Joining of Silver Nanoparticles: Computer Simulations and Experimental Observations

by

Ehsan Marzbanrad

A thesis
presented to the University of Waterloo
in fulfillment of the
thesis requirement for the degree of
Doctor of philosophy
in
Mechanical Engineering - Nanotechnology

Waterloo, Ontario, Canada, 2016

AUTHOR'S DECLARATION

I hereby declare that I am the sole author of this thesis. This is a true copy of the thesis, including any required final revisions, as accepted by my examiners.

I understand that my thesis may be made electronically available to the public.

Ehsan Marzbanrad

Abstract

This dissertation introduced a new type of high aspect ratio silver nanoparticle, synthesized by assembly and joining of hexagonal and triangular nanoplates. The synthesis procedure is a simple mixing at room temperature of silver nitrate solution with ascorbic acid and PMAA solution. After mixing, the synthesis starts from reduction of silver ions, leading to nucleation of silver crystals. Growth of the nucleated crystals in presence of capping agent produces thin hexagonal and triangular nanoplates. These nanoplates assemble and join to make one-dimensional segments. This process continue through assembly of the segments to form one- or two-dimensional supercrystals, the configuration of which is controlled by experimental condition such as silver content of the reactor, nitrate ion content, and pH. The introduced synthesis method answers one of the major questions that motivated this research: Finding a simple, feasible, high-yield, low-cost, and mass producible high aspect ratio silver nanoparticles for using as nanofiller in hybrid electrical conductive adhesives and for various other industrial applications.

SEM observation reveals that final thickness of the synthesized nanoparticles are around 25 nm, while the other sides are bigger, even up to 100 μm length nanobelts. TEM and XRD demonstrate that the synthesized nanostructures exhibit a (111) crystal texture on their broad surface, inherited from their nanoplatelet structural blocks. One- and two-dimensional silver nanoparticles with (111) surface plane on this scale is a unique material that has not reported before this research.

Molecular dynamics simulation reveals that the nanoplates join together to produce a perfect crystal at the formed joint. The simulation results are confirmed by high-resolution TEM observation. This is another important feature of the synthesized nanocrystals that provide unique properties such as good electrical conductivity. Another important property of the synthesized material is high thermal stability, which originates from the (111) crystal texture surfaces being composed of low-energy and high-stability atoms, compared to the surfaces of other silver nanoparticles. This stability is confirmed by molecular dynamics simulation and experimentation, with comparison to pentagonal silver nanowires with (100) surface crystals. This high thermodynamic stability of the synthesized silver nanoparticles raises the working temperature limit of silver nanoparticles by several hundred degrees over that of the competing nanoparticles.

In addition to application of the synthesized 1-D high aspect ratio silver nano particles as nanofiller for enhancing electrical properties and reducing the cost of the hybrid electrical conductive adhesive, the synthesized 2-D silver nanosheets were employed as the primary functional material to fabricate an

airflow sensor. The fabricated sensor was examined for detecting low airflows (below 5 ml/min). The sensor shows a linear and repeatable response to airflow in the range of experiment. Simple sensor fabrication method, high electrical stability and excellent atmospheric corrosion resistance of silver nanosheets at working temperature of the sensor (120˚C) are other outstanding features of the synthesized silver nanostructures that make them good candidate for future research.

Looking at the thermal behaviour of silver nanoparticles a traditional question is raised about the hypothesized existence of a liquid layer on the surface of silver nanoparticles, called "surface premelting" in the literatures. Molecular dynamic simulation was employed to investigate the phenomenon. This thermodynamic investigation uncovered that by increasing temperature, thermal phonons become potent enough to overcome the cohesive energy of the surface atoms, throwing atoms from their lattice positions to create stable surface defects. Accumulation of defects, which is temperature dependent, is able to create a solid disordered-phase layer covering the nanoparticle surface. Existence of this disordered layer was confirmed in the literature, although it is interpreted as liquid layer in some reports. Investigation into the physical state of this disordered surface layer uncovered that it exists as an amorphous solid, which remains solid until melting temperature, and that the melting of the nanoparticle happens at a constant temperature: a usual melting based on classical thermodynamics. This finding contradicts the predicted behavior of the literature's "surface pre-melting" phenomena, providing an alternative answer to a traditional question that has been asked in this field of science since the 1940s.

Acknowledgements

I would like to express my sincere gratitude to my supervisor, Professor Norman Y Zhou and my co-supervisor, Professor Boxin Zhao, for their valuable supports and guidance.

I owe my deepest gratitude to my wife Bahareh and my daughter Vania for their unconditional love, trust, understanding, encouragement, and patience, which made this research possible. Also, I would like to extend my appreciation to my mother and my parents-in-law and my brother-in-law, Mohammad Marzbanrad, for their sincere love and continuous supports.

I am thankful to Mark Griffett, Neil Griffett, Andy Barber, and Martha Morales for their technical supports. I greatly appreciate my colleagues, Professor Anming Hu, Mr. Geoffrey Rivers, Professor Peng Peng, Dr. Melisa Hattat, Dr. Ali Nasiri, Dr. Allan Rogalsky for their precious thoughts and discussions.

To my wife Bahareh and my Lovely daughter

Vania

Table of Contents

List of Figures

List of Tables

Chapter 1
Introduction

In 1959, Richard Feynman introduced a new concept of *small systems* in his presentation entitled "There's Plenty of Room at the Bottom"[1]. However, research into nanoscience and nanotechnology has only started two decades after Feynman, in the early 1980s considering developments in analysis and microscopy techniques [2]. During the last three decades, research outcomes have developed our understanding of small systems and led to new materials, apparatus and many potential applications. As part of this advancement, nanoparticles with different sizes, shapes and morphologies have been synthesized.

Today, individual nanoparticles can be used for various applications such as nanosensors and nanotransistors. In addition, nanoparticles have been employed by other routes such as membrane, thin and thick film, pellets and filler materials for making composites, and research continues in these fields. Another potential application of nanoparticles is fabrication of structures, devices or machines from nano scale building blocks. For this purpose, nanoparticles should assemble and join as two important steps in the fabrication process. The assembly of nanoparticles is a hot research topic and scientists have put many efforts into this subject [3-7]. Nowadays, it is possible to control nanoparticles and push them to the desired positions by different methods such as self-assembly and electric field assisted assembly [8, 9]. However, current knowledge about joining of nanoparticles, which can be named nanojoining, is in a preliminary stage. Expanding the knowledge in the field of nanojoining along with the progress in self-assembly of nanoparticles will provide the capability to design and produce new nanomaterials, nanodevices and nanomachines. Therefore, research for understanding joining methods for nanomaterials and finding controllable joining methods seems to be a very important topic.

1.1 Motivation

Among all elements, silver is one of the most interesting materials for nanotechnology because of its remarkable properties. In recent years, silver nanoparticles with different shapes and sizes have been synthesized and proposed for various applications such as optoelectronic sensors and devices, biological sensors, nanocomposites and catalysts, and these researches are ongoing [10-14]. Along with this progress, difficulties arise, however, when researches attempt to go further from prototype to market. A feasible, high yield, repeatable, and environmentally friendly, method of synthesis is a real demand for industrial applications. On the other hand, stability is another major weakness of silver nanoparticles. It is well known that silver is inherently susceptible to electromigration. This issue becomes more serious in nanoparticles because of higher energy level of the silver atoms in nano-scale than bulk [15-17]. Thermal stability of

silver nanoparticles, especially silver nanowires, is another important obstacle in front of application of silver nanoparticles, which limits working temperature of these nanoparticles [18]. Regarding those fascinating proposed applications for silver nanoparticles, and above-mentioned issues, synthesis of a fast, high yield, high stability zero-, one-, and two-dimensional silver nanoparticle seems to be very critical research topic.

Stability of a material strongly relates to its atomic arrangement. It is well known that non-crystalline solids have higher energy and less stability than crystalline structures; and, among different crystallographic planes, higher packing factor provides lower energy and higher stability for that crystal plane. Silver has face centered cubic crystal structure in which the (111) planes have the densest packing. Among all different silver nanoparticles, the hexagonal and triangular nanoplates have maximum (111) surface texture [19-21]. Therefore, silver nanoplates seem ideal structural blocks for fabricating high stability one-, two-, or three-dimensional superstructures.

Assembly of the structural blocks can be done by different methods, however, joining of the assembled blocks is a challenging task. To understand the difficulties of nanojoining from a material point of view, it is worthwhile to pay attention to the thermodynamic behaviour of nanoparticles. Total energy of a system can be divided into potential and kinetic energy. Origin of the potential energy of the system is attraction and repulsion forces between the atoms. The kinetic energy presents movement and vibration of the atoms. In large scale, the total energy of the internal atoms of a system is very much larger than the sum of the energy of atoms at surfaces and around structural defects. Hence, the effect of surfaces, interfaces and defects on the total energy of the system can be ignored. However, when the particle size decreases the ratio of surface energy to bulk energy of the particle will increase. Therefore, when the particle is very small, the surface energy must be taken into account for any calculation. The surface atoms can change stability of the nanoparticles because of their high energy level [22-25]. The tendency of these excited atoms to decrease their excess energy is the origin of much special and unusual behaviour of small systems. This phenomenon can influence nanojoining processes, and it can also introduce new joining methods for small systems. On the other hand, high-energy surface atoms of nanoparticles can cause problems for implementing traditional joining process in nano scale.

Stability of nanoparticles, their special properties such as unusual melting properties and absorbed species on the surface of nanoparticles are the most important barriers in front of traditional joining methods at nano-scale [26-28]. The melting point of nanoparticles is a function of their size and is usually lower than the melting point of bulk material. In addition, high mobility atoms on the surface of the particles and surface disordering can be observed in nanoparticles before melting. Therefore, control of thermally activated joining process such as sintering and welding will be very difficult and complex. In addition to the aforementioned issues, existence of high energy atoms at the surface of nanoparticles leads to absorption

of ions and molecules from surroundings or agglomeration of nanoparticles which can be a barrier in front of nanojoining by eliminating direct and simple contact of the structural blocks.

To overcome these complicated problems facing nanojoining, more research in this field is necessary. To solve these problems, two different approaches can be considered. First, one may attempt to achieve enough knowledge from behaviour of nanomaterials to control traditional joining process for nanojoining applications. The second approach is to invent new methods for joining of nanomaterials. The focus of this research is the investigation of novel methods for joining of nanomaterials. In this regard, both theoretical study and experimental observation are considered. Theoretical studies have been conducted by molecular dynamics simulation; and, experiments have been employed to examine the simulation predictions.

1.2 Research objectives

Synthesis of high stability one- and two-dimensional silver nanoparticles with a high yield, using a feasible and repeatable method is a main goal of this project. For this purpose, hexagonal and triangular silver nanoplates were selected as structural blocks for fabricating one- or two dimensional structures. These nanoplates have been selected because of their special surface texture, which consist of two large (111) flat surfaces. This unique surface texture could provide special properties such as high stability for the nanoplates. The first part of this research is an attempt to systematically investigate nanojoining of the hexagonal and triangular nanoplates. For this purpose, the molecular dynamics simulation method was selected to uncover the joining mechanisms, features and limitations. Molecular dynamics is a powerful simulation technique, which can be employed to investigate nanoparticle behaviour; but simulation by itself is not sufficient and experimental observation should also be done to confirm that simulation results are reliable and applicable in the real world. Therefore, experimental observations are also considered in this research.

The tendency of the nanoparticles' surface atoms for decreasing their excess surface energy by absorbing other molecules or ions can be a new window to nanojoining. If the surfaces of two nanoparticles are placed in contact properly, they will join to decrease their surface energy. This type of joining is experimentally observed at large scale through joining of silicon wafers in a well-controlled condition [29]. To carry out joining through this method, very special conditions such as extremely clean and flat surfaces are required to get good joints. Meanwhile, different issues such as surface roughness, oxidation and contamination of the surfaces with some molecules such as oil and grease are big barriers in front of this joining process. Therefore, direct contact joining does not seem feasible as a joining method at large scale. However, the story can be different at nanoscale. Surface atoms of nanoparticles not only have higher energy than large-scale particles but also the larger ratio of the surface energy to total energy of the particle than those of large scale materials, and in consequence, nanoparticles have higher tendency to decrease their surface energy. This is a new concept and it has not been systematically studied to be employed in joining of nanomaterials

yet. This self-joining will be tested in the first part of this research to see if it can be considered as a joining method for small systems. If yes, the mechanism of joining, the particle size range that this mechanism can be employed for joining and affecting parameters will be investigated.

In addition to theoretical study, nanojoining mechanisms are verified by experimental observation. For this purpose, the silver hexagonal and triangular nanoplates self-joining was the subject of study. Importance of these tiny silver nanoplates relates to the existence of (111) crystal planes on their surfaces. If these nanoplates can be assembled and joined to each other and built into one or two dimensional structures, the resultant fabricated structure will be a unique material with special crystal structure, while all other one one-dimensional silver nanoparticles have mostly (100) planes on their surface. Therefore, the experimental part of this project is designed not only to compare experimental results with the simulations but also introduces self-joining as a method for fabrication of silver structures with special properties.

1.3 Justifications

Synthesis of high stability silver nanoparticles with a feasible, repeatable and high-yield method is a critical step in development of nanotechnology from laboratory to industrial scale production. In this research a new approach to the synthesis of silver nanoparticles is proposed. This method is fabrication of silver nanoparticles by self-assembly and nanojoining of the hexagonal and triangular silver nanoplates.

Nanojoining is essential for nanofabrication. However, a systematic theoretical study and experimental observation in this area of nanoscience have not been conducted yet. The importance of research into nanojoining can be emphasized by considering the potential applications for nanostructures, nanomachines and nanodevices. In addition, complicated behaviour of nanomaterials, which are size and morphology dependent, should be well established to have successful nanojoining. This research will introduce a novel nanojoining method which is oriented attachment or self-joining of nanoparticles. This method of nanojoining can be used for many applications such as temperature sensitive systems and flexible electronic circuits.

On the other hand, using silver nanoplates as structural blocks will provide unique properties for silver nanostructures. By a successful fabrication, surface texture of the product should be same as the structural blocks. The hexagonal and triangular silver nanoplates are the only silver nanoparticles that have maximum high close packed (111) planes on the surface. This texture must provide very unique properties for the fabricated structures such as high stability, which will be investigated in this research.

1.4 Criteria and constraints

This research will be done on silver nanoparticles for both simulation and experimental parts. This system is selected based on the importance of silver in nanotechnology and biotechnology. All simulation will be based on classical molecular dynamics simulation.

Experimental observations of self-joining will be restricted to joining of triangular and hexagonal silver nanoparticles, although the modeling side will not be restricted to these nanoplates, and other structures can be considered for simulation. All restrictions of a molecular dynamics simulation such as total simulation times, sizes of the particles, will be limitations of the simulation part of the project.

1.5 Thesis Layout

This thesis consists of eight chapters as follows:

The current chapter (Chapter 1) outlines the motivation of this research and declares the thesis objectives. The Chapter 2 presents the background information about different synthesized silver nanoparticles. Following this chapter, nanojoining methods and self-assembly of the nanoparticles is introduced as background for this research. The molecular dynamics simulation is briefly described in chapter 3. The chapter 4 focuses on the nanojoining of hexagonal and triangular silver nanoparticles. Experimental results on the synthesis of one- and two dimensional silver nanoparticles by self-assembly and nanojoining of hexagonal and triangular nanoplates are depicted and discussed in chapter 5. Then thermal stability of the synthesized nanoparticles is revealed in chapter 6. Moreover in this chapter, surface disordering and melting of silver nanoparticles are discussed. Chapter 7 depicts some applications of the synthesized silver nanoparticles. Finally, conclusions and recommendation for future work are summarized in chapter 8.

Chapter 2
Literature review

2.1 Silver

Silver is a metal with a very long history. This metal has excellent electrical and thermal conductivity with good mechanical properties and chemical stability. Meanwhile, special properties of nano-size particles and thin films of silver such as antibacterial, catalytic and optical properties change this old metal into a strategic material for the modern world. These outstanding properties of silver, which is also associated with reasonable price in comparison to its competitors such as gold and platinum encourage scientists to conduct many researches to develop the synthesis methods, investigate properties in different conditions, and find new applications, and studies into these topics are ongoing [30-36]. Among them, one of the most important and basic topics is synthesis of nanoparticles with different morphologies. Since the material properties of nanoparticles is dependent on their shape and morphology, synthesis of silver nanoparticles with different morphologies has been a hot research topic in recent years.

Various methods have been developed for synthesis of silver nanostructures, including chemical reduction, chemical vapor deposition (CVD) and physical vapor deposition (PVD) [19, 37-41]. Among them, the solution-based chemical reduction is a simple, low-cost and flexible method. In this method of synthesis, it is possible to adjust solution conditions and chemical agents of the reaction to produce different types of nanoparticles, nanowires and nanoplates (Figure 2-1). The general strategy for controlling morphologies of the synthesized nanoparticles is to coat a certain crystallographic plane with a capping agent to change the growth rate in different crystallographic directions [7, 38, 42-44]. Thus far, the surface planes of synthesized silver nanomaterials through solution-based chemical reduction route are mostly (100) planes although the (100) plane is not the most stable or low energy plane in the fcc crystal structure[45, 46]. It is well known that the most stable crystallographic planes with the lowest energy in a fcc crystal structure are highly packed (111) planes that usually form the surface of stable crystals of fcc structures[41]. In addition, it has been shown that (111) planes have better performance in comparison to other crystallographic planes in some applications such as catalytic reactions [41]. In this regard, the synthesis of new grades of silver nanoparticles with preferred (111) surface planes will be highly beneficial for different applications.

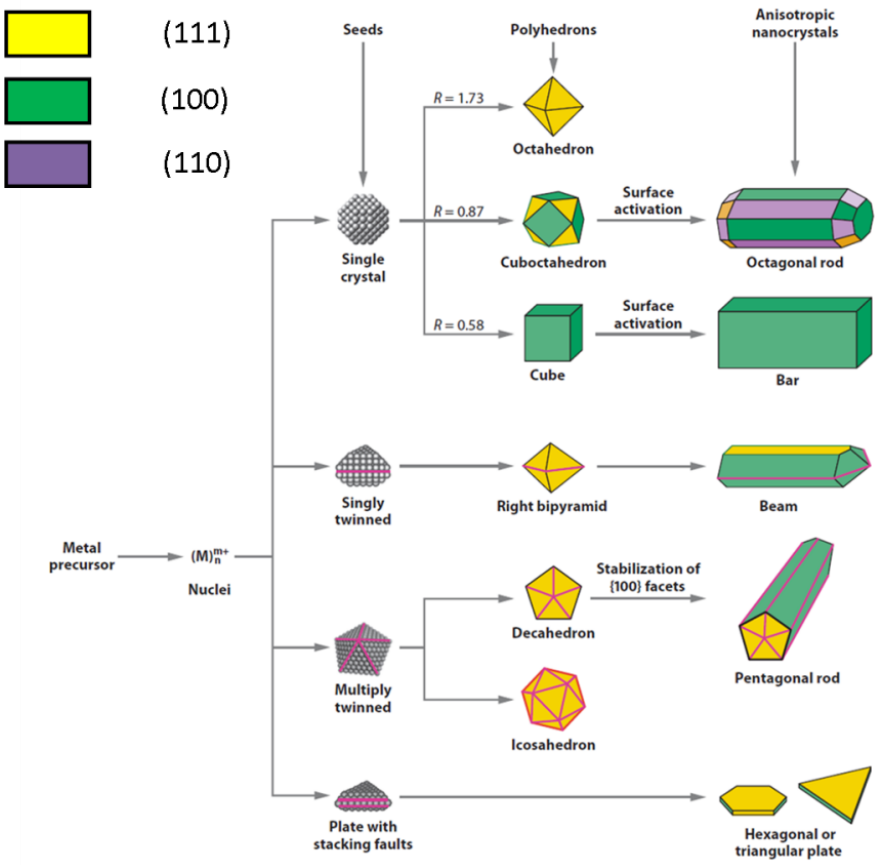

Figure 2-1: Synthesized silver nanoparticles through chemical reduction method [37]

Among different morphologies of silver nanoparticles, hexagonal and triangular silver nanoplates are two morphologies of silver with maximum (111) planes on their surface. The crystal structure of these nanoplates was revealed to have a twin plane in the center and two (111) planes at the top and bottom surfaces parallel to the twin plane [19-21]. These nanoplates are synthesized by capping the top and bottom (111) planes with special molecules or ions to reduce the growth rate of the crystal in this direction. Hence, the nanoplates can grow mostly from the edges. The edges of very thin nanoplates are a combination of (100) and (111) planes. A flat hcp layer is formed at the edge between the (111) and (100) planes when nanoplates become thicker[21]. Different growth rate of silver crystal in directions leads to change initial hexagonal particles to triangular form.

In this research, silver has been selected for all experiments and simulation works. It is well known that response of all nanoparticles to environmental stimuli is size dependent. Based on the traditional joining strategies, two nanoparticles have to be placed in contact or have a special material between them and then one must give energy to the system to make a strong bond between the particles. The existence of another particle or material close to a nanoparticle and any kind of energy that transfers to it are powerful stimuli

and could lead to change in the shape, morphology and structure of that nanoparticle. The sensitivity of nanomaterials to environmental stimulus is not only size dependent but also material dependent, since it is related to the interaction between the atoms. Hence, for consistency of the results, it will be beneficial if all simulations and experiments are done on same material. In addition, it seems more realistic if a pure system is selected for simulations and experiments because of the complicated mathematical calculations, simplifying assumptions and restriction of computing capability of available computers.

2.2 Self-assembly

Experimental observation of self-joining of silver nanoparticles shows first self-assembly of the particles during synthesis, which is followed by self-joining (nanojoining) of the particles. In this section, self – assembly of nanoparticles will be reviewed as a background for experiments. Nanoparticle self-assembly and joining has been reported in the literature [3, 7, 47, 48]. Sun et al reported that it is possible to transform silver nanospheres to nanobelts through self-assembly of the nanoparticles and subsequent thermal treatment to remove adsorbed surface molecules and sinter the particles[39]. In another research, Tang et al reported organization of CdTe nanoparticles into nanobelts, in which after partial removal of thioglycolic acid stabilizer layer of the colloidal CdTe nanoparticles by methanol, the CdTe nanoparticles attached to each other and made crystalline CdTe nanobelts [49]. It is interesting that individual CdTe nanoparticles coalesced to become a single crystal. The authors suggested two different mechanisms: one is Oswald ripening and the other is the direct fusion of the particles for single crystal formation [39, 50, 51]. However, the mechanism of orientation was not discussed and a dynamic procedure transferring fused nanoparticles into single crystals was not clarified. Kalsin et al reported that silver and gold colloidal nanoparticles could join to each other to form a diamond-like lattice structure [52]. They showed that these nanoparticles created unusual binary crystals through electrostatic self-assembly and could join to each other at room temperature to make crystalline particles. Recently, Zhang et al reported self-assembly of silver nanoparticles at room temperature which led to a 2D array ultrathin film of silver nanoprisms on the glass substrate, providing a tunable Plasmon response property [53]. These experimental researches show the importance of nanoparticle joining especially at low temperature.

2.3 Nanojoining

Nanojoining can be defined as joining of two nanoparticles in such a way that they keep their original shape, morphology, size and make a proper bond that can withstand applied forces in an acceptable range. It is well known that the morphology, shape and size of nanoparticles play important role in outstanding

properties of nano-size materials. Therefore, for having the benefit of the distinguishing features of nano-size particles in the manufactured devices or structures, their original shape, morphology and size should remain intact during fabrication. On the other hand, the strength of a structure is a function of mechanical properties of its building blocks and their joining strength. Hence, the joints between nanoparticles must have proper strength. Common methods of joining at large scale are welding, sintering, soldering, brazing and adhesive bonding. Each of these methods employs special materials, techniques and apparatus to join different parts and has its properties and applications. General trend in the field of nanojoining is using same methodology and scientists try to customize these techniques for nano scale applications. Based on the literature, current nanojoining methods can be summarized into four different groups as listed in Table 2-1. To implement these joining techniques at nano scale, precisely controlled machines and devices are required. In addition, properties of nanoparticles should be known to adjust the process. Although these successful nanojoining examples are very good news for joining of nanomaterials, many questions have not been answered yet. For example, it should be determined if these joining methods can be applied for different size nanoparticles, especially very small ones, and different morphologies. In addition, some new devices such as flexible electronics cannot withstand high temperature treatments. Therefore, some restrictions in using high power energy sources arise in these applications.

Table 2-1: Nanojoining methods [54-56]

Solid state bonding	Electron beam welding, Diffusion welding, Ultrasonic welding, cold welding,
Soldering/Brazing	Liquid-phase reflow soldering, Resistance soldering, Active brazing, Laser brazing
Fusion welding	Laser beam welding, Resistance welding
Adhesive bonding	Adhesive bonding

There are several theoretical studies on the joining of nanoparticles. However, their focus has almost always been investigation of some unusual behaviour of the material at the nano-scale such as lower melting point of nano materials or surface premelting that is used to explain nanoparticle sintering [57-61]. Surface premelting and size dependent melting behaviour in nano scale were usually employed to explain nanoparticle joining. A good example of these theoretical studies is one by Hu *et al* concerning low temperature sintering of silver nano particles for flexible electronic packaging [62]. They employed a Monte Carlo simulation to support their experimental results. Size dependent behaviour of the silver nano particles was the goal of their model, which was employed to explain low temperature joining and high temperature application of the silver nano particles as electronic packaging. Detailed results of Monte Carlo simulation

of sintering of silver nano particles were published by Guo et al [63]. They showed that small silver clusters could join to each other even at 0.01K. At a higher temperature, attachment and initial joining were followed by sintering of the particles because of the diffusion of atoms. Although Monte Carlo is a simple and powerful method for prediction of the most probable state of a system regarding minimization of the energy of the system, it is not suitable for explanation of the dynamic sintering process. Because, in this method of simulation, the most stable configuration for atoms of the system is found based on a random change in atomic positions and comparing the energy change of the two configurations [64]. On the other hand, the size of the biggest particle in their research was less than 1 nm. Qi *et al* shows that the cohesive energy of the particles is size dependent [24]. They developed a model to explain cohesive energy of particles as a function of the particle size. Based on their model, cohesive energy of a spherical particle can be calculated using the following equation:

$$E_p = E_b\left(1 - \frac{d}{D}\right) \qquad (1)$$

In this equation, E_p is cohesive energy of the spherical particle, E_b is cohesive energy of bulk material, which is equal to 284 KJ/mol for silver [24], d is equal to atomic diameter, which is equal to 0.288 nm for silver and D is the diameter of the nanoparticle. Equation (1) shows when the particle diameter becomes around 1nm or less, the effect of size on cohesive energy of the particle becomes very important. It means, changes in the total energy of a particle are not linear and extrapolation of the modeling results for subnanometer particles to bigger ones is not accurate. Therefore, another simulation method providing the detailed explanation should be employed to clarify mechanisms of nanoparticles joining.

Different joining methods have been employed to join nanoparticles. Some of these methods have been listed in table 1-1 and, as mentioned in introduction many researches should be done to find a well-established method for joining of nanoparticles. In this chapter, a short review on the mechanism of sintering is provided here to make a background for future discussions about similarities and differences between sintering and self-joining or oriented attachments of nanoparticles. After that, oriented attachment is introduced as an alternative method of joining method, which is starting point for current research.

2.3.1 Sintering

Sintering is one of the oldest human technologies, coming from the time when people made their goods from clay and fired them to make them stronger. Sintering is a thermally activated process in which, particles make a bond through mass transfer process [65]. From thermodynamic point of view, driving force for sintering is minimizing surface energy of the particles [65-69]. Sintering starts from neck formation between two adjacent particles and follows by pore shrinkage. The mass transfer can be done in solid state sintering through bulk diffusion of atoms, grain-boundary diffusion, surface diffusion, viscous or plastic flow that is caused by surface tension or internal stresses of the particles and evaporation/condensation of

atoms on surfaces[70]. Based on the thermodynamic models, the behaviour of an array of same size spherical particles can be explained[67]. Sintering process starts from necking. This preliminary neck grows as shown in Figure 2-2.

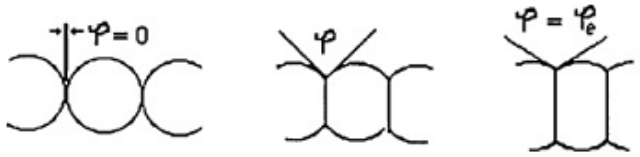

Figure 2-2: Schematic presentation of sintering of an array of spherical particles [67]

During neck growth, the contact angle between the particles increases as shown in Figure 2-2. This angle has an equilibrium value, which can be calculated from the balance between the surface and grain boundary energy through the Yang relation as presented in equation 8 [67].

$$\frac{\gamma_{gb}}{\gamma_s} = 2cos(\varphi_e) \quad (8)$$

Where, γ_{gb} is the grain boundary energy, $\gamma_s$is the surface energy and φ is the contact angle between the particles. This process makes a bond between the particles, meanwhile shape of the particles changes as shown in Figure 2-2, schematically.

The sintering process is a dynamic process and simultaneously other phenomena such as grain growth and coalescence may occur; because, the mechanisms of these phenomena are the same as sintering. As mentioned, neck growth causes the shape of the particles to change during sintering. This process is more dramatic when size of the particles is not equal. Figure 2-3 shows schematic of sintering progress of two particles with different size followed by grain growth. The process starts by necking initiation that is followed by neck growth. This process continues until the contact angle reaches an equilibrium value. From this stage, the grain boundary moves and grain growth occurs. After grain growth the barrier that stop the sintering process, equilibrium between grain boundary and surface energy, does not exist and the particle shape can change to find a more stable condition. This shape change can be done by diffusion.

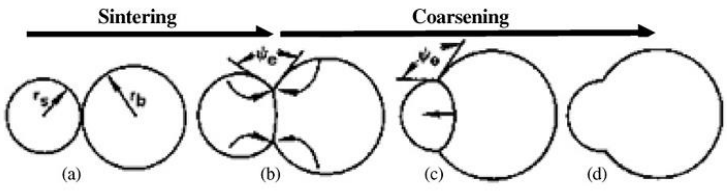

Figure 2-3: Sequential mass transport between two touching particles; steps: a to b, sintering; b to c, coarsening; c to d, grain boundary motion [67].

Figure 2-4 shows another schematic sintering process that shows sintering of three particles. Same as the previous case, sintering starts from neck initiation and follows by neck growth to reach equilibrium. After this stage, grain growth can happen and after that another sintering can be done to reach a new equilibrium. It is worthwhile to mention that these schematic explanations were supported by experiments [66-68].

The aforementioned explanation of the sintering process shows that it is a thermally activated process. Therefore, all other phenomena such as grain growth and coalescence that work with the same mechanisms can arise during sintering. For nanoparticles sintering, enough thermal energy should be provided to activate the sintering mechanisms. On the other hand, during sintering and other phenomena, which happen at the same time, shape and size of the particles can change to reach the most thermodynamically stable condition. This shape change is a big issue in front of using sintering as a candidate for nanojoining.

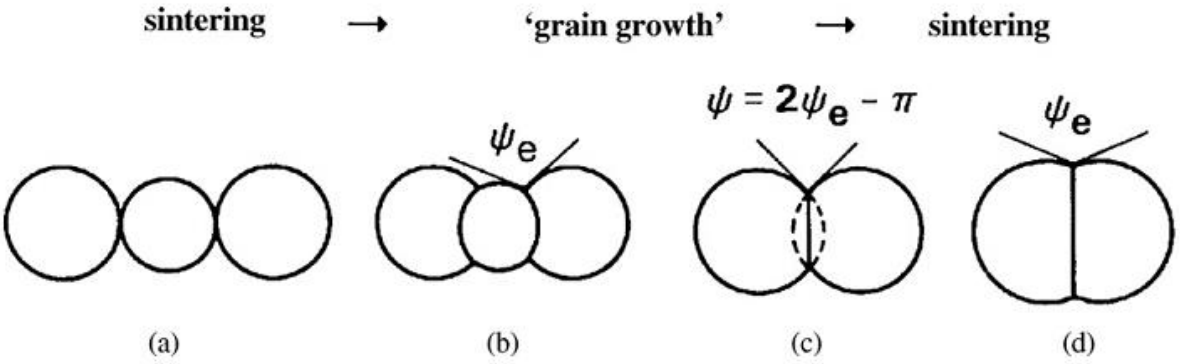

Figure 2-4: Sequential mass transport for two larger particles sandwiching smaller particle; steps: a to b, sintering; b to c, coarsening; c to d, sintering between larger touching particles [67].

Sintering of nanoparticles has been employed in many applications such as conductive adhesive, metal-metal bonding and flexible electronics [71-74]. Sintering or coalescence of very small nanoparticles such as silver nanoparticles will happen at a temperature lower than bulk material. Importance and potential applications of low temperature sintering of nanoparticles lead to many studies into this unusual phenomenon. Based on the published research articles, researchers believe that existence of liquid layer on the surface of nanoparticles and higher energy of small nanoparticles in comparison to bulk material are two major origins of these phenomena [27, 28, 58, 75].

Research into coalescence of nanoparticles have revealed the structural changes during coalescence. An example of these experimental observations is presented in Figure 2-5, which shows coalescence of two Au nanoparticles with different crystal structure [76]. As clearly seen, the coalescence started from a necking while the particles were aligned completely, Figure 2-5-a and b. The coalescence process had continued by neck widening which led to more alignment of the particle. This crystal alignment had induced stress in the crystal, which led to some crystal defects, Figure 2-5-e. These defects then moved out from the crystal and

final structure after coalescence was a perfect crystal, Figure 2-5-f. This complicated process was observed by TEM microscope and the particles were heated by electron beam. Therefore, this coalescence process occurred at high temperature.

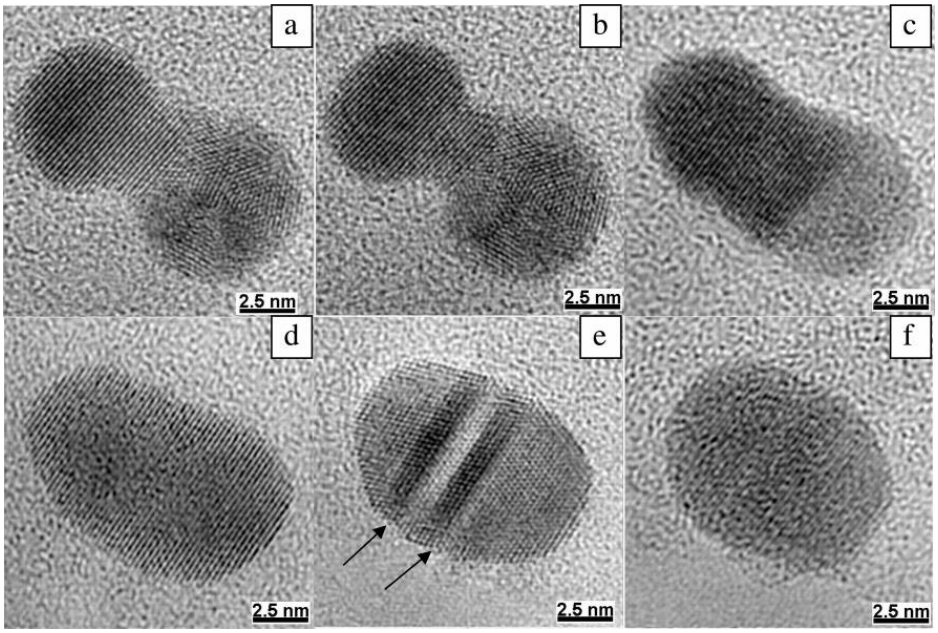

Figure 2-5: Coalescence between Au nanoparticles of different crystal structures; (a,b) Neck formation at the contacting surfaces; (c) The planes align between the two nanoparticles, and the neck widens; (d) Planes are completely aligned, and the voids formed by the previously existing neck fade away, tending to a rounder shape; (e) Plane defects begin to appear as a result of the stress in the new structure; stacking faults are clearly observed as marked by the arrows; (f) The newly formed structure is now relaxed, and structural defects are no longer noticeable [76].

Moreover, several theoretical studies were conducted to explain nanosintering and coalescence [27, 28, 59, 61]. These observations show that nanoparticles can be joined to each other in different configurations, situations and temperatures. Generally, these theoretical studies have followed experimental observations for sake of comparison. In addition, limitations of simulation methods restricted the cases theoretically studied. Figure 2-6 is an example of these simulations that shows coalescence of two iron nanoparticles at different temperatures [59]. The presented results reveal that at 400K the particles have only joined to each other and kept their initial shapes intact. However, at higher temperature, some atoms have diffused to adjacent particles while shape of the particles started to change.

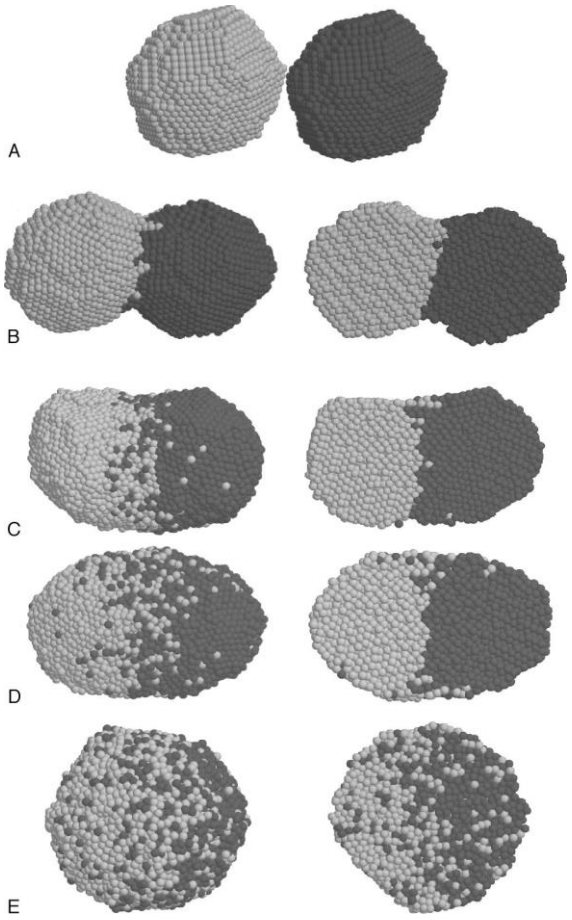

Figure 2-6: Snapshots at different temperatures during $Fe_{5000}+Fe_{5000}\rightarrow Fe_{10000}$ coalescence and melting; a) initial structure at 400 K; b) 800 K; c) 1200 K; d) 1400 K; e) 1460 K. The left pictures in B–E are of the entire cluster and show the surface atoms, whereas the pictures on the right-hand side are cross sections through the clusters [59].

2.3.2 Orientad attachment

When two piece of a solid material that have clean and flat surface reach to each other, they will join and make a unique crystal. One example of this type of joining was reported by Gosele *et. al.* in 1995 [29]. They washed two piece of silicon wafer with diluted HF acid then put in an ultrahigh vacuum chamber, heated to 600˚C-800˚C to degas the surface and then push the wafers together at room temperature. The clean flat silicon wafers welded and make a single piece. Nanoscale particles seem to be able to join to each other directly when they get in contact, particularly because of high energy surface atoms of nanoparticles [25]. Therefore, this phenomenon can be used as a method of joining for constricting nano-scale structures or synthesis supercrystals. This type of nanostructures are classified under non-classical crystallization and

this type of joining calls oriented attachment [77]. Classical crystallization starts from nucleation of a crystalline phase in a matrix and continues via atom-by-atom attachment process. In contrast, non-classical nucleation happens through assembly and oriented attachment of structural blocks. Different examples of this type of crystallization was reported in the literature, most of the restricted to experimental characterization of this type of structures [78]. Based on these research, this method of nano-fabrication or synthesis can be employed for many applications, while current researches in this field are mostly restricted to fundamental observations.

Oriented attachment or self-joining of nanoparticles has some distinguishing features. It is a room temperature, and fast joining and result of joining is a perfect crystal boundary when the joined particles are small [79]. Interestingly, the joining happen very fast and finish. However in case of sintering, if thermal energy is provided, sintering will continue and two initial structural blocks completely dissolve in each other and make a single particle. Therefore, understanding mechanism of oriented attachment or self-joining and using it for constructing nanostructures could be very important progress in nanotechnology.

Chapter 3
Simulation methods

3.1 Classical molecular dynamic simulation

Classical molecular dynamics (MD) is an atomic scale method of simulation, in which a system is defined by atoms and evolution of the system during simulation time explored by calculating movement of atoms. To build a MD model, initial positions, initial velocities and masses of the atoms are set as initial conditions. The interaction of the atoms is defined as another input for the model. To do a simulation, total simulation time is divided into equal time steps. In each time step, the applied force on each atom by other atoms is calculated and new positions and velocities of the atoms are calculated by using classical mechanic equations of motion. The material properties can be calculated from the positions, velocities and applied forces on each atom. In this research, classical MD simulation will be employed, which means quantum effects are not considered in this simulation. In other word, electrons are not present explicitly in this MD simulation. They are introduced through the potential energy, which is a function of atomic positions only (Born-Oppenheimer approximation).

There are three major limitations for classical MD simulation. One of them is the limitation that comes from replacing Schrödinger equation for nuclei with classical Newton equations. One indicator of the validity of the replacement is the de Broglie wavelength Λ. Quantum effects are expected to become significant when λ is much larger than inter particle distance. For thermal motion we can use the thermal de Broglie wavelength:

$$\lambda_{th} = \frac{h}{\sqrt{2\pi m k_B T}} \qquad (1)$$

In which, h is plank constant, *m* is mass of the atom, k_B is Boltzmann constant and *T* is temperature. Typical interatomic spacing in solid-state materials is d ~ 1-3 Å. Therefore, All atoms, except for the lightest ones such as H, He, Ne, can be considered as "point" particles at sufficiently high temperature (d >> λ) and classical mechanics can be used to describe their motion. Second limitation of MD is limitations on the size of the MD computational cell (number of atoms). The size of the computational cell is limited by the number of atoms, which can be included in the simulation, typically 10^3 – 10^7. This corresponds to the size of the computational cell on the order of tens of nm. Any structural features of interest and spatial correlation lengths in the simulation should be smaller than the size of the computational cell. The last important limitation of MD is time scale of the simulation. The maximum time step of integration in MD simulation is defined by the fastest motion in the system. Vibrational frequencies in a molecular system are up to 3000 cm^{-1} which corresponds to a period of ~10 fs. Optical phonon frequencies are ~10 THz - period of ~100 fs. Therefore, a typical time step in MD simulation is on the order of a femtosecond. Using modern computers

it is possible to calculate $10^6 - 10^8$ time steps. Therefore simulation time can be only in the range of 1 ns to 100 ns. This is a serious limitation for many problems which involve thermally-activated diffusional processes.

As mentioned, in order to use MD simulation interatomic potential should be defined for the atoms in the system. The potential function $U(r_1, r_2, \ldots, r_N)$ describes how the potential energy of a system depends on the coordinates of the atoms ($r_1, r_2, \ldots, r_N$). The forces in MD simulation are defined by the potential:

$$\vec{F}_i = -\vec{\nabla}_{r_i} U(\vec{r}_1, \vec{r}_2, \ldots, \vec{r}_N) \qquad (2)$$

$\vec{\nabla}_{r_i}$ operates on the position r_i of atom i. Any change in the total potential energy that results from a displacement of atom *i* contributes to the force acting on atom *i*. Position of atoms are calculated by using the calculated force through the second Newton's equation of motions. The total potential energy of the system is a sum over all pairs and the total force acting on each atom is found by summing over all pairwise interactions.

In this research, MD simulation method is employed to study nanojoining of silver nanoparticles. One of the best interatomic potentials which can be used for MD simulation of metals is embedded atom method (EAM) which is developed by Daw and Baskes[80, 81]. In EAM, the total energy is taken by the following equation:

$$E_{total} = \sum_i F(\rho_i) + \frac{1}{2}\sum_{i,j,i\neq j} \emptyset_{i,j}(r_{ij}) \qquad (3)$$

Where $\emptyset_{ij}$ is the two body potential between two atoms i and j with distance r_{ij} , $F(\rho_i)$ is required energy to embed atom i into the electronic gas due to all neighbor atoms which can be calculated by following equation:

$$\rho_i = \sum_{i\neq j} f(r_{ij}) \qquad (4)$$

EMA interatomic potential parameter for silver and some other fcc metals were calculated by Foiles *et al* [82]. MD simulation is done in a C++ program that developed and visualizations are done through VMD and Atomeye, which are open source software [83]. The MD simulations were carried out in the canonical (NVT) ensemble. Temperature was kept constant during simulation according to the Nose-Hoover thermostat [84]. The equations of motion were solved numerically using the Verlet algorithm [85]. Each time step of calculation was one femto second $(1\times10^{-15}\text{fs})$. Cut off radius in this MD simulation was set to 12Å.

To investigate existence of solid and liquid phases in the system we used the Lindemann index that was calculated as follows [60]:

$$L_i = \frac{1}{N-1}\sum_{j(j\neq i)} \frac{\sqrt{\langle r_{ij}^2\rangle_T - \langle r_{ij}\rangle_T^2}}{\langle r_{ij}\rangle_T} \qquad (5)$$

$$L = \frac{1}{N}\sum_{i} L_i \qquad (6)$$

Where L_i and L are the Lindemann index of ith atom and whole particle, respectively, $\langle ... \rangle_T$ denotes the average at temperature T over time, r_{ij} is the distance between two atoms i and j. As is well known, Lindemann index equal to 0.1 is a criterion to distinguish solid and liquid phase. If the Lindemann index of an atom or a particle is below 0.1, it is in solid state while the Lindemann index above 0.1 represents high mobility liquid phase.

It is worthwhile to emphasize that the Lindemann index revels the mobility of atoms. Liquid atoms has higher mobility than solid atoms; however, it not necessarily true that any high mobility atom has liquid physical state. For example, the solid atoms show high mobility when they flow during plastic deformation or under impact. In other word, The Lindemann index is able to distinguish between solid and liquid state in when the system is in equilibrium condition and external stimulus dose not influence the atoms.

Chapter 4

Oriented attachments of hexagonal and triangular silver nanoplates

Nanojoining is a challenging but essential step in the nanotechnology for assembly of nanoscale building blocks into 2D or 3D structures[55]. It is well known that individual atoms may apply attractive or repulsive force on each other depending on their distances, and the atoms in a crystal network will try to find a stable position for themselves in which the net force on each atom becomes zero[86]. Obviously, the most stable configuration of atoms in a crystal is the lowest energy configuration. In this regard, if two particles with clean uncovered surfaces meet each other, they could join to reduce their excess surface energy[55, 87]. However, how nanoparticles joined together at low temperature is still unclear. Solid-state bulk and surface diffusion of atoms at a temperature below half of the melting point of bulk material is very slow, because there is not enough energy in the system. In sharp contrast, sintering of nanoparticles can occur at a temperature as low as 0.2 to 0.4 of the melting point [64, 88, 89]. Thus, clarification of the nanojoining mechanism is critical in the assembly and joining of nanomaterials.

Nanoparticle self-assembly and joining has been reported in the literature [3, 7, 47, 48]. Sun et al reported that it is possible to transform silver nanospheres to nanobelts through self-assembly of the nanoparticles and subsequent thermal treatment to remove adsorbed surface molecules and sinter the particles[39]. In another research, Tang et al reported organization of CdTe nanoparticles to nanobelts, in which after partial removal of thioglycolic acid stabilizer layer of the colloidal CdTe nanoparticles by methanol, the CdTe nanoparticles attached to each other and made crystalline CdTe nanobelts[49]. It is interesting that individual CdTe nanoparticles coalesced to become a single crystal. The authors suggested two different mechanisms: one is Oswald ripening and the other is the direct fusion of the particles for single crystal formation [39, 50, 51]. However, the mechanism of orientation was not discussed and a dynamic procedure transferring fused nanoparticles into single crystals was not clarified. Kalsin et al reported that silver and gold colloidal nanoparticles could join to each other to form a diamond-like lattice structure [52]. They showed that these nanoparticles created unusual binary crystals through electrostatic self-assembly and could join to each other at room temperature to make crystalline particles. Recently, Zhang et al reported self-assembly of silver nanoparticles at room temperature which led to a 2D array ultrathin film of silver nanoprisms on the glass substrate, providing

a tunable Plasmon response property [53]. These experimental researches show the importance of nanoparticle joining especially at low temperature.

There are several numerical and theoretical studies on the joining of nanoparticles, but their focus has been in investigation of some unusual behavior of the material at the nano-scale such as melting point of nano materials or surface premelting that is used to explain nanoparticle sintering[57-61, 90]. Surface premelting and size dependent melting behavior in nano scale were usually employed to explain nanoparticle joining. A good example of these theoretical studies is one by Hu et al concerning low temperature sintering of silver nano particles for flexible electronic packaging [72]. They employed a Monte Carlo simulation to support their experimental results. Size dependent behavior of the silver nano particles was the goal of their model, which was employed to explain low temperature joining and high temperature application of the silver nano particles as electronic packaging. Detailed results of Monte Carlo simulation of sintering of silver nano particles were published by Guo *et. al.*[63]. They showed that small silver clusters could join to each other even at 0.01K. At a higher temperature, attachment and initial joining were followed by sintering of the particles because of the diffusion of atoms. Although Monte Carlo is a simple and powerful method for prediction of the most probable state of a system regarding minimization of the energy of the system, it is not suitable for explanation of the dynamic sintering process. Because, in this method of simulation, the most stable configuration for atoms of the system is found based on a random change in atomic positions and comparing the energy change of the two configurations[64]. On the other hand, the size of the biggest particle in their research was less than 1 nm. Qi et al shows that the cohesive energy of the particles is size dependent [24]. They developed a model to explain cohesive energy of particles as a function of the particle size. Based on their model, cohesive energy of a spherical particle can be calculated using the following equation:

$$E_p = E_b\left(1 - \frac{d}{D}\right) \qquad (1)$$

In this equation, $E_p$is cohesive energy of the spherical particle, E_b is cohesive energy of bulk material, which is equal to 284 KJ/mol for silver [24], d is equal to atomic diameter, which is equal to 0.288 nm for silver and D is the diameter of the nanoparticle. Equation (1) shows when the particle diameter becomes around 1nm or less, the effect of size on cohesive energy of the particle becomes very important. It means changes in total energy of a particle are not linear and extrapolation of the modeling results for sub-nanometer particles to bigger ones is not accurate. Therefore, another simulation method providing the detailed explanation should be employed to clarify mechanisms of nanoparticles joining.

In this research, we employed a Molecular dynamics (MD) simulation method to study room temperature nanoparticles joining. Since silver nanoparticles have attracted intensive research efforts because of their interesting applications, we selected hexagonal and triangular silver nanodisks for MD simulation. The aim of this research was clarification of joining of the particles at a temperature range below half of the melting point of material when there is not surface premelting of the particles. To study the joining mechanism, we perform MD simulation at three different temperatures: 1K, 300K, and 500K. 1K is low enough to deactivate thermally activated mechanisms of joining. 300K is room temperature, which is our focus, and 500K is the highest temperature before surface premelting that can affect the joining mechanism. The room temperature joining mechanisms was validated with experimental observations of synthesized, self-assembled and joined hexagonal and triangular silver nanodisks.

4.1 Simulation and Experimental

4.1.1 Simulation.

A hexagonal and a triangular particle were designed; and MD program was run for each particle for 50000 time steps to get equilibrium. The hexagonal particle consists of 1785 silver atoms and the triangle consists of 1288 atoms. In this research, hexagonal nanoparticles were used to show joining in edge-to-side configurations while triangular nano particles were used to show joining. Triangular silver nanoparticle in side-to-side configurations was selected for side to side joining, because of their simple structure at the edges [21]. However, the corner atoms of these particles are not stable because of the sharp angle of the corners of triangle; hence, they are not suitable to show edge to side joining. Therefore, we selected hexagonal silver nanoparticles to observe side to edge joining. In addition, we will report joining of a triangular and a hexagonal particle. To simulate joining in all of the cases, the particles were put far away from each other, which means a distance larger than the cut off radius and the MD program was run for 20000 time steps before joining. During these 20000 time steps, two particles reached equilibrium and initial potential energy of the system could be calculated. After that, the particles were put in close to each other to join freely without any pressure or impact. The distance between nearest points of the particles in this condition must be less than the cut off radius of the atoms and not too close to push each other away. In this situation, the atoms apply attractive force on each other, the particles become closer and closer, and finally, the joining starts. In this research we selected 1K as the lowest temperature in which thermal energy of the system is very low and the thermally

activated process of joining such as surface or bulk diffusion cannot play a role in joining, because the surface and bulk atoms have not enough energy to diffuse. Our focus in this research was room temperature joining, which was modeled at 300K. Finally, we did simulation at 500K to investigate role of thermal energy of atoms on the joining.

4.1.2 Synthesis and characterization of silver nanoparticles joining

To synthesize, self-assemble and join silver nano particles, 2.1 g of $AgNO_3$ (Sigma-Aldrich) was added to 60 ml H_2O and agitated by ultrasonic bath for one minutes to dissolve $AgNO_3$ powder. At the same time in another beaker, 0.68 g Ascorbic acid (Alfa Aesar) and 0.16 ml Poly (methacrylic acid, sodium salt) 40% in water (PMAA) solution (Aldrich Chemistry) were added to 200 ml H_2O and agitated by ultrasonic bath for one minutes. Synthesis was started by pouring silver nitrate solution into reducing solution while it was agitating in the ultrasonic bath.

To prepare samples for SEM and TEM observations, two min after adding silver nitrate solution to reducing agent, 0.5 ml of this suspension was added to a solution that contained 0.1 ml of PMAA in 3 ml of H_2O. This suspension was agitated in ultrasonic bath. After 5 min agitation, 0.1 ml of this suspension was added to 3 ml distilled water. This dilute suspension stirred for five minutes with a magnetic stirrer to wash the surface of the silver nano particles from polymer molecules to get better conductivity. 0.02 µl of this dilute suspension was poured on a clean silicon wafer and dried at 70°C. TEM samples were prepared from the same suspension. One drop of the suspension was poured on a TEM grid and after drying, the grid was used for TEM observation.

4.2 Results and Discussion

Figure 4-1 shows the simulation results at 1K, which was done to check what happened in side-to-side configuration joining of triangular silver nanoparticles when the thermally activated mechanism of sintering such as diffusion was deactivated. Figure 4-1-a shows the triangular nanoparticles just after they were put near each other in a small 3D misalignment (around 5^o) before attachment. After first touch at the nearest point of the two particles, they rotated (the left hand side particle counterclockwise and the right hand side particle clockwise) and aligned as shown in Figs 1-b and 1c respectively. The rotation occurred to make the edges of the particles parallel for a complete contact. Final configuration of the particles after joining is presented in Figure 4-1-c and d from two different views. In this simulation, the particles made a joint at the edge and no more progress was observed. There was a crystallographic orientation between the two particles after joining. As seen in d, three (111) planes of

the left hand side particle were aligned with a few atoms of the right hand side particle. However, the alignment was restricted only to the joint area and these particles made a line contact. Figure 4-1-e shows the potential energy change of the system during this simulation. The energy of the system corresponding to Figure 4-1-a, b and c are marked on this figure. Figure 4-1-e reveals that the potential energy of the system reduced by around 15eV, which is the driving force for joining of the particles. In Figure 4-1-c and d, it is shown that around 30 atoms participated in this joining sequence. The binding energy of silver in fcc crystal is about 2.6 eV for each atom [91]. Therefore, the total energy reduction of the system in the boundary area was around 19.2% of total energy of these atoms if they were in the bulk.

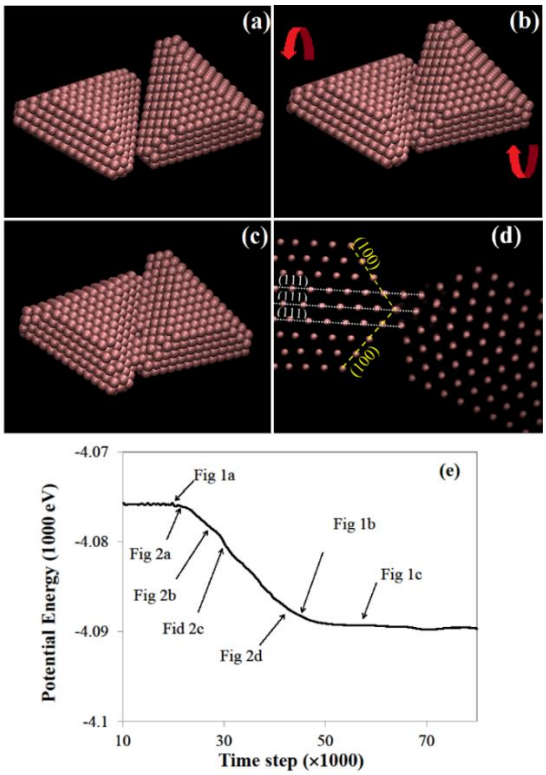

Figure 4-1: Joining of two triangular nanodisks at 1K: a) Initial contact; b) After 45000 time step, the arrows show the rotation direction of the particles; c) Final configuration of the particles, after 57000 time steps (top view); d) Structure of interface, the lines show local aligned of atoms at the interface; e) Potential energy change of the system, corresponding energy of the snapshots of Figure 4-1-a to c and Figure 4-2-a to d are pointed.

To explain the joining mechanism, a close view of the movement of atoms during joining is presented in Figure 4-2 and corresponding energy of each snapshot is marked on Figure 4-1-e. During joining, atoms of the edges of the particles moved to find the most stable position. Figure 4-2-a shows the edge of two particles when they were near each other, before joining. In this image, four atoms were marked to trace their movement during joining. Figure 4-2-b is a snapshot after 8000 time steps. In this figure, the atoms came out of their positions in the right hand side crystal and went toward atoms in the left hand side. Figure 4-2-c is a snapshot after 12000 time steps showing that the atoms were trying to find their stable positions in the crystal network at the left hand side. The atoms number one, two and three went to the backside of their adjacent atoms from the left hand side particle and atom number four went to the front of its neighbors. As mentioned, the atoms migrated to new positions because of the attraction between them and rearranged in a new configuration based on the initial orientation of the particles. Figure 4-2-d shows final configuration of atoms after 27000 time steps. As seen, the atoms were arranged in new crystal positions and their neighbors in the right hand side followed the migrated atoms and rearranged themselves. Obviously, movement and rearrangement of atoms were done to decrease the total energy of the system that can be seen in Figure 4-1-e.

Our simulation revealed that even at 1K, the surface atoms of silver nanoparticles can move and make a contact between two particles because of the attractive forces that exist between the atoms when their distance is less than the cut off radius of the MD simulation. Since the temperature of this simulation is very low, diffusion is inhibited. Only the joint in line contact is formed by rearranging of surface atoms. This occurs through short movement of the atoms (5-10 Å) under columbic attraction of the adjacent surface atoms of the other particle to reduce the excess energy of surface atoms. Migration of the surface atoms imposes elastic strain that leads to small rotation of the particles. Nanoparticle joining at 1K as reported here is consistent with previous Monte Carlo simulation results that showed at 0.01 K the silver clusters can join [63] and further, we provide a clear explanation for the mechanism of joining.

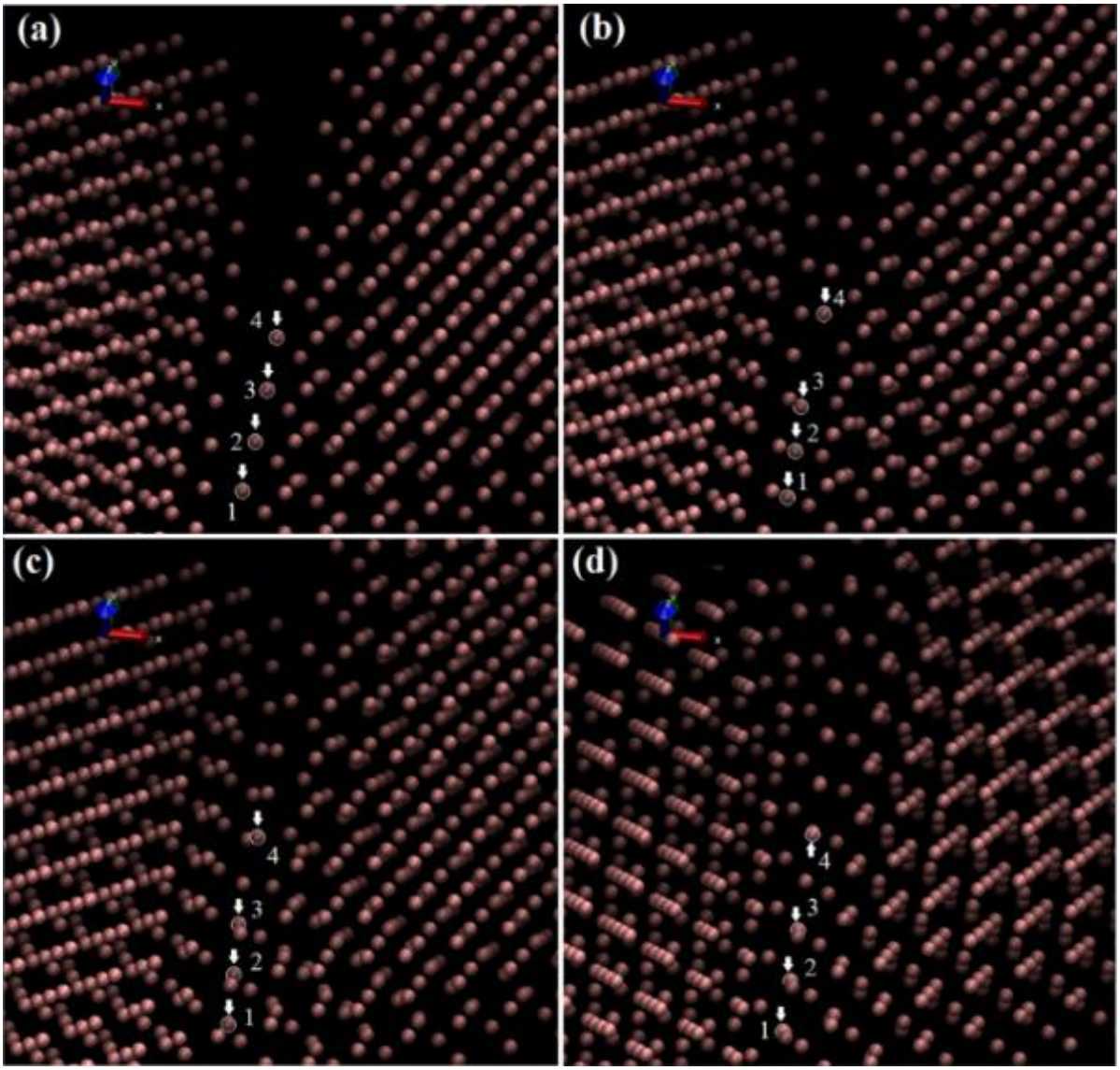

Figure 4-2: Rearrangement of atoms at the interface between two nanodisks during joining at 1K; a) Before joining; b) 8000 time step after first touch; c) 12000 time steps after first touch d) Final configuration of atoms.

The second simulation was performed at 300K for the same configuration of triangular silver nanoparticles (Figure 4-3). Potential energy change of the system during joining is presented in Figure 4-3-a. Similar to the previous case at 1K, the potential energy of the system reduced through the joining of nanoparticles. However, this curve did not present a simple decreasing curve like the 1K result (Figure 4-1-e). To elucidate this complex behavior, joining progress has been monitored at

different stages. At the beginning, the particles touched each other by attractive forces that existed between them, which led to some reduction in total energy of the system (Figure 4-3-b). After 4000 time steps, nanoparticles completed their initial joining which means the edges of the particles were in a line contact, completely (Figure 4-3-c). The joining process was accomplished through a short movement of surface atoms of the right hand side particle toward the edge atoms of the left hand side particle, same as what was revealed at 1K (Figure 4-2). Similarly, when the atoms at the joint area changed their atomic position and built new aligned structure at the interface, their neighbors in the crystals tended to follow them. This means that the particles were deformed elastically. This elastic deformation induced elastic energy in the nanoparticles. Excess elastic energy of the system, which is shown on the energy curve (Figure 4-3-a) with a circle, was released through first rotation of the particles within the next 10000 time steps. The direction of rotation of the particles is shown in Figure 4-3-c by a counterclockwise arrow for the left hand side particle and a clockwise one for the right hand side nanodisk. Configuration of the particles after 38000 time steps is shown in Figure 4-3-d and e from two different views. Looking at the backside of the interface (Figure 4-3-e), it is shown that a gap existed between two particles at the joint area that is marked by an arrow. The surface atoms of the particles in the sides of the gap attracted each other. Therefore, they moved toward each other and filled the gap. During MD simulation from 38000 to 49000 time steps, the gap was filled. Fig3e shows the particles after gap filling. During this process, a little out of plane rotation was seen in the particles due to elastic energy release in the system. Rotation directions of the particles are marked at Figure 4-3-e. The gap-filling process induced additional elastic energy to the system that was released by second rotation of the particles. This energy release is shown in Figure 4-1-a from 49000 to 56000 time steps. The arrows in Figure 4-3-f show particles' rotation directions. Figure 4-3-g presents the final configuration of the particles after joining.

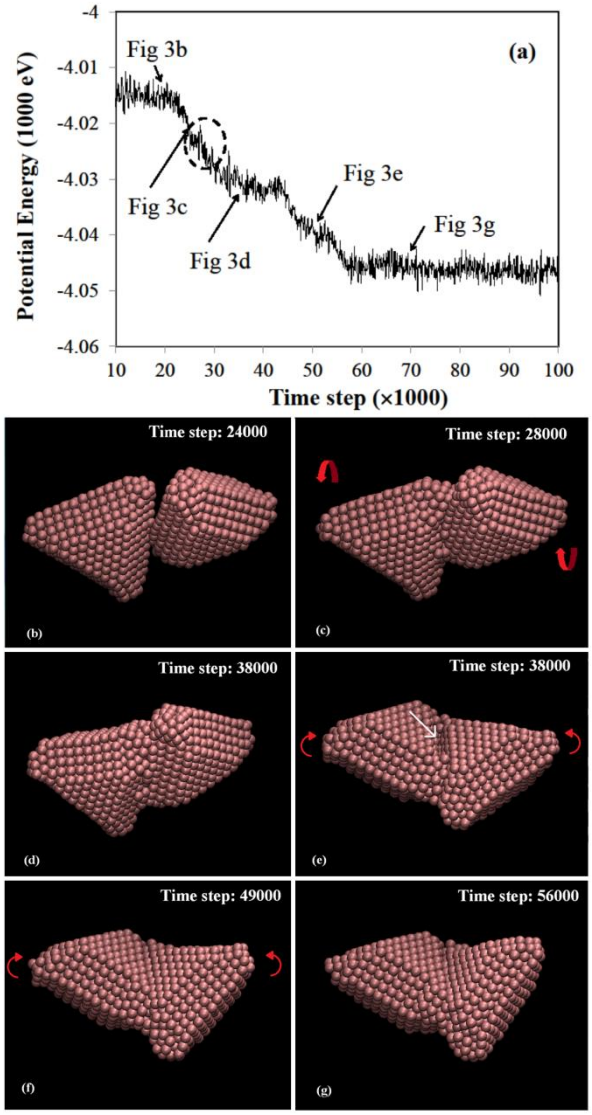

Figure 4-3: Joining of two triangular nanodisks at 300K; a) Potential energy change of the system, corresponding energy of the snapshots of Figure 4-3- b-g is pointed on the graph; b) First contact of nanodisks; c)Line contact of nanodisks, the arrows show the rotation direction of the particles; d)Nanodisks at first step of joining; e) Gap at the Interface, the straight arrow points the gap between the particles, round arrows show the rotation direction of the particles; f) Nanodisks after gap filling, the arrows show the rotation direction of the particles; g) Final configuration of the particles.

To clarify what happens for two nanoparticles after joining from crystal structure point of view, we reduced the size of the atoms in the visualization software to see the crystal structure of the new particle after joining. A cross section of the particles is presented in Figure 4-4. As shown, the particles were

aligned very well during the joining. Dashed lines show twin planes of the triangular nano disks [19]. As shown in Figure 4-4, (111) planes on the upper half part of the particles above dash lines on the Figure 4-4 were aligned. It is worthwhile to emphasize that there are some irregularities at the bottom of the presented image of the particles in Figure 4-4. These irregularities come from the sharp corners of the triangular particles. The corners' atoms have very high energy and high mobility. Hence, the corners of the particles lost their regularity. For better clarification, this part of the crystal is marked on the added image to Figure 4-4.

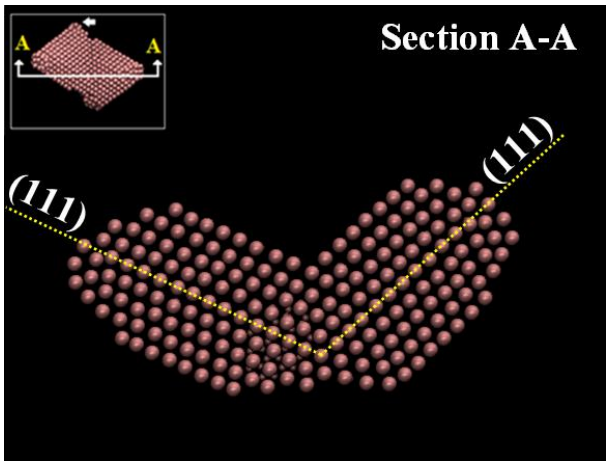

Figure 4-4: Crystal structure of A-A cross section of two nanodisks after joining at 300K; (111) planes above dash lines were aligned.

Our MD simulation at 300K showed an out-of-plane rotation during joining. This rotation was found to be dependent on the geometry of the edge of the particles. The sharp edges of the triangular and hexagonal silver particles can be flattened by increasing the thickness of the particles. In this condition, the edges of the particles have a hcp crystal structure[21]. To investigate effect of flattened edges of the nanodisks on rotation of the particles, we modified the edge of the triangular silver nanoparticles through deleting outer row of atoms from the middle plane of the particles and re-ran the simulation again. Figure 4-5-a shows the particles before joining at 300K. Arrows in this figure point to flattened edges of the particles. After joining, these two nanoparticles showed a different configuration (Figure 4-5-b) in comparison to the previous case as shown in Figure 4-3-g; two particles joined to each other without such rotation. Figure 4-5-c shows alignment of (111) planes of the nanodisks at the interface. Comparison between Figure 4-5-c and Figure 4-4 reveals that in both case [111] directions

of the nanodisks aligned at the interface. The presented result in Figure 4-5 proved that the surface plane of the edge of the particles plays an important role in final configuration of the joined particles while alignment direction of the particles follows the same crystallographic orientation. In other words, rotations were done because the particles wanted to align in a certain crystallographic direction that is [111]. These kinds of rotations during joining of nano particles are also reported in other simulations [63]. It is important to mention that this out-of-plane rotation was not observed at 1K since the particles have not enough energy to extend their interface by rotation.

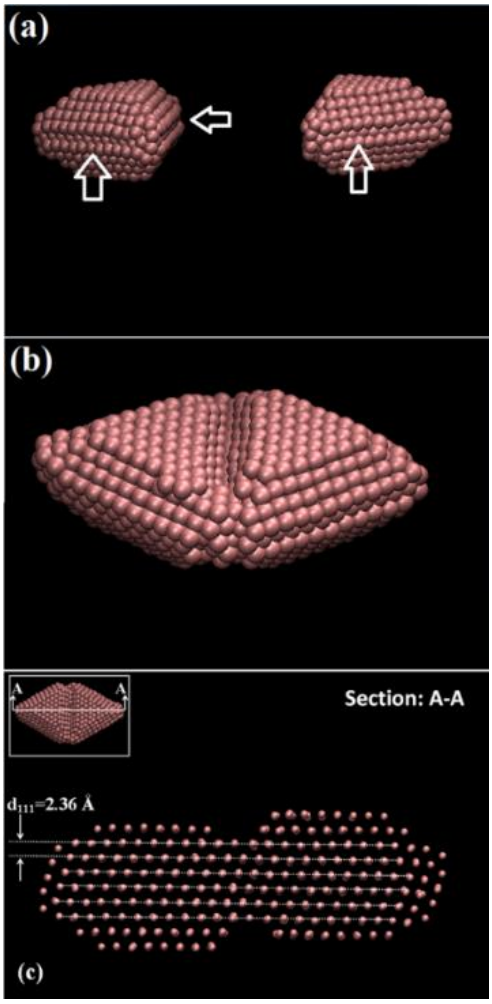

Figure 4-5: Joining between two flat-edge triangular nanodisks; a) Before joining, the arrows pointed the flattened edges; b) After joining; c) Alignment of crystals after joining.

Not only the structure of the particles at the edges, but also their contact direction, can affect the joining of the particles. We further investigated the effect of contact direction of the particles on the final configuration and crystal structure of the joint area because of its potential importance in the joining. To do that, we simulated the joining between two hexagonal nano particles at 300K in edge-to-edge configuration. Figure 4-6-a shows the configuration of the particles in early stage of joining where first contact of the particles took place. Surface atoms of these two silver hexagonal nanoparticles were moved in the interface toward lower energy positions and other atoms followed them. During these migrations of atoms, we observed an edge dislocation that was created in the interface between the particles as shown in the circled area in Figure 4-6-b. However, the dislocation moved out of the crystal as shown in Figure 4-6-c. Finally, this dislocation reached the surface and made a step. These steps are pointed by arrows in Figure 4-6-d. Final configuration of the particles is shown in Figure 4-6-e where the plastic deformation step can be seen in both particles near the boundary, which is created through dislocation movement out from the particles. Figure 4-6-f shows the complete alignment of the particles after joining. Note that the dislocations are created because of crystal mismatch at the interface when the particles reach each other. The same mismatch can be observed in joining of the triangular nanoparticles.

As shown in Figure 4-6, MD simulation revealed that nucleated dislocations at the interface are not stable and will move to the surface. Instability of dislocations in nanoparticles has been reported previously. For example, the strengthening mechanism of metals changes from Hall-Petch to inverse Hall-Petch softening at nano grain metals because of the instability of dislocation arrays in nano-size crystalline materials[92]. Not only nano crystalline metal, but also nano-size individual particles' defects are affected by the size of the crystal. Liu et al showed that when the size of iron nano particles became less than a critical value, dislocation core could not be stable in the iron nanoparticles [93]. In another research, Schallet al by using a continuum model and experimental observation showed that there is a critical radius for the particles below, which dislocations cannot be stable in the particles[94]. Jose-Yacaman et al claimed that partial dislocations can be stable in nano particles[95] and Carlton et al showed that stacking fault and twin defects might be stable in nanoparticles while they are rare in coarse grain material[96]. They claimed that these defects are stable in nano structured material because of the stability of partial dislocation in nano scale. Our modeling results are consistent with these results: hexagonal and triangular nanoparticles have stable stacking faults[95, 96]; meanwhile dislocations at the nanodisk interfaces were not stable and moved to the surface of the nanoparticles [92, 93].

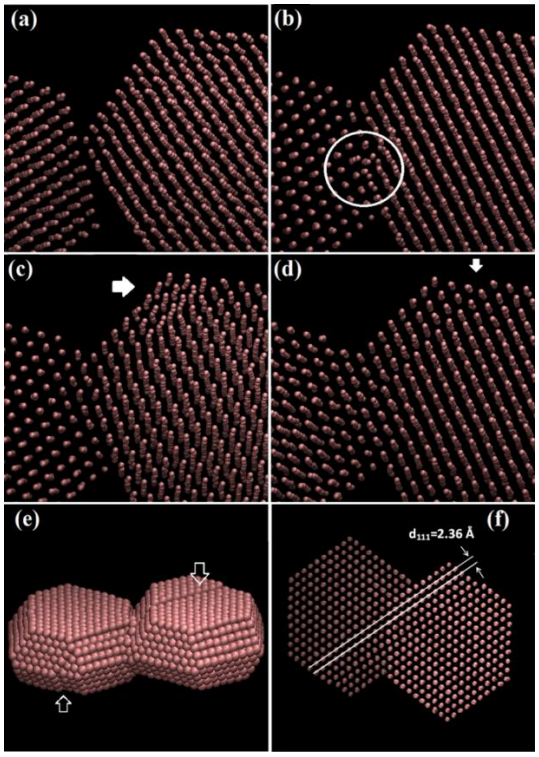

Figure 4-6: Hexagonal nanodisks joining at 300K; a) Initial contact; b) Interface structure at 22500 time steps, generated dislocation was circled; c) Movement of dislocation; d) Final interface structure; e) The nanodisks after joining, the arrows show the plastic deformation in the particles; f) Crystal alignment of the particles after joining.

To investigate the possible phase transition during joining of particles, joining of two triangular nanoparticles at higher temperatures was studied. The Lindemann indices of the particles before joining at different temperatures are reported in Figure 4-7-a. As shown in this figure, the Lindemann index of the particle is less than 0.1 at 500K and lower temperatures. This indicates that the joining procedure at a temperature lower than 500K is based on a solid-state diffusion. In addition, the Lindemann indexes as a function of the distance to the center for all of the atoms of a triangular nanoparticle at 1K, 300K and 500K were presented in Figure 4-7-b, c and d respectively Figure 4-7-b and 7c show that all atoms of the nanoparticle (surface and bulk) at 1K and 300K are in solid state since the Lindemann index of all of the atoms are below 0.1. However, at 500K (Figure 4-7-d), it can be seen that a few atoms located on the vortex of the triangle have Lindemann index higher than 0.1. High Lindemann index of these five atoms demonstrates that they had higher mobility. This is an evidence for high mobility surface

atoms. High mobility of these atoms seems reasonable because of the missing neighbors of the atoms at the sharp corners of triangles. Although few atoms were of high mobility, most of the atoms of the particles were in the solid state. Thus these high mobility atoms would not affect joining of the particles too much and it is reasonable to state that the joining was done in solid state. However, it is expected that with increasing temperatures the number of the high mobile atoms will reaches a critical value and trigger a local phase transition. If that occurs, the joining will be the combined effect of both solid state diffusion and liquid phase sintering. The further detailed study at a higher temperature is under way.

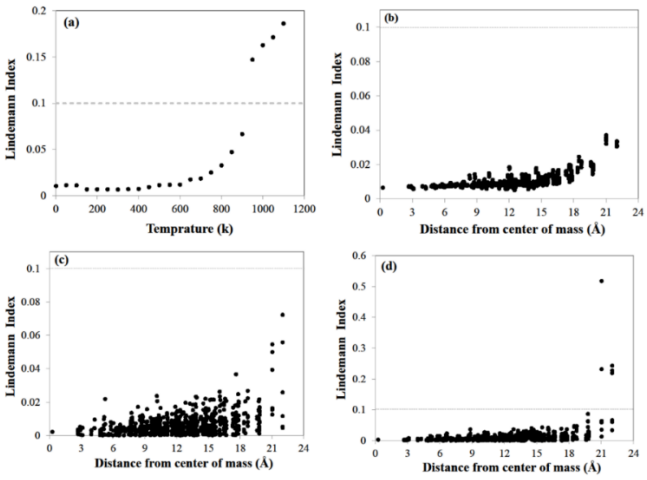

Figure 4-7: a) Lindemann index of a triangular nanodisk at different temperatures; b) Lindemann index of atoms of the triangular nanodisk at 1K; c) Lindemann index of atoms at 300K; d) Lindemann index of atoms at 500K.

Figure 4-8-a-d show different views of the final configuration of the particles after 200000 time steps. Our modeling reveals that the joining procedure at 500K was same as 1K and 300K, but shape of the initial structural blocks (triangular nanodisks) were changed during joining. The atoms at 500K had high mobility because of increasing kinetic energy of the system by increasing temperature. In other words, silver is very soft at higher temperature and induced energy in the system during joining can deform particles. Therefore, the interface of the nanodisks extended and consequently, the strength of the joint is higher than other joining at lower temperature. The strength of the joints between nanoparticles is important in some applications and high temperature solid state joining can be applicable in this kind of applications although the shape of the structural blocks have changed.

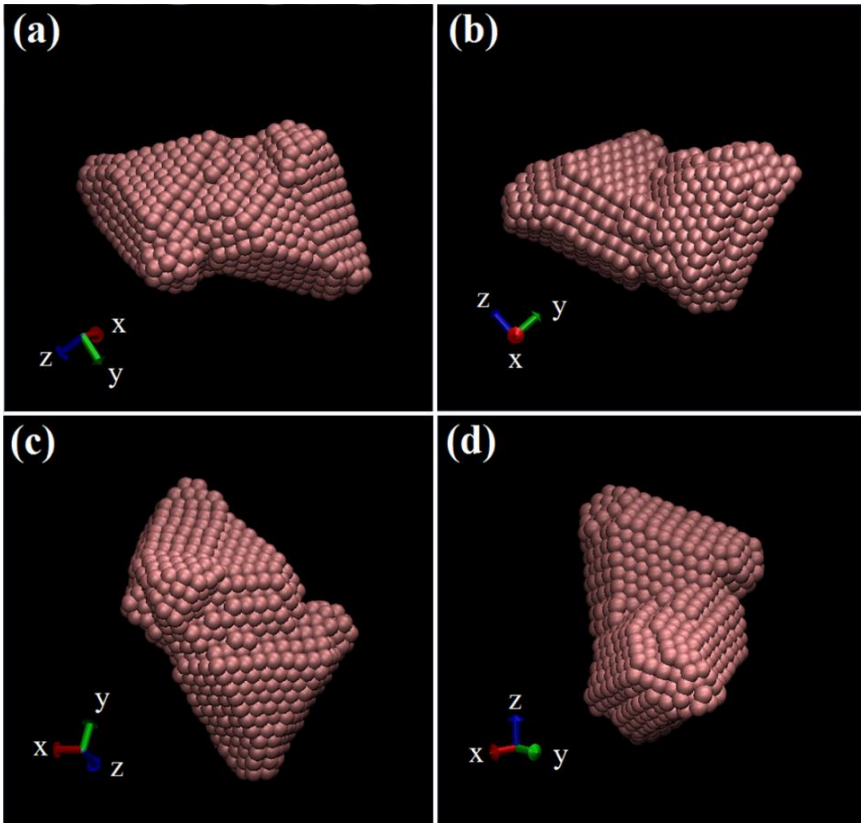

Figure 4-8: Final configuration of the silver triangular nanodisks after joining at 500K from different views, the coordinate axes on each image shows viewing direction.

To compare the joining process at different temperatures, potential energy changes of the system during simulation at different temperatures were presented in Figure 4-9. As it was explained, potential energy of the system has decreased due to joining. The noisy nature of the curves at 300K and 500K is related to kinetic energy of the system. When temperature increased, the atoms vibrate and during vibration the distances between the atoms change randomly and this leads to some noises that superimpose on the potential energy of the system. As shown in Figure 4-9-a, the joining process at 300K takes more time to become stable. In comparison to 1K, joining of the particles at 300K is more complicated and leads to larger area in the boundary between the particles and hence, takes more time to complete. This fact can be easily understood when comparing Figure 4-1c and d, and Figure 4-3-f and Figure 4-4. On the other hand, joining at 500K is faster than 300K because of the higher thermal energy of the system that helps the atoms to move faster and even diffuse on the surface or in the bulk. To compare the change in energy of the system through joining at different temperatures, the changes

in potential energy of the system at different temperatures with respect to the initial potential energy of the systems before joining at the same temperature were plotted in Figure 4-9-b. This figure reveals that the potential energy drop during joining at 300K is more than those at two other temperatures. In comparison to the 1K, the energy reduction of the system through joining at 300K is higher because of the larger joint area compared to the line contact joint at 1 K (Figure 4-1-c, Figure 4-3-f and Figure 4-4). At 500K, the particles deformed during joining as shown in Figure 4-8. These deformations create new surfaces. In contrast, joining at room temperature shows perfect alignment of the atoms. Hence, the total energy drop in 500K is less than 300K when the crystals did not align well at 500K.

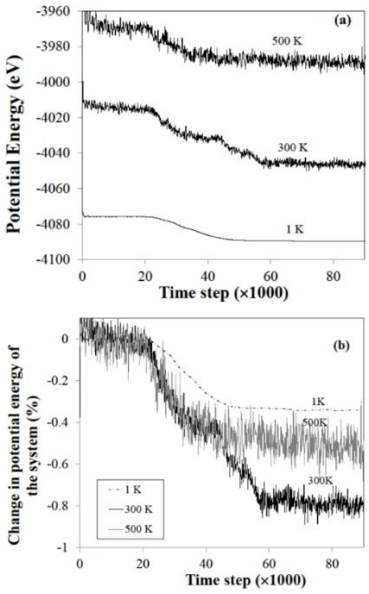

Figure 4-9: a) Potential energy change of the system during joining at 1K, 300K and 500K; b) Normalized potential energy change at 1K, 300K and 500K versus simulation time

Both triangular and hexagonal nanoparticles are synthesized in an experiment. Therefore, their joining is predictable and should consider for simulation as a real case. Figure 4-10 shows MD modeling result of joining between a hexagonal and a triangular silver nanoparticle. The edges of two particles were parallel at the beginning of joining as it can be seen in Figure 4-10-a. However, it is clearly shown in Figure 4-10-b that the particles rotated while they migrate toward each other. The arrow in Figure 4-10-b shows the rotation direction of the triangular nanoparticle. Figure 4-10-c shows the nanoparticles after joining. As it can be seen in this figure, the particles rotated and joined in a corner-corner configuration. Figure 4-10-c shows that the (111) plane of the triangular particles is aligned with the (111) plane at the edge of hexagonal nanoparticle which is compatible with other joining of

triangular particles and hexagonal particles that are showed in Figure 4-6-f and Figure 4-4. Figure 4-10-d demonstrates the perfect crystal alignment between the joined hexagonal and triangular silver nanoparticles by decreasing size of the ball with visualization software. The image viewed perpendicular to the (111) plane of the hexagonal particles, indicates that the triangular particle rotated and aligned with the (111) plane at the edge of hexagonal nanoparticles.

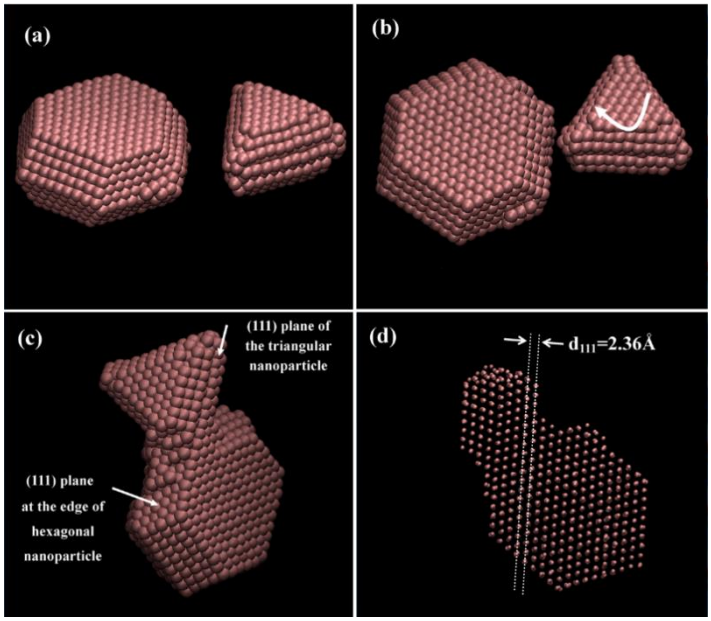

Figure 4-10: joining of hexagonal and triangular nanoparticle; a) initial configuration of the nanoparticles at the start of joining; b) rotation of the particles before joining; c) corner to corner join and alignment of the nanoparticles; d) crystal structure of nanoparticles after joining.

The rotation of nanoparticles during migration of the particles before joining that depicted in Figure 4-10, shows the importance of nanoparticle's geometry and its impact on the self-assembly of the particles. The Lindemann index of atoms of triangular nanoparticles presented in Figure 4-7 shows that the atoms at the corner of the triangular particles have a higher mobility, which means a higher energy in comparison to the atoms inside or at the surface far from corners. High energy levels of the atoms at the corners of triangular particle leads to a higher tendency of these atoms to join to their neighbors to reduce their energy levels. Therefore, during the migration of hexagonal and triangular particles, the higher attraction force at the corners drives the particle to rotate and creates contacts at high-energy corners. Therefore, it can be deduced that the shape of nanoparticles and its effect on the energy of the surface atoms are the important parameters in the self-assembly of the particles. It is worthwhile to emphasize that this case is still a special configuration for joining of the hexagonal and

rectangular nanoparticles. Other parameters such as the sizes of particles, their initial velocities when they approach to each other, absorbed surface molecules and so on, can affect the self-assembly of the particles and should be taken into account.

Overall, the MD simulation shows that the silver nanodisks are able to join to each other even at 1K by movement of the surface atoms because of atomic attraction. These movements of atoms occurred because of the high energy of surface atoms at a nano scale [22, 23, 25, 97]. The surface atoms of nano particles are excited and their bond with other atoms is weaker than surface atoms of micron size particles, which means their energy is higher than surface atoms of micron size particles[42]. Therefore, when two nanoparticles become enough close and their surface atoms attract each other, this attraction force can be enough strength to pull out them from their position on the surface and guide to a new position. Hence, the atoms make a new bond and reduce their energy. This energy release is the driving force for movement of atoms and joining. On the other hand, continuity of the crystals in solid state leads to rearrangement of the neighbors of the migrated atoms. These fast migrations of atoms store elastic energy in the system through elongation of the atomic bonds around the jumped atoms. This excess energy will be released through elastic or plastic deformation. The joining process is fast and finished within few thousand time steps. Hence, the joining mechanism at room temperature is different from diffusional process, which is the dominant mechanism of sintering at high temperature (above half of melting point of the material). Another important outcome of the simulation is alignment of the crystals after joining at room temperature (300K). In comparison to 1 K, joining of the particles at 300 K has more progress after first atom contact. The mechanism of the first attachment of the particles at 300 K is similar to that at 1 K. However, at 300 K the atoms have more kinetic energy than at 1 K, which means the atoms have more vibration. Therefore, the surface atoms of the particles in the joining area have more chance to move toward each other. Hence, the joining process can show more progress in comparison to joining at 1K. Based on our findings, the interface of joined nanodisks at 300 K will be free from crystal defects and the joining at room temperature serves as the lowest energy condition to the particles in comparison to joining at very higher and lower temperature. As mentioned earlier, room temperature joining and crystal alignment was reported by other researchers [39, 47-49, 51, 98]. They reported that nano particles could assemble and join at room temperature and after joining. In some cases, crystal alignment was also observed. These experimental observations emphasize that the results of our MD simulation are reliable. Therefore, the provided mechanism for low temperature nanojoining can be used to explain how and why nano particles join to each other in different conditions. Another important feature observed in our MD modeling is the existence of different

interface conditions between the particles at different temperatures. At 1K, the interface is restricted to line contact. This type of interface can be employed in some applications such as sensing, because of localized surface plasmonic hot spots [97]. At 300 K, the interface of the joined nanodisk is more extended. This area will be a perfect crystal without usual defects such as dislocations. In this condition, the particles are joined and aligned meanwhile their initial shape remain intact. These interesting features of the nanojoining at 300 K introduce unique and novel morphology for silver in nano scale. From this point of view, 500K is too hot to keep the initial shape of the particles intact. The particles will deform at high temperature solid state joining and the bond between the particles will be strong.

We did some experiments to validate our MD simulation results. To do that, we employed a wet chemical route to synthesize, self-assemble and join hexagonal and triangular silver nanoparticles. Synthesized silver nanoparticles structural blocks are shown in Figure 4-11-a and b individually. It is worthwhile to emphasize that the hexagonal and triangular structural blocks were almost join to each other. Only few individual structural blocks can be observed individual in the product. Crystal structures of the silver hexagonal and triangular nanodisks that were synthesized in the experimental part of this research are well known [19, 21, 99, 100]. In these two kinds of nanodisks, each crystal consists of a twin plane in the middle of the particle. Since the stacking fault energy of silver is quite low, the twin plane can be formed easily. Therefore, the top and bottom planes of the crystal will be (111). The edges of the crystal consisted of (111) and (100) planes. The initial crystal shape will be hexagonal because of the symmetry of fcc structure. These hexagonal nanoparticles will grow to make a triangular shape crystal because of different growth rates in [111] and [100] directions. To synthesize silver structural blocks, we used ascorbic acid as the reducing agent [21, 101]and PMAA as stabilizing\capping agent. PMAA was used as reducing agent to reduce Ag^{+} to Ag by itself; however, as reported by Zhang et al, this process is very slow and needs long aging time[102]. Since our synthesis was very fast and finished in few minutes, it indicates that PMAA cannot function as a dominant reducing agent by attaching to Ag ions, although some silver ions can attach to PMAA. On the other hand, PMAA molecules could attach to the Ag crystals after reduction [103]. The surface atoms of silver particles desired to share their energy and become more stable. Therefore, PMAA molecules may attach to the surface atoms of the small silver particles. Based on published papers and also, the shape of the synthesized silver nano particles that presented in Figure 4-11-a and b, it can be assumed that the PMAA molecules were attached to the (111) planes of initial silver clusters. The PMAA that covered the top and bottom sides of the particles reduced the chance of joining of the particles from the big flat

sides, however they could touch from the edges and join. This is compatible with our edge to edge and edge to corner MD simulation so we could compare the experimental and MD results.

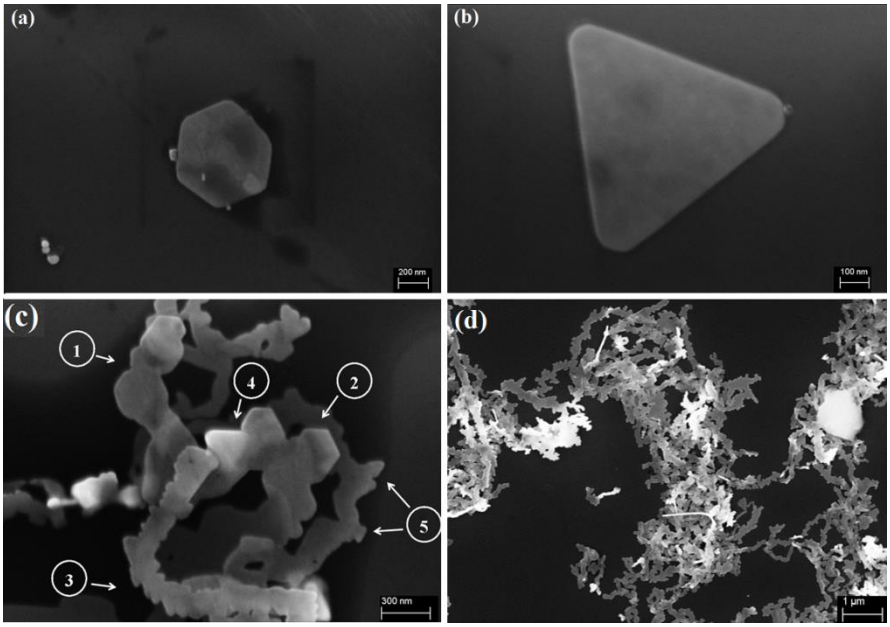

Figure 4-11: a) SEM Images of a hexagonal silver nanodisk; b) SEM Images of a triangular silver nanodisk; c) SEM image of silver nanobelts formed by joining of structural blocks; d) low magnification SEM image of the nanobelts.

SEM images of self-assembled and joined silver nanoparticles are shown in Figure 4-11-c. The hexagonal and triangular silver particles were attached to each other and result in nanobelts. Different joining configurations can be seen in Figure 4-11-c. The marks of "one" and "two" in the figure indicate the positions where hexagonal structural blocks joined to each other. The area marked by "three" shows the triangular structural blocks join together. The head to the corner or edge configuration of these triangular nanoparticles is compatible with MD simulation results that presented at Figure 4-10. The mark of "four" points to the joining of hexagonal and triangular blocks while these blocks keep their initial shapes. Two tri-angular nanoparticles marked by "five" in Figure 4-11-c have been joined in two different configurations to a nanobelt, indicating a random nature of the self-assembly of the structural blocks. Figure 4-11-d shows a low magnification SEM image of nanobelts consisting of the silver structural blocks. This image reveals that the structure and joining configuration shown in Figure 4-11-c are uniformly distributed through the whole sample. These two SEM images prove that the nanoparticles can join to each other at room temperature. This is consistent with our MD simulation results (Figure 4-3, Figure 4-4, Figure 4-5, Figure 4-6 and Figure 4-10). To check the important

alignment feature of the nanojoining at room temperature that was revealed by the MD simulation, we performed HRTEM observation. Figure 4-12-a and b show a HRTEM image of the boundary area between the nanoparticles. Figure 4-12-a reveals two nanoparticles that joined to each other and perfectly aligned. As shown in Figure 4-12-a, the particles were joined and aligned on their (111) planes. The crystal structure of the boundary between two particles was perfect as predicted through MD simulation (Figure 4-6-f). More evidence of the joint morphology is presented in Figure 4-12-b. In this image, five particles were joined to each other and as clearly shown, all of the particles tended to achieve their lowest energy level by aligning their crystal structure, which was predicted by our MD simulation in Figure 4-4, Figure 4-6-d and 6f. (111) planes of five particles are marked in Figure 4-12-b. The experimental outcomes have supported our MD simulation results and show that nanojoining can be considered as a synthesis method to build nanostructures. In addition, the boundaries of the joined particles had perfect crystal structure as predicted by the MD simulations.

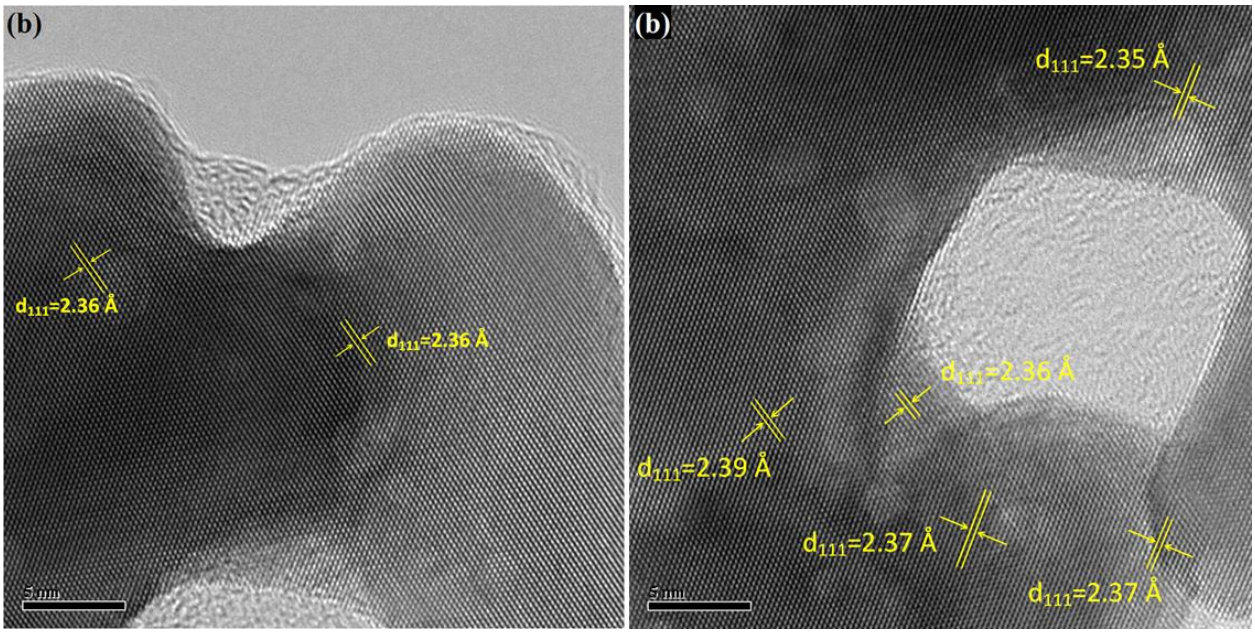

Figure 4-12: a) HRTEM image of the interface area between two joined nanodisks, direction of (111) planes of the particles are marked; b) HRTEM image of five silver nanodisks after joining, directions of (111) planes of the particles are marked.

4.3 Summary

In this research, we have employed molecular dynamics simulation method to study room temperature joining of silver nano particles as an applicable noble material. Our MD simulation has shown that low temperature joining occurred by short movement of atoms to reach lower energy levels. These atoms have forced their adjacent atoms to follow them and impose elastic strain on the crystal structure, which are released through subsequent elastic deformation of the particles. If crystal defects such as dislocations are created in the interface during joining, they will move out and make plastic deformation in the particles and after these events, the final crystal structure of the particles will align and reach minimum energy level. This decrease in the energy of the surface atoms is the driving force for nanoparticle joining at room temperature. Our MD simulations at lower temperature show that the joining can occur even at 1K. However, energy of the system is not sufficient to make a complete joint between the particles. At this temperature, the particles assembled and made a line contact. The mechanism of joining at 1K is short movement of atoms from their position on the surface of a particle toward surface atoms of the other particle followed by subsequent elastic deformation to release stored elastic energy. In contrast, at 300 K, the particles not only make a line-contact joint at beginning, but also the joint grows to cover the whole interface area between two nanoparticles. In this condition, the original shape of the structural blocks will remain intact. This phenomenon is very important for assembled nanoparticles to fabricate nanodevices. At higher temperature (500K), the particles are very ductile, stored energy during migration of atoms is enough to do plastic deformation, and shape of the structural blocks will change. Therefore, the final product is more like sintering of the nanoparticles. Experimentally, synthesized silver hexagonal and triangular nanodisks were self-assembled and joined into nanobelt morphology simultaneously, which is compatible with our MD simulation results. In addition, HRTEM clarified that the interface area of the joined particles is perfect and no dislocations remain in the interface. This observation confirms our MD simulation results that show generated dislocations will move out and the final crystal structure of the joined particles will be perfect.

Chapter 5
Synthesis of silver nanoparticles by self-assembly and nanojoining of nanoplates

Silver has attracted extensive research interest because of its potential applications in nanotechnology and biotechnology [30-36]. The properties of silver nanoparticles, similar to other nanomaterials, depend not only on size, but also on morphology and surface crystal orientation. Researchers have employed various methods for synthesizing silver nanoparticles, including chemical reduction, chemical vapor deposition (CVD) and physical vapor deposition (PVD) [19, 37, 38, 40, 41, 104, 105]. Among them, the solution-based chemical reduction is a simple, low-cost and flexible method. In this synthesis method, it is possible to adjust solution conditions and chemical agents to synthesize various nanoparticles. Strategies for controlling the morphology and the geometry of the synthesized structures are well established: a shape-directing capping agent is employed to change the growth rate in different crystallographic directions [7, 38, 42-44, 106]. Therefore, the surface crystal plane of the nanoparticles is dictated by the choice of capping agent. Thus far, the surface planes of synthesized silver nanomaterials through the solution-based chemical reduction route are mostly (100) planes, although this is not the lowest energy plane in the fcc crystal structure [37, 45]. It is well known that the lowest energy crystallographic plane of fcc crystals is the highly packed (111) plane, which usually forms the surface of stable crystals of fcc structures [41]. In addition, research has demonstrated that (111) planes have better performance in some applications such as catalytic reactions [41]. In this regard, the synthesis of a new grade of one- and two-dimensional silver nanostructures with (111) surface planes is desired.

Among different silver nanoparticles, hexagonal and triangular silver nanoplates are two shapes with maximum (111) planes on their surfaces. Such nanoplates have a twin plane in the center and two (111) planes at the top and bottom surfaces parallel to the twin plane [19-21]. They are synthesized by capping the top and bottom (111) planes with special molecules to reduce the growth rate of the crystal in the [111] direction. Hence, the nanoplates can grow mostly from the edges. When a nanoplate is very thin, its edges are a combination of (100) and (111) planes and when the nanoplates become thicker, a flat hcp layer forms at the edge between the (111) and (100) planes [21]. Different growth rates of silver

crystal in [111] and [100] directions lead to the change of initially hexagonal particles into a triangular form.

The silver nanoplates seem ideal structural blocks for fabricating high stability supercrystals. Based on the literature, a non-classical crystallization mechanism is proposed for supercrystals in which, first the initial structural blocks are synthesized and then, they are assembled and finally joined. The joining mechanism of the structural blocks could be diffusional sintering [75, 107], or a non-thermal diffusion-less, which is called oriented attachment [108, 109]. The product of joining through oriented attachment is usually a defect-free perfect crystal structure at the interface [110]. We examined the oriented attachments of the nanoplates through Molecular Dynamics simulation, which demonstrates how the nanoplates align themselves and join [111]. However, adjusting the affecting parameter of the chemical reaction to achieve a successful synthesis by this method is a challenge.

In this research, the affecting parameters on the synthesis of silver supercrystals by reducing of silver nitride with ascorbic acid in presence of PMAA via the chemical reaction (1) are investigated.

$$2AgNO_3+C_6H_8O_6 \rightarrow 2Ag + 2HNO_3+ C_6H_6O_6 \qquad (1)$$

Based on this chemical reaction, main factors that are able to play role in the synthesis are: 1) the pH of the mixture, 2) the ratio of silver nitrate to ascorbic acid, 3) the reagent concentrations, in the reaction mixture, including that of the capping agent and 4) nucleation of the crystalline silver. The pH in particular is expected to have a significant effect as influences the redox reaction rate and the affinity of the polymer capping agent [112]. Experimental observation and mathematical modeling have applied to investigate the influence of the aforementioned factors on the resultant morphologies of nanostructures.

In this chapter, systematic experimental studies of the formation of silver nanostructures through simultaneous self-assembly and room temperature nanojoining of hexagonal and triangular silver nanoplates is described. First synthesis methods for synthesizing different nanostructures is revealed. Then, the identification of the effect of the key chemical agents of this synthesis method (silver nitrate, ascorbic acid and PMAA) and the synthesis procedure on the shape and morphology of synthesized nanoparticles are explained.

5.1 Experimental procedure and modeling method

5.1.1 Experimental Procedure

First, 0.68 gr Ascorbic acid (Alfa Aesar, 50-81-17) was dissolved into 200 ml H_2O. In another beaker, 1 ml of Poly(Methacrylic Acid, Sodium salt), 40 wt. % solution in water (PMAA) (Aldrich Chemistry) and 100 ml deionized water were mixed by gently shaking (Solution B). Then, 1.6 ml of this solution was added to ascorbic acid solution and mixed to prepare reducing solution (solution B). Then, 2.1 gr of $AgNO_3$ (Sigma-Aldrich) was poured in a 500c beaker and 60 ml of H_2O (except for recipe 9) added to it and gently sway the container to dissolve $AgNO_3$ and prepare the silver nitrate solution (Solution A). When the silver nitrate crystals disappeared, the solution B was poured into this 500 beaker. After five minutes (10 minutes for recipe 9 and 10), the synthesized silver nanoparticles was collected by büchner funnel vacuum filtration.

For SEM and TEM observations, 0.5 ml of nanoparticles suspension was added to a solution that contained 0.1 ml of PMAA solution in 3 ml of H_2O. This suspension was agitated in an ultrasonic bath. After 5 min agitation, 0.1 ml of this suspension was added to 3 ml distilled water. This dilute suspension was stirred for five minutes. 0.02 ml of this dilute suspension was poured on a clean silicon wafer and dried at 70°C for SEM observation. TEM samples were prepared in the same way as SEM samples. One drop of the prepared diluted suspension was poured on a TEM grid and after drying, the grid was used for TEM observation.

XRD analysis with Cu-Kα_1 (λ = 0.154056 nm) was employed to investigate the crystal structure of the products. XRD tests were carried out on a thick film prepared from silver nanoparticles. To prepare the thick film, suspended silver nanoparticles were deposited on a filter paper (Whatman® # 1001042) through a vacuum filtration apparatus after 20 min stirring. The thick film was dried at 70°C. The film was detached from the filter paper by bending of the paper and used for XRD test.

To measure transmittance of the solution during reaction, a photoconductive cell (Parallax Inc., 350-00009) and a LED (Lumex Opto/component Inc., SML-XL1110SOC-BTR) were used. They installed in two standard cuvettes (LIGHTLAB, C-6001) and the cuvettes are fix in a way that the gap between the photodetector and LED was 5 mm. The setup was connected to a data logger to record the data. This setup was placed in the reactor and transmittance of the solution was measured every 5 ms.

5.1.2 Modeling

A predictive model of the pH developed throughout the silver reduction was constructed. The reacting mixture is assumed to be well mixed, and to be at pH equilibrium for every point of the reaction, where the equilibrium point will shift as the relative concentrations and activity of each contributing species changes throughout the reaction. It is also assumed that every species that is in the mixture throughout the progression of the reaction is contributing to the pH equilibrium without sequestration; which is to say that it is assumed that the adsorption of the PMAA by the silver surface has a negligible effect on its buffering capacity, and that the developed dehydroascorbate is stable on the timescale of the synthesis. Ionic strength, μ, is calculated as shown in Equation 2, where c_i represents the molar concentration of an ionic species, and z_i represents the absolute value of its charge. Counter ions related to the PMAA are considered to be localized near the polymer chain and do not contribute to the overall ionic strength, and the self-ionization of water was included in the model. Strong acids and bases are treated as fully dissociated. Ascorbic acid and PMAA.Na are weak acids expected to act as buffers, and both are expected to have their dissociation pK values influenced by the solution ionic strength μ. For ascorbic acid, Ball demonstrated that across the applicable range of total ionic strengths the Henderson-Hasselbalch equation is acceptable when the apparent dissociation constant is varied with ionic strength according to the equation proposed by Ball (Eq. 3), with a pK constant of 4.21 at zero ionic strength [113]. PMAA·Na is a polyelectrolyte, and was treated according to the Katchalsky model (Eq. 4) [114].

$$\mu = \frac{1}{2}\sum_{i=1}^{n} c_i z_i^2 \qquad (2)$$

$$pK' = pK - \ 0.5\sqrt{\mu}/(1 + 0.5\sqrt{\mu}) \qquad (3)$$

$$pH = pKa' + n\ \log((1-\alpha)/\alpha) \qquad (4)$$

In which, α is degree of dissociation of PMAA.Na. For PMAA, Katchalsky and Spitnik reported analytical titration curves of across the range of interest, linearized independently for five ionic strengths [112]. The data presented in a figure by Katchalsky and Spitnik was digitized by image analysis, where it was assumed that distortions by rotation, stretch and shear were applied uniformly to the figure, and the axes were used for scale calibration. The resulting dataset was fit by a linear regression of the form:

$$pH = A + B\sqrt{\mu} + (C + D\sqrt{\mu})\log((1-\alpha)/\alpha) \qquad (5)$$

Table 5-1: Linear model constants for dissociation of Poly(methacrylic) acid, obtained from linear regression of data derived from [112]

	A	B	C	D
Values	6.33324	-1.32015	-1.80890	0.37048
Linearized using:	X_1	X_2	X_3	
	$\sqrt{\mu}$	$\log((1-\alpha)/\alpha)$	X_1X_2	

to be performed on the full set of data [112]. This obtained the model constants presented in Table 5-1. For accurate modelling of the PMAA·Na, the molar concentration and salt substitution of the polyacid needed to be determined. A specimen of the stock PMAA solution was carefully weighed into a cleaned and pre-weighed 20mL glass scintillation vial, and dried under 32 in-Hg vacuum at 80°C for 24 hours. Once dried, the vial was sealed and re-weighed, to determine that the stock solution contained 40.01wt% dissolved PMAA/PMAA·Na. A 19 mg specimen of this dried material was then placed in a TA Instruments Q500 TGA, degraded at 10°C/min to 700°C under nitrogen, cooled to 390°C, then reheated at 10°C/min under air flow to 900°C to drive off the carbon content, leaving only white Na_2CO_3 ash. A molar analysis of the masses determined that the sodium salt substitution of the PMAA carboxylic acid groups was 86.86 mol%. This was treated in the model as 0.8686 mol NaOH strong base being added alongside each mol of PMAA.

To solve the model, the user provided the ingredient amounts intended in the two reactants solutions, the ratio of the two solutions, and a list of desired degrees of silver conversion that the model is to be solved. From these, the program calculates the total concentration of each species present at the degree of conversion being solved. The estimates of pH and the degree of dissociation of ascorbic and PMAA species were initialized at 12 and 0.5, respectively, and the initial ionic strength estimate is calculated. The program then solves for equilibrium pH at this degree of conversion by repeatedly alternating between recalculating the ionization strength and dissociation constants of each buffer species under the current species concentration estimates, and iteratively solving for the current pH estimate based on recalculations of the buffer dissociation from the last estimates of pH, μ, and dissociation constants. The PH was estimated based on the current estimated concentration of hydronium ions, obtained by summation of estimated concentrations for all hydrogen-dissociated species and subtracting the concentration of strong base. The convergence criteria used was that an acceptable pH estimate had been found for that degree of conversion when the difference between two

consecutive pH estimates was <0.001 and the difference between two consecutive μ estimates was <0.0001, concurrently. Once converged, the model would recalculate concentrations based on the next degree of conversion, and reinitialize the estimates as before.

Using data from the above pH model, relative reaction kinetics were calculated for recipes 1-6, based on data reported by Kimura et al., and Moya et al, for the reduction of tris(oxa1ato)-cobaltate(III) by L-ascorbic acid [115, 116]. This makes the assumption that the pH and ionic strength scaling for the two systems is similar, and allows us to compare relative rates on an arbitrary timescale. In accordance with Kimura et al., the rate model equation 6 was used, where K_0 was dependent on pH and ionic strength, and calculated by equation 7 in the range of pH < 4.5. In accordance with the findings by Moya et al., K_0 was considered constant at K0 = -2.69 for 4.5 < pH < 7.5. This relationship was found by comparing the two published datasets, and determining that ionic strength had an insignificant effect in the studied range.

$$\dot{\alpha} = k_0[AgNO_3][L-Ascorbic] \quad (6)$$

$$k_0 = 0.42(pH) - 4.6 \quad (7)$$

5.2 Results and Discussion

5.2.1 Silver Nanobelts

Figure 5-1-a is a typical SEM image of the belt shaped silver particles that synthesized through reduction of silver nitrate by ascorbic acid when we did not add PMAA to the system. The inset illustrates a wavy shape and small side branches of the belt. Figure 5-1-b reveals local structure of a belt with a highly magnified image. This figure reveals that the belts consist of small nanoparticles. Thickness of the belts was found to be around 200 nm (Figure 5-1-c). Based on the IUPAC definition of nano materials, one of the upper size limits of the nano materials is 100nm [117]. Therefore, these silver particles could be named microbelts. Figure 5-1d shows the XRD pattern of the microbelts. It was thereby confirmed that the sample can be indexed as silver, according to JCPDS card number 00-001-1164.

This experiment confirmed that ascorbic acid can reduce silver ions to silver atoms as expected. We evaluated the yield of the process based on the mass balance of silver, which was 99%. However, it is not clear why the silver particles are belt shaped. No chemical was present to play a shape-directing role in this experiment, except ascorbic acid. The ascorbic acid molecule has a carboxyl group and two

more carboxyls could be generated after reaction of this molecule with silver nitrate [118, 119]. On the other hand, it is well known that the carboxyl group can attach to the surface of silver nanoparticles [120]. Therefore, it is likely ascorbic acid has played a shape-direction role to synthesize microbelts, although further investigation is needed to directly confirm this.

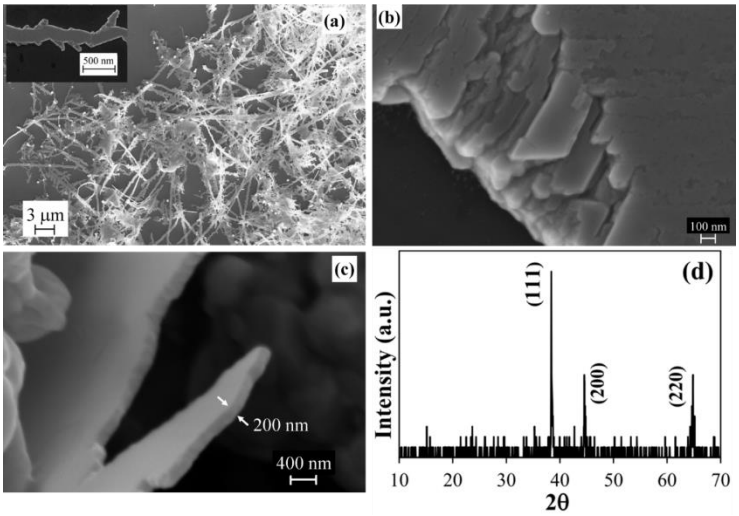

Figure 5-1: One-dimensional silver irregular belts synthesized without capping agent after 20 min; a) overall view of the product and close-up image of a belt; b) high magnification image of the surface of a belt; c) thickness of the belts; d) XRD pattern of the belts.

Figure 5-2-a shows one-dimensional silver particles and Figure 5-2-b provides a higher magnification image of them, which reveals their structure as serpentine belts. These belt shape silver particles were synthesized when PMAA was added to the system. Figure 5-2-c illustrates the thickness of the belts, measured as 25 nm. Hence, the particles are nanobelts. Figure 5-2-d shows an individual silver nanobelt which consists of hexagonal and triangular structural blocks; some of the triangles and hexagons are highlighted. The inset shows a triangular nanoplate that remained unattached in the system.

The role of PMAA in this synthesis can be established by comparing Figure 5-1 and Figure 5-2. Adding PMAA to the system reduced the thickness of the synthesized belts (Figure 5-c and Figure 5-2-c). In addition, since hexagonal and triangular structural blocks were synthesized in the presence of the PMAA (Figure 5-2-d), one can hypothesize that the PMAA molecules attach to the (111) planes of silver crystals and decrease the growth rate in a [111] direction; thus conforming to a well-established synthesis process of the nanoplates[19, 21, 121]. And then, the nanoplates self-assembled and joined to each other, side by side, to fabricate each nanobelt; a process that we have previously elucidated[122]. The hypothesized role for the PMAA can be investigated by examination of the crystal structure of the

nanobelts. Figure 5-3-a is a TEM image of a silver nanobelt. This image shows that the nanobelts consist of silver nanoplates. Selected area diffraction (SAD) pattern of the marked area of Figure 5-3-a revealed that the zone axis of all of the particles in the area of diffraction pattern is [111] (Figure 5-3-b). The area of diffraction pattern consists of several individual particles that joined to each other laterally. Since only one diffraction pattern was observed from all of them, it can be concluded that all of these particles oriented in the same direction and their flat basal planes were parallel. This is compatible with the aforementioned synthesis mechanism of nanobelts [122]. Figure 5-3-c shows the XRD pattern of the silver nanobelts, which confirmed that only the (111) crystallographic direction exists on the surface of the nanoparticles. This crystal texture is different from that of the microbelts (Figure 5-1-d). The TEM and XRD results revealed that the nanobelts formed by joining of hexagonal and triangular nanoplates. The structural blocks remained intact and only joined at their edges. Hence, flat surfaces of the nanobelts are (111) planes. This special structure of nanobelts provides evidence that PMAA can stabilize the (111) plane of fcc crystals. Therefore, adding of PMAA to the system causes a change in the product from microbelts to well oriented single crystal nanobelts.

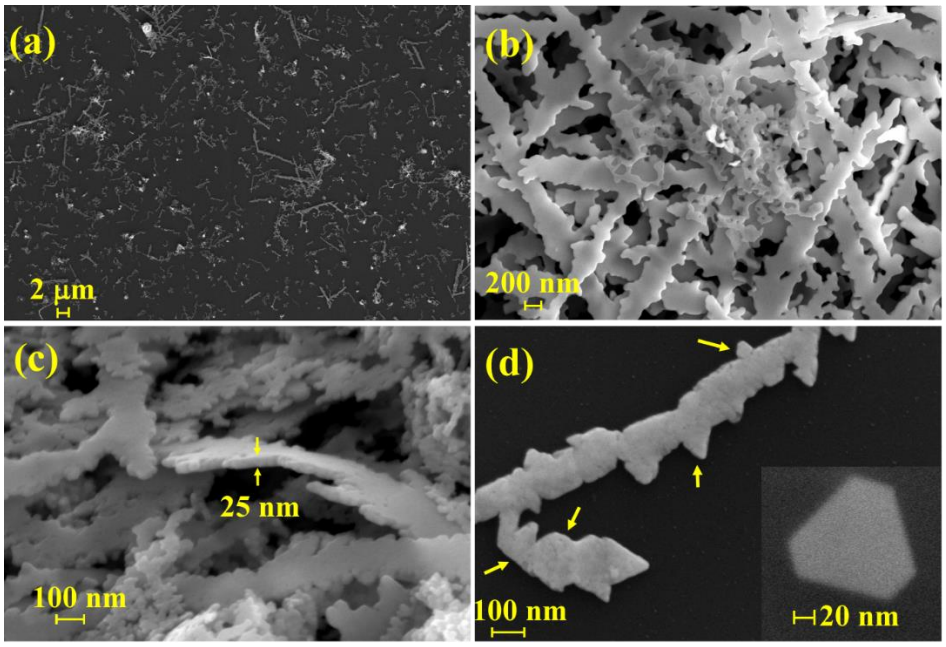

Figure 5-2: a) Synthesized silver nanobelts; b) High magnification image of the nanobelts ; c) Thickness of the nanobelts is around 25nm; d) Structure of a nanobelts, inset is one of the triangular blocks.

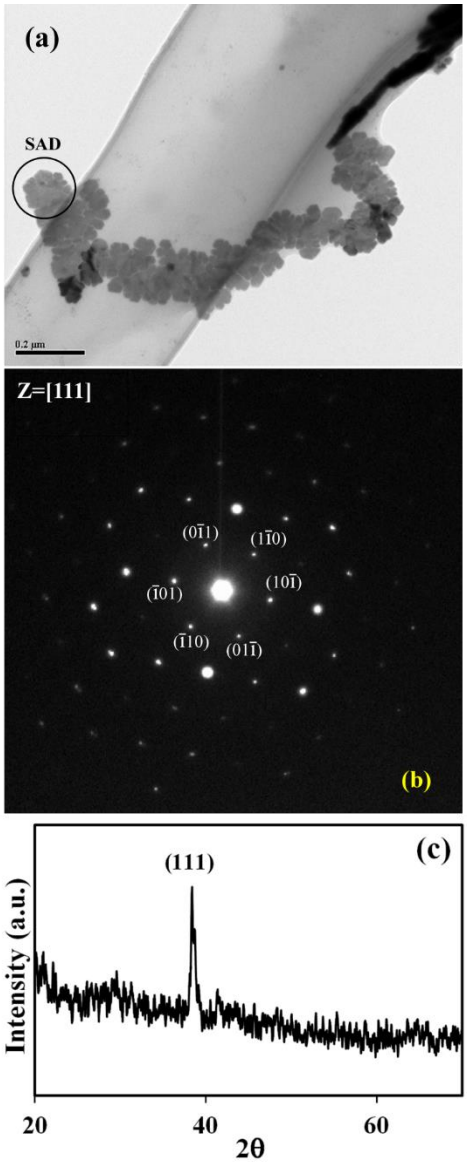

Figure 5-3: a) TEM image of a nanobelts; b) SAD pattern of the marked area; c) XRD pattern of the silver nanobelts.

5.2.2 Silver Nanoflakes

Aging of the silver nitrate solution resulted in a change in the morphology of one-dimensional silver nanobelts to two-dimensional silver nanoflakes. Figure 5-4 illustrates synthesized silver particles using the same recipe as that used for nanobelts, but after 48 hour ageing of silver nitrate solution. In this synthesis, the particles took on a flake shape instead of the belt shape (Figure 5-4-a). High magnification SEM examination revealed that the flakes formed by joining of hexagonal and triangular silver blocks;

some of the blocks were bigger than usual (Figure 5-4-b). Figure 5-4-c reveals that the thickness of the flakes was around 25 nm, almost same as that of the synthesized silver nanobelts (Figure 5-4-c). This shape change from one-dimensional nanobelt to two-dimensional nanoflakes that observed after aging of silver nitrate solution is clarified that preparation of silver nitrate solution has important impact in the assembly of silver structural blocks. The effect of preparation method of silver nitrate solution of the morphology of the product will discuss later in this chapter.

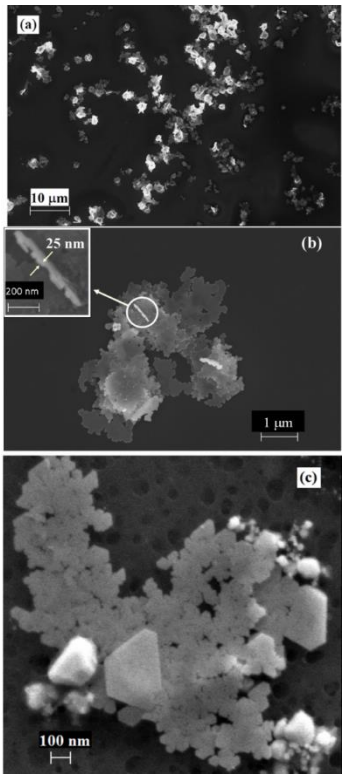

Figure 5-4: a) Overall view of the synthesized silver nanoflakes; b) higher magnification image of the silver nanoflakes; c) structural blocks of silver nanoflakes

5.2.3 Silver nanosheet

Figure 5-5 shows multilayer and single-layer silver nanosheets that were synthesized by the same recipe used for silver nanobelts. The only difference between this synthesis and the others was mixing of the solutions. In this experiment, the silver nitrate solution was added dropwise to reducing solution. This type of mixing resulted in floating very thin sheets of silver on top of the solution (Figure 5-5-a).

Figure 5-5-b and c demonstrate that these floated nanoparticles are multilayer or single-layer porous silver nanosheets, respectively. Insets of Figure 5-5-b and d reveal the structure of the nanosheets in higher magnification. XRD analysis of the nanosheets demonstrated the crystal structure of the sheet (Figure 5-5-d). This pattern confirmed that the crystal structure of the sheets is same as that of the silver nanobelts. By adding silver nitrate solution to the reducing solution, the reaction happens on the surface of the liquid and because of the special geometry of the particles, they will float on the suspension. Individually floated particles can join with each other to make large silver nanosheets, even up to several centimeters in diameter.

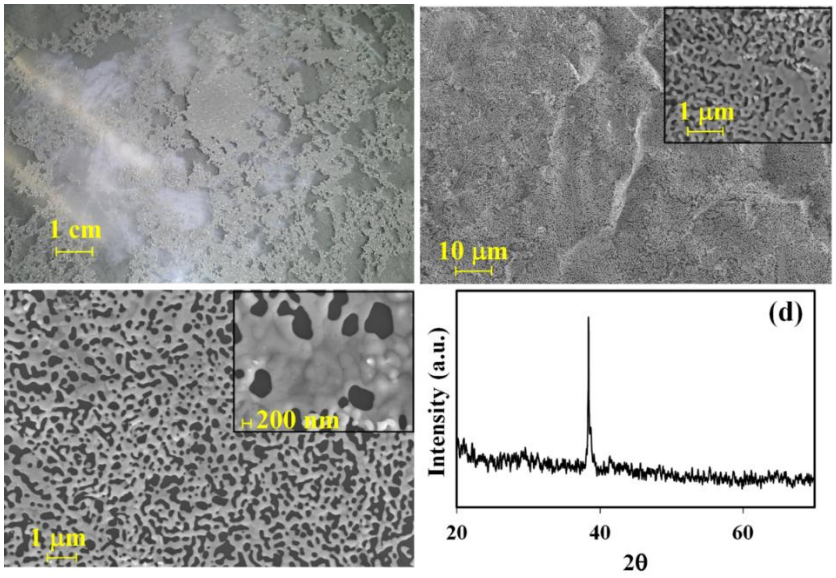

Figure 5-5: a) Optical image of the floated silver nanosheets; b) multilayer porous silver nanosheets, inset is a high magnification image of the nanosheet; c) single layer porous nanosheet, inset is a high magnification image of the nanosheet; d) XRD pattern of the silver nanosheets.

5.2.4 Synthesis mechanism and affecting parameters of one- and two-dimensional silver nanostructures by oriented attachment

To investigate the effect of $AgNO_3/C_6H_8O_6$ molar ratio on the shape of silver supercrystals, six different recipes were selected (Table 5-2). We performed five replicates of each recipe, both with and without the addition of balance water used to maintain constant final volume (4^{th} column of Table 5-2). The addition of water had minimal effect of the resulting nanoparticles, which otherwise exhibited repeatable morphologies specific to each recipe, providing ten replicates per recipe. Figure 5-6

demonstrates the synthesized nanostructures by these six recipes, Based on these observations, chemical reduction of silver ions at very low $AgNO_3/C_6H_8O_6$ molar ratio (0.05) leads to ball-like nanoparticles, which are actually disordered clusters of very small structural blocks (inset of Figure 5-6-a). Increasing the $AgNO_3/C_6H_8O_6$ ratio to 0.27 changes the supercrystals to flower-shape particles created by short and wavy ribbons-like structural blocks (inset of Figure 5-6-b). Molar ratios of 0.53 and 1.0 produced small porous nanosheets of silver (Figure 5-6-c and d). Inset image of Figure 5-6-d reveals the thickness of the sheets is about 25 nm. Finally, high $AgNO_3/C_6H_8O_6$ molar ratios (1.6 and 3.2) produced one-dimensional silver nanobelts (Figure 5-6-e and f).

Careful examination of the SEM images of Figure 5-6 reveals a clear trend in the synthesized nanoparticles. All recipes other than recipe 1 produced nanostructures composed of short nanobelt segments that have undergone a second stage of assembly. In recipes 2 through 6 we see a progression in preferred joining site. Recipe 2 displays extensive joining along all segment faces, producing flower-like clusters. Recipe 3 through 6 display joining that is highly selective to the narrow edges. This progresses from long-edge-to- long-edge "lateral" joining dominating (recipe 3), to tip-to-long-edge "branching" joining dominating (recipes 4 and 5), with tip-to-tip "linear" joining becoming more in the progression from Recipe 5 to 6. This is either due to an increasing preference towards linear joining, or an increasing aversion to long-edge joining. Recipe 1 appears to be consistent with this progression, representing clusters of particles that have joined indiscriminately. In our experiments, all recipes have same ascorbic acid and PMAA concentration. However, silver content of the recipes are different, although the silver nitrate solution (Solution A) that used in all recipes has same molarity. In addition, the pH of the solution is a function of the amount of ascorbic acid and silver nitrate that react with each other. Therefore, the effect of silver content of the reactor and PH evolution during progress of the reaction on the formation of the silver supercrystals must be uncovered.

Table 5-2: The recipes of the syntesis with different concentraion of silver ion.

Recipe Number	Solution A (ml)	Solution B (ml)	H2O (ml)	$\frac{AgNO_3}{C_6H_8O_6}$ (mol/mol)
1	1	200	59	0.05
2	5	200	55	0.27
3	10	200	50	0.53
4	20	200	40	1
5	30	200	30	1.6
6	60	200	0	3.2

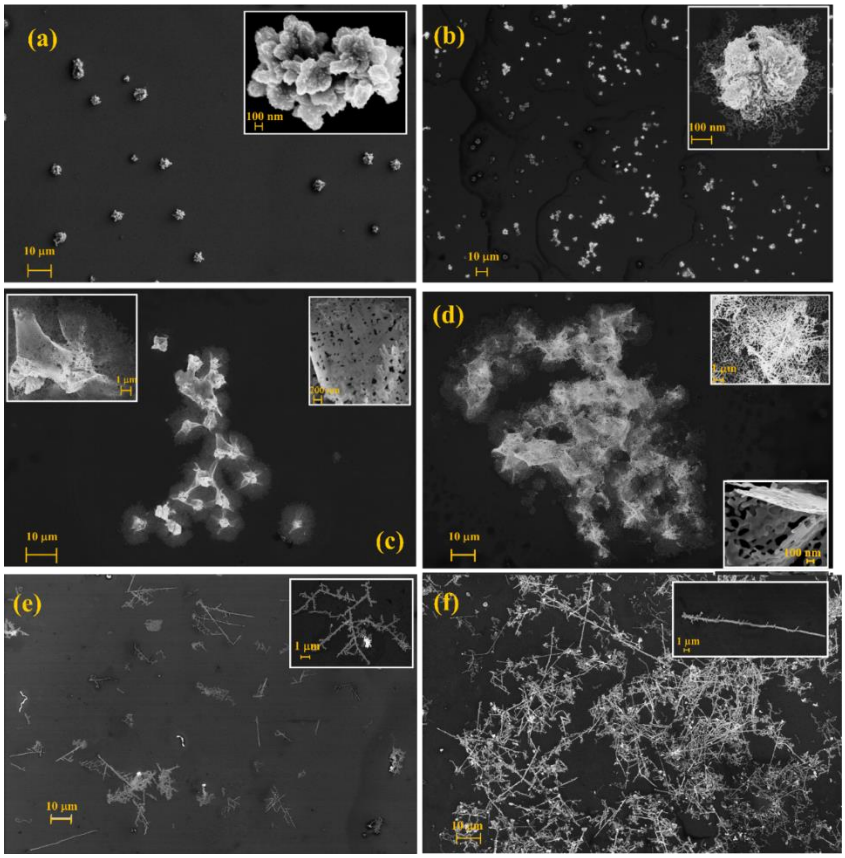

Figure 5-6: SEM images of the silver supercrystals synthesized by recipe 1 to 6 (a to f, respectively)

Evolution of the pH versus progress of the reduction reaction (Equation 1) for each recipe was calculated using the proposed model (Figure 5-7-a). Regarding fast progress of the chemical reaction, precise measurement of the pH during reaction was practically impossible due to time lag of the conventional pH meters. Hence, to examine the accuracy of the model, the pH of the reactor after completion of the reaction was measured for all recipes, which illustrates excellent agreement between the model prediction and experiment (Figure 5-7-b). Based on the presented data in Figure 5-7-a, the pH value of the recipe 1 shows very small change, which is predictable due to low silver content of the reactor. For other recipes, the PH evolution shows a descending trend and, increasing silver content of the recipes leads to higher rate of the PH reduction. To explain the difference between the recipes, we select PH 2 as a benchmark. Based on the Figure 5-7-a, the reaction of the recipe 1 to 3 finish at a PH higher than 2. In recipe 4, 70% of silver ions reduced at a PH higher than 2, while this value is 50% for recipe 5 and 40% for recipe 6. Hence, Not only the silver content of the reactor increased in the recipes,

but also more silver nanoparticles synthesize in lower PH when $AgNO_3/C_6H_8O_6$ molar ratio increases. This finding is very important because the role of PMAA molecules as capping agent might be pH dependent [77, 110]. In addition, changing the PH of the reactor is able to change the reactivity of ascorbic acid and hence, the kinetic of reduction reaction. Figure 5-7-c presents moles of silver converted per liter of reaction mixture for each recipe as a function of arbitrary time, demonstrating that the time to completion increases up to recipe 5, while recipe 6 displays a similar reaction duration as recipe 4. This is because the stoichiometric ratio of $AgNO_3$ to $C_6H_8O_6$ is 2:1, and recipe 4 and 6 lie equidistant to the crossover point. Figure 5-7-d presents the reaction rate of each recipe versus arbitrary time, demonstrating that the reaction rate increases monotonically with the increasing $AgNO_3/C_6H_8O_6$ molar ratio.

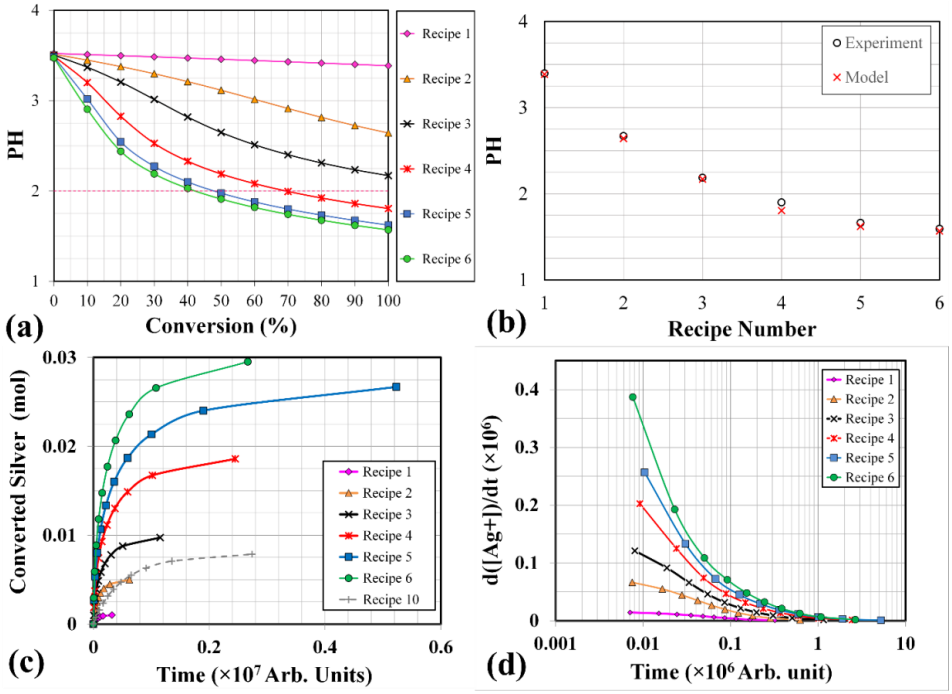

Figure 5-7: a) pH changes during progress of synthesis redox reaction for recipe 1 to 6; b) Comparison between predicted final pH of the recipe 1 to 6 and experiments; c) Calculated molarity of silver converted for recipe 1 to 6 and recipe 10 versus time; d) The reaction rate of recipe 1 to 6 versus time.

To distinguish between the effect of $AgNO_3$ to $C_6H_8O_6$ molar ration and PH on the morphology of the products, we manipulate the pH of recipe 6 by using NaOH and HNO_3 to the solution B, while the silver content of the solution was kept constant (Table 5-3). The PH value of reduction solution of recipe

7 was adjusted to be higher than PKa value of ascorbic acid and less than PKa value of PMAA, and for recipe 8 was adjusted to be higher than PKa value of both ascorbic acid and PMAA. a demonstrates the pH vs conversion of the chemical reaction of recipe 7, and 8 in comparison to recipe 6, which uncovers that the 90% of the reaction has done at a pH high than 2. Figure 5-8-b and c show the SEM images of the synthesized nanoparticle by recipe 7 and 8. These images illustrate that increasing pH of the solution at constant $AgNO_3/C_6H_8O_6$ molar ratio was tremendously changed the morphology of the products. The Product of recipe 7 is wavy silver nanobelts and individual overgrown hexagonal and triangular silver particles (Figure 5-8-b). Increasing the pH to 7.4 in recipe 8 eliminate assembly of the structural blocks and let them to growth as individual particles. Recipe 7 and 8 illustrate the upper margin of the pH, however in recipe 1 to 6 pH is less than 4 in all cases. Therefore, to clarify what happen if all silver ions reduce at a PH lower than 2, we modified recipe 3 by adding HNO_3 to adjust the pH of reducing solution to be 1.85. This also changed the concentration of nitrate ions to be between that of recipes 4 and 5. The pH versus conversion of the chemical reaction of recipe 9 is demonstrates Figure 5-8-a. The pH of this recipe is always bellow pH 2 while as demonstrated in Figure 5-7-d, required time to convert all silver ions in this case is much longer than recipe 3 and equal to recipe 6. This circumstance seem to be a good index to distinguish the effect of pH, silver content of the reactor and conversion time. Synthesized silver nanostructures by recipe 9 is demonstrated in Figure 5-8-d, which demonstrated that the synthesized particles are a combination of wavy and straight one-dimensional silver nanostructures. Based on this observation, the silver content of this recipe is almost same as recipe 3, the conversion time of this recipe is close to recipe 4, 6, and less than 5; however, the resultant silver nanostructure is more similar to recipe 5 and 6.

Table 5-3: Recipies of the synthesis with adjusting PH by using NaOH or HNO_3

Recipe Number	Solution A (ml)	Modified reducing solution		$\frac{AgNO_3}{C_6H_8O_6}$ (mol/mol)
		Solution B (ml)	Adjusted pH	
7	60	200	5.70	3.2
8	60	200	7.40	3.2
9	10	200	1.85	0.53

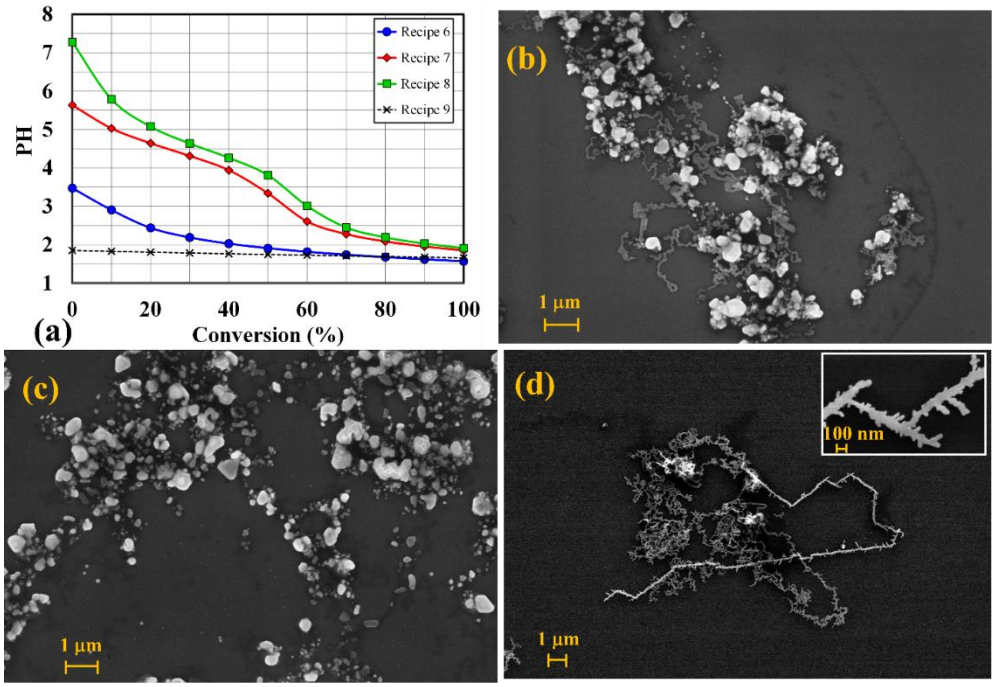

Figure 5-8: a) pH changes during synthesis of supercrystals by recipe 6 to 9; SEM image of the synthesized particles by pH manipulated in: b) Recipe 7; c) Recipe 8; d) Recipe 9.

We observed that the size of the silver nanobelts that synthesized by recipe 6 is very sensitive to preparation method of the silver nitrate solution. To investigate this phenomenon, we conduct two experiments. First, we used 5 minutes severe shaking to dissolve silver nitrate crystals and then, this solution was used for synthesis. Figure 5-9-a shows the synthesized sliver nanobelts after severe shaking of silver nitrate solution. Comparison between Figure 5-9-a and Figure 5-6-d clearly demonstrates that shaking of silver nitrate solution is able to reduce the length of the synthesized silver nanobelts. On the other hand, it is reported in the literature that dissolution of the silver nitrate is not a simple one-step process , but that the silver nitrate dissolves through some intermediate stages such as silver trimers (Ag_3^{3+} and Ag_3^{+}) and these silver trimers can be considered as nucleation site for nanoplates [123]. Therefore, it can be hypothesized that silver trimers play the role of precursor for silver hexagonal and triangular nanoplates, and that aggressive mixing decreases the number of silver precursors available in the reactor. To examine this idea, we designed the second precursor solution experiment, recipe 10, in which 2.1 gr $AgNO_3$ was slowly dissolved in 10 mL water by very gentle movement of the container to minimize mixing. To examine this idea, we designed recipe 10, in which 2.1 gr $AgNO_3$ was dissolved

in 10 ml water by very gently movement of the container. Concentration of this solution is 6 times higher than recipe 6. To keep total concentration of the system same as recipe 6, 50 ml water was added to the reactor simultaneously with reducing solution (Table 5-4). Figure 5-9-b demonstrates the synthesized silver nanobelts and inset of this image demonstrates the thickness of the nanobelts. The synthesized nanobelts by recipe 10are much longer than recipe 6. Figure 5-9-c shows one of the synthesized nanobelts, which is around 95 nm in length. The Insets of this image, demonstrate high-resolution image of two parts of this nanobelts, which confirm continuity of the nanobelt.

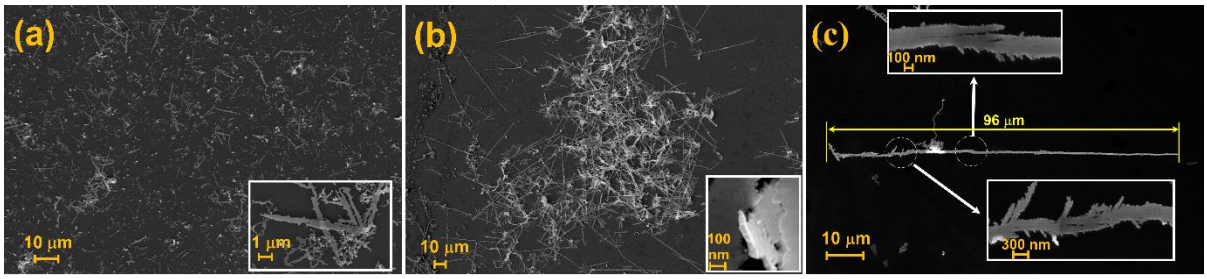

Figure 5-9: a) Short nanobelts, synthesized by recipe 6 by using agresivly shaked silver nitrate solution; b) Long nanobelts, synthesied by recipe 10; c) High magnification SEM image of a long belt-shape supercrystal synthesized by recipe 10.

Table 5-4: Recpie of the synthsis with high silver nitrate concentration

Recipe Number	Silver nitrate solution	Solution B (ml)	H2O (ml)	$\frac{AgNO_3}{C_6H_8O_6}$ (mol/mol)
10	2.1 gr $AgNO_3$+10 ml H2O	200	50	3.2

It is noted that the differing reaction rates among the recipes were not negligible and can be visibly differentiated by changing color of the solution from a clear solution to black. Therefore, we measured the transmittance of the solutions during synthesis. The results of these measurements for recipe 6, 8, and 10 are presented in Figure 5-10 . In addition, it was possible to record the changing pH of the solution during synthesis for recipe 10, due to its exceptionally slow reaction rate, and the results have been superimposed. Figure 5-10 demonstrates that the synthesis with recipe 8, in which the addition of NaOH raised the pH of the solution above the PKa value of the ascorbic acid and PMAA, displayed a reaction rate higher than recipe 6. More interestingly, recipe 10 has a very low reaction rate, even though the fully-mixed concentration, pH, and $AgNO_3$/L-ASB molar ratio of these two recipes were similar. The only difference between these two recipes was higher concentration of the precursor silver nitrate solution, and the preparation method of this solution.

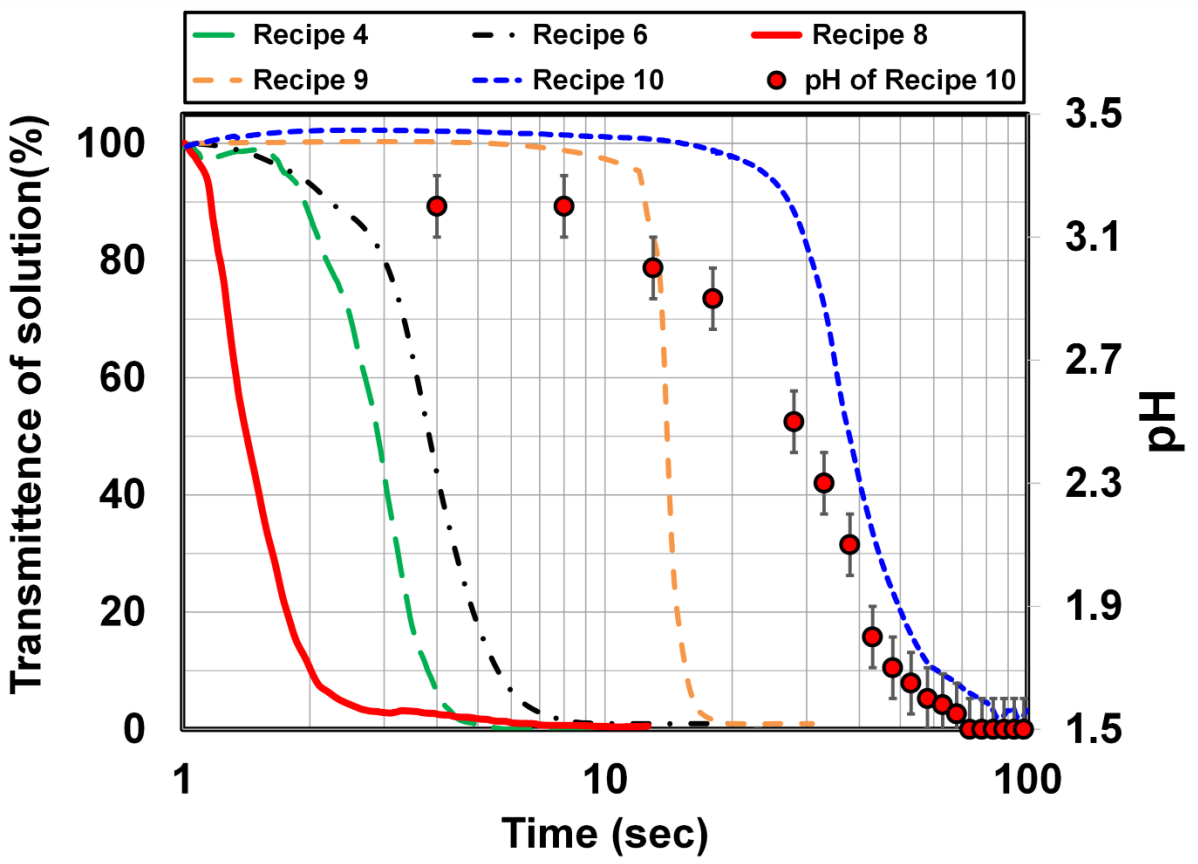

Figure 5-10: Kinetic of synthesis reaction measured by light-transmission for recipe 6, 8, and 10. Evolution of pH during synthesis by recipe 10 is superimposed on the graph. The presented pH data is the average of 6 replicates.

5.2.4.1 Discussion

Literature would argue that the type of nanoparticle growth and assembly observed here achieves varying morphologies through kinetically controlled processes [77, 124]. However, in this system the kinetics of the process was determined not to be the controlling factor. The reduction reaction appears to be the rate-limiting step, as evidenced by the agreement between light-transmission and pH data for recipe 10, and the general agreement between light-transmission and kinetic predictions for recipes 6 through 8. Based on morphology, recipes 6 and 10 were the most similar, and yet their

reduction kinetics differ by orders of magnitude. Meanwhile, recipe 4 had reduction degree of conversion kinetics most similar to recipe 6, while the two display significantly different morphology. Similarly, recipes 9 and 10 were both observed to significantly deviate from their predicted kinetics due to long incubation times. Although they displayed similar incubation times and reaction durations, recipe 9 and 10 produced significantly different final morphologies. This insensitivity to kinetics appears to be why the repeatable synthesis of these nanostructures can be completed so rapidly. A working hypothesis on why the morphologies display such insensitivity to kinetics is that they each represent a local equilibrium under their experimental conditions. Comparing the morphologies of recipes 1 through 6, 9, and 10, it can be seen that the progression in preference for lateral, branching, or linear joining correlates either with the final pH or with the concentration of nitrate ions. Based on our model, correlation with final pH may be due to the changing ionization of PMAA from 3% to 0.4% as the pH dropped from approximately 4 to 1.5. This is a relatively small change, and so this having such a significant effect would be surprising. A potential source of the pH sensitivity is the unreacted L-ascorbic acid, which changes ionization from 19% to 0.3% across this pH regime as predicted by model. However, for most recipes investigated the lowering pH throughout the reaction is caused by the consumption of the ascorbic acid, in some cases to completion (recipes 6, 10). Therefore, a reasonable hypothesis is that either the uncharged L-ascorbic acid, or the dehydroascorbic acid product of the reduction, may be involved in this process. We cannot rule out the correlation of the nitrate ion with the morphology; however, we do not have a hypothesis of the mechanism at this time.

It should be noted that Recipe 7 and 8 represent a different regime in the PMAA ionization. In recipe 7, where the high pH value produced initial PMAA ionization of 38% as predicted by our model, the majority of the silver is in the form of prismatic crystals that we hypothesize are overgrown primary structural blocks, accompanied by limited quantities of assembled nanostructures. In recipe 8, where the PMAA initial ionization was 85% (calculated by model), the assembled nanostructures are absent. Therefore, highly ionized PMAA may be inhibiting assembly, due to charge repulsion.

There is an indication that the silver ion concentration may affect the length of the short nanobelt segments prior to their final assembly, based on comparison within Figure 5-6. If this is the case, we hypothesize the trend would be related to the increasing concentration of primary silver nanoplates. However, silver content is partially correlated with the trend in linear joining, complicating analysis. Recipe 10 displays exceptionally long linear nanobelts, at the same silver concentration as recipe 6, and differs only in the AgNO3 dissolving procedure. The long reaction time of recipe 10 may

indicate a change in the nucleation characteristics caused by this gentle mixing, which may indicate a change in the number-concentration of the primary silver nanoplates.

5.3 Summary

In this research, one-dimensional silver nanobelts, two-dimensional silver nanoflakes and multilayer and single-layer porous silver nanosheets were synthesized by choosing suitable solution parameters. From the crystal structure point of view, these silver nanoparticles are unique because of the special surface texture of the products. The surfaces of the nanobelts, nanoflakes and nanosheets are (111) crystallographic planes. This special crystal structure of the products was confirmed by TEM and XRD observations.

Repeatable and fast synthesis of one- and two- dimensional silver nanostructures, constructed from highly stable hexagonal and triangular nanoplates. We demonstrated that the primary nanoplate structural blocks will assemble into secondary 1-dimensional belt-shaped segments, followed by secondary assembly and joining into various larger scale structures. The selectivity of preferred joint locations during this secondary assembly directed the development of the final morphology. We demonstrated that these are not kinetically controlled processes, and that the selectivity of joining location during secondary assembly correlated with pH and the concentration of nitrate ions in solution. There were some indications that the concentration of silver ions correlated with the developed length of the secondary belt segments, however this was correlated with the factors that also selected for more linear secondary assembly modes, complicating analysis.

Chapter 6
High temperature stability, surface disordering and melting of silver nanoparticles

In this chapter, first, thermal stability of silver nanobelts is compared to pentagonal silver nanowires by Molecular dynamics simulation and experimental observations. Then, surface disordering and melting of silver nanoparticles are discussed.

6.1 How morphology and surface crystal texture affect thermal stability of a metallic nanoparticle: the case of silver nanobelt and pentagonal silver nanowire

The thermal stability of crystalline metallic nanoparticles is a challenging topic in nanoscience, which can limit the employment of a nanoparticle at high temperature [125-132]. This is a complicated issue, since processes of chemical attack, diffusion, and phase change are all temperature dependent, and so it is often difficult to identify which are the dominant causes of thermal instability in a particular case. It has been shown that for metallic nanoparticles smaller than 2 nm the surface atoms play a critical role [125]. In this regime, most of the atoms are at the surface, and the arrangement of the atoms influences the stability of the particles independent of other factors. Researchers have employed protective layers to manipulate the surface atoms and enhance the stability of the nanoparticles within this size regime [125, 126]. At larger particle size regimes between 2 nm and 100 nm, the internal bulk of the particle becomes sufficient to produce a transition between the surface and core atoms. In this size regime, systematic investigation of thermal stability of metallic nanoparticles has been limited, though nanoparticles of this size are employed in many applications. In this size regime, research typically investigates the contribution of surface texture to stability in terms of how easily the nanoparticle surface is chemically attacked by outside contaminates. However, there remains an open question as to whether crystallography and surface texture act independently on the thermal stability of these metallic nanoparticles. In other words, before referring to the effect of external reactants, it is worthwhile to answer whether a nanoparticle is thermodynamically stable at high temperature or exhibit sufficient kinetic barriers to resist changing to a more stable form.

Of the metallic nanoparticles, silver is a desirable nanomaterial thanks to its remarkable physical and chemical properties. Researchers are developing silver nanoparticles for many unique applications [6, 30-35, 133-137], synthesizing them in a variety of sizes and morphologies during last two decades [19, 38, 41, 46]. Among those reported, pentagonal silver nanowire is unique: a high aspect-ratio particle, achieving excellent electrical conductivity and mechanical strength [40, 138]. These desirable properties have led to many previous works where silver nanowires were employed for various applications such as flexible and transparent electronics, nanosensors, transparent heaters, and nanocomposites [139-143]. However, it has reported these silver nanowires are not stable when subjected to high temperatures [18, 130, 139, 144] This has been attributed to sulfidation of silver nanowires, based on energy dispersive spectroscopy analysis [18, 145, 146]. Sulfidation of silver is a well-known process that can happen at room temperature and is intensified at elevated temperatures. Therefore sulfidation can be one of the driving forces of degradation of silver nanowires, under an appropriate environment. However, it is not clear how temperatures alone contribute to this instability, which could be investigated by annealing under vacuum or in an inert atmosphere. This is of concern because this instability may also be driven by the physical properties of nanoparticles such as surface crystallography. Such an effect would confound research efforts to mitigate the thermal instability of silver nanoparticles intended for high temperature applications; techniques that prevent chemical attack would be undermined or obscured by any intrinsic thermodynamic instabilities that exist for that particle crystallography.

It is well known that different crystal planes have different packing densities; more packing means lower energy and higher stability. In the case of silver, the close-packed (111) plane is the lowest energy crystal plane with maximum packing, and therefore the most stable. By comparison, the (100) plane is more loosely packed, higher energy, and therefore relatively unstable. However, no work has been reported to utilize theoretical calculation or experimental observation to investigate the surface morphology effects on thermal instability for nanoparticles such as nanowire. Silver nanowires have a pentagonal cross-section when viewed perpendicular to their major axis, with each edge corresponding to a (100) surface that runs parallel to the major axis. The pointed tips of the nanowires, which project in the direction of the major axis, are five-sided pyramids where each triangular face is a (111) surface. It means this crystal morphology, which mainly covered by the five high-energy 100 planes is not the most stable possible configuration for a silver nanoparticle in theory.

Recently we synthesized a new one-dimensional flat silver nanoparticle, the nanobelt [122], by simultaneous self-assembly and nanojoining of hexagonal and triangular silver nanoplates as structural

blocks. The nanoplates have been previously investigated [39, 99, 147, 148] and their crystal structure, explored by Elechiguerra et al. [34], were found to have a twin plane at the center and two (111) planes on the flat surfaces [19]. The majority of the nanobelt surface area is composed of closed packed (111) planes, as a result of realignment of the nanoplates during joining [122]. Therefore, it could be expected that silver nanobelts should be stable at higher temperature than pentagonal silver nanowire.

In this research, we demonstrate how the morphology and surface texture of a nanoparticles can affect its thermodynamic instability and how this inherent instability is temperature dependent. This question is answered by comparing the thermal stability behavior of two closely-related metallic nanoparticles, which differ mainly in surface crystal texture: silver nanowires and silver nanobelts. To do this research, we employed MD simulation and experimental observation to compare the thermal stability of these nanoparticles. Moreover, this study clarified the thermal stability of silver nanowires and nanobelts, which indicated nanobelts are a new candidate for high temperature applications, such as a transparent heater material.

6.1.1 Simulation and experimental methods

6.1.1.1 Simulation

Using the molecular dynamic simulation, for each atom, the potential energy is calculated by summing the bonding energy between that atom and its neighbors, and the total potential energy of the system was the sum of the potential energy of all atoms. Similarly, for each atom, the kinetic energy calculated according to the velocity of that atom, and the total kinetic energy of the system was the sum of the kinetic energy of all atoms. The displacement of each atom is calculated as the distance from its original position. To investigate the position of the atoms in the nanoparticle, the Ackland-Jones parameter was used to categorize the atoms based on their local crystal structure, setting a characteristic value for each atom [149]. In this MD simulation program, fcc structure was denoted by 2, hcp structure by 3 and unknown structure, such as a surface, by 1.

The simulated nanowire contained 3530 atoms, with the initial state designed according to crystal structure of nanowires [19]. To show the effect of nanowire size on thermal stability, we did simulation by a nanowire contained 6355 atoms. The diameter of this wire was 6.2 nm, which was approximately two times larger than the first nanowire. The simulated nanobelt segment contained 4804 atoms, and was composed of three joined sub-units: two hexagonal nanoplates and one triangular nanoplate. To represent a real silver nanobelt accurately, the simulated nanobelt segment was constructed by initially placing the simulated nanoplates in a MD simulation domain at 300K, with the distance between the

nanoplates less than cut-off radius of the MD program. Under these conditions, the surface atoms of the particles attracted each other, and the nanoplates joined to produce the model nanobelt segment. This joining mechanism was investigated by the author, and reported in our previous paper [122]. Using these simulated structures, thermal stability was studied by simulating the MD simulations at various desired temperatures, for 10^6 time-steps in all cases.

6.1.1.2 Experimental Procedure

The silver nanowires were prepared in a polyol solution with polyvinylpyrrolidone (PVP) as a structure-directing reagent, using a method modified from the literature [73, 141, 150, 151]. In this study, 330 mg PVP ($(C_6H_9NO)_n$, K25, M.W.= 24000, Alfa Aesar) and 12.5 mg silver chloride (AgCl, Alfa Aesar) were mixed with 40 ml ethylene glycol (EG, Fisher Chemical) in a round-bottom flask to make solution A. This solution was heated to a temperature between 160°C and 170°C. Then, 110 mg silver nitrate was dissolved in 10 ml ethylene glycol liquid to form solution B. This solution added into the solution A while stirring vigorously and continuing the reaction conditions for 4 hours. Silver nanowires were washed with deionized (DI) water to remove the residual ethylene glycol and PVP.

To synthesize silver nanobelt, 2.1 g of silver nitrate ($AgNO_3$, Sigma-Aldrich) was added to 60 ml H_2O and agitated by ultrasonic bath for one minute to form $AgNO_3$ solution. Reducing solution was prepared separately by adding 0.68 g Ascorbic acid (Alfa Aesar) and 0.16 ml Poly (methacrylic acid, sodium salt) 40% in water (PMAA) solution (Aldrich Chemistry) as structure-directing reagent to 200 ml H_2O and agitated by ultrasonic bath for one minute. Synthesis was performed by mixing these solutions while the mixture was stirred by a magnetic stirrer.

6.1.1.3 SEM, TEM and XRD characterization

SEM and TEM were utilized to investigate the morphology and crystallography of both nanoparticles and EDX was employed to analyze the chemical composition of the products. To prepare SEM, EDX and TEM samples, 0.5 ml of the suspension containing nanowires or nanobelts was added to 3 ml H_2O, then agitated by ultrasonic bath for 5 min. For SEM samples, 0.02 ml was deposited by pipette onto a clean silicon wafer, then dried under argon at 70°C using a controlled atmosphere tube furnace. Immediately after drying, the samples was annealed at the proper temperature at same furnace under argon atmosphere. After annealing, the annealed samples were placed in a vacuum desiccator. For TEM samples, approximately 100µl of the diluted suspension was deposited onto a TEM grid, then dried under room conditions.

XRD was utilized to characterize the crystal structure of the newly developed silver nanobelts. To prepare XRD samples without annealing, suspended nanobelts were collected on filter paper (Whatman® # 1001042) by vacuum filtration to form a 1.2mm thick film. This was dried at 70°C in the air, then detached by peeling away the filter paper. To prepare all annealed XRD samples, 500 mg of silver nanobelts was dispersed in 10 cc water by ultrasonic agitation. This suspension was deposited onto an iron sheet (15cm×2.5cm) drop-wise and dried under argon at 60˚C using a controlled atmosphere tube furnace, then annealed. After annealing, the nanobelts were dispersed again in water using ultrasonic agitation, and then collected on filter paper (Whatman® # 1001042) by vacuum filtration. This was dried at under argon 70°C using a controlled atmosphere tube furnace, then detached by peeling away the filter paper. XRD was performed using an x-ray tube with wavelength output of Cu-K_α (λ = 0.154056 nm).

6.1.2 Results and discussion

6.1.2.1 MD Simulation of Silver Nanowire

The results of four MD simulations of a short silver nanowire being annealed at four different temperatures (-272˚C, 200˚C, 300˚C, and 400˚C) are presented in Figure 6-1. It is apparent that the nanowire is thermally unstable above 200˚C, with degradation worsening as temperature increases. The -272˚C simulation (Figure 6-1-a) reveals the nanowire to be stable and well ordered, having developed no apparent defects; the (100) plane of the nanowire side is highlighted in the inset view. At 200˚C (Figure 6-1-b) and above (Figure 6-1-c to d), atoms (arrows 1, 3, 6 and 7) migrate from their initial positions onto (100) surfaces to form clusters (arrows 3, 6 and 7), leaving vacancies at the edges where the (100) surfaces intersect (arrows 2, 4 and 5). In the 400˚C simulation (Figure 6-1-d), a great deal of degradation has occurred; large clusters of migrated atoms have formed, and the edges at the intersection of the (100) surfaces have eroded. These eroded edges leave behind a new surface crystallography: the hexagonal close-packed (111) crystal plane, outlined by the white rectangle in (Figure 6-1-d) and shown magnified in the inset. Interestingly, the tips of the nanowire were stable at each of these simulated temperatures, and are composed exclusively of (111) crystal planes. An additional simulation of a larger diameter nanowire at 400˚C for 2×10^6 time-steps is also included (Figure 6-1-e), and confirms that the larger nanowire degrades in the same way as the smaller one. The longer simulation time in this case reveals that the degradation is not limited to a single atomic layer at

the sharp edge: the nanowire will continue to degrade, eroding (100) surfaces while producing surface clusters and new (111) planes.

These qualitative observations imply that the thermal instability of silver nanowires is primarily a result of surface atoms diffusing from the edges of high-energy (100) planes to form new surfaces. The production of (111) surfaces, and the lack of observed degradation of the nanowire tips, supports that the (111) surfaces are significantly more stable than the (100) planes. Figure 6-1-f presents the potential energy of the nanowire as the 400˚C simulation progressed; as anticipated, there is a reduction of potential energy as the nanowire degrades.

Figure 6-2 is an analysis of the potential energy, kinetic energy, and displacement of atoms for a simulated nanowire at 200˚C. This data is gathered from the beginning of the simulation, using the atomic states at five equally spaced time steps between 10000 and 11000. The nanowire tips are stable at all temperatures, and so it is reasonable to remove them from the following analysis. Coordinates were assigned by projecting the initial position of each atom onto an X-Y plane perpendicular to the major axis of the central nanowire segment. Figure 6-2-a shows atoms plotted by the A-J parameter versus initial X-Y coordinate; surface, interior, and twin boundary atoms are clearly distinguished. The remaining properties of Figure 6-2 are plotted with respect to radial distance (R) from the central Z-axis, calculated by equation 3.

$$R = \sqrt{X^2 + Y^2} \qquad (3)$$

Where, X and Y are the instantaneous coordinates of the atoms projected onto the X-Y plane. To highlight that simulated atom states are not being over-constrained, Figure 6-2 b-d displays the state of every atom for each distance R, rather than presenting average values. Figure 6-2-b demonstrates that interior and twin boundary atoms have similar potential energy, while the surface atoms have notably higher energy, implying that the instability is likely not the result of the twin boundary presence. The highest potential energies belong to the surface atoms farthest from the center axis, and therefore located close to the edges that describe the intersections of the (100) surfaces. Figure 6-2-c presents the kinetic energy with respect to radial distance, demonstrating that the simulation was appropriately isothermal. Plotting atom displacement in a similar manner (Figure 6-2-d), we see that the highest mobility was displayed by members of the edge-occupying group of surface atoms.

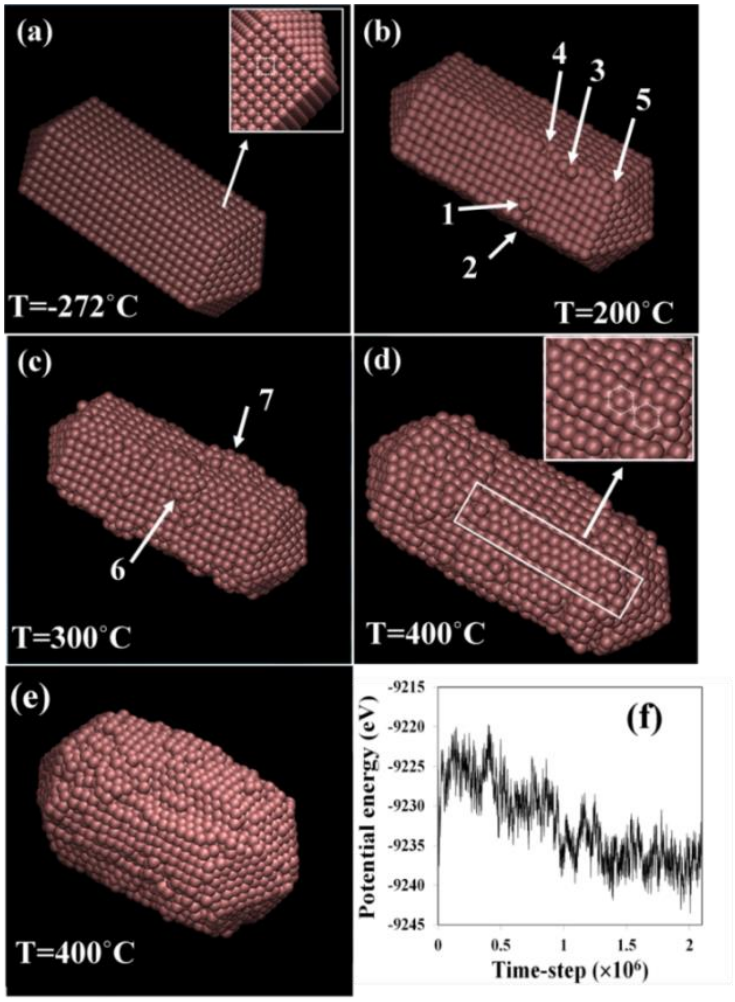

Figure 6-1: a) Structure of silver nanowires annealed at -272 ˚C; b) Silver nanowire annealed at 200˚C; c) Silver nanowire annealed at 300˚C; d) Silver nanowire annealed at 400˚C; e) A larger silver nanowire annealed at 400˚C for 2×10^6 time-steps, twice as long as the previous cases; f) Potential energy change of silver nanowire during annealing at 400˚C.

To explain how temperature can affect degradation, the potential energy of surface and interior atoms after annealing at 200˚C, 300˚C and 400˚C were compared (Figure 6-3-a). The average potential energy of surface is around 13% lower than the interior at these temperatures in all cases. However, considerable differences can be observed in the maximum potential energy of surface atoms. In other words, the maximum potential energy of a small fraction of the atoms is very high, which may allow them to escape from their original position. Based on this data, the mechanism of the instability of surface atoms can be explained considering Figure 6-3-b though d. Figure 6-3-b shows the kinetic

energy and vibration of the surface atoms in their potential well. The arrows in this figure show fluctuation of the kinetic energy. MD simulation data reveal that the interior atoms are stable and their vibration is not enough to let the atoms escape from the potential well. The potential energy of surface atoms is around 13% higher than the interior atoms (Figure 6-3-b). When the temperature is lower than 200˚C, the atoms of the corners remain in the potential energy well (Figure 6-3-c). However, increasing temperature to 200˚C or more will provide enough kinetic energy for some of the atoms to escape from their potential well (Figure 6-3-d). Obviously, few atoms with high kinetic energy have this chance to move out of their position. When an atom moves out from its position, the potential energy of the atoms around its vacancy increases, they will be more susceptible to escape from their original position, and this process can continue.

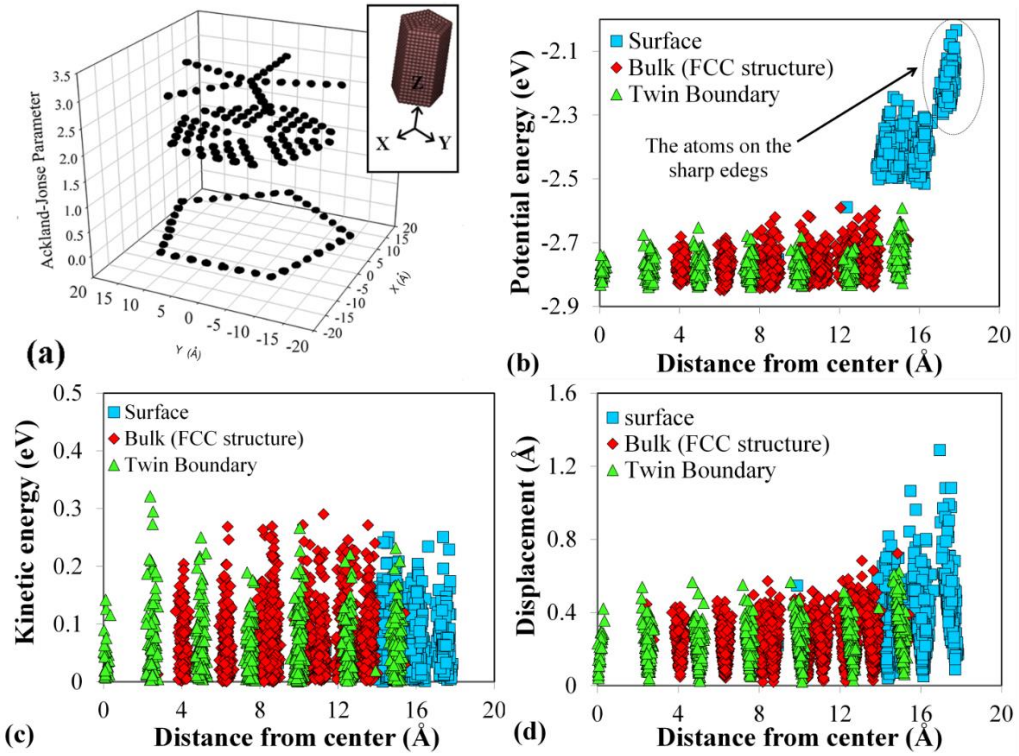

Figure 6-2: a) The Ackland-Jones parameter of the atoms of the silver nanowire versus x and y dimension of the atoms; b) Potential energy of the atoms versus distance from center of cross section (*R*); c) Kinetic energy of the atoms versus distance from center of cross section (*R*); d) Displacement of atoms versus distance from center of cross section (*R*).

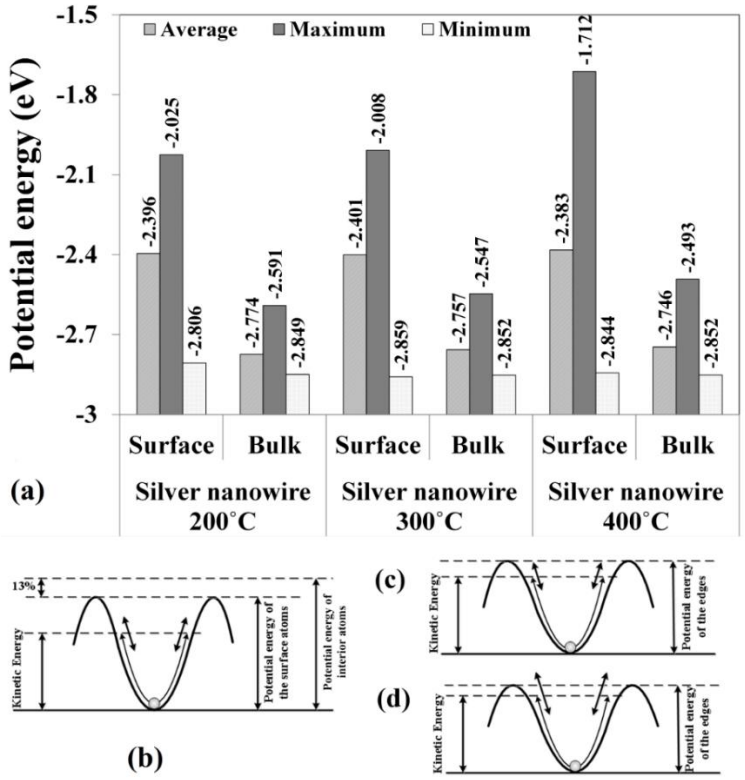

Figure 6-3: a) Average, maximum and minimum potential energy of the surface and interior atoms at 200˚C, 300˚C and 400˚C; b) Schematic grapH shows the kinetic energy and vibration of a surface atom compare to its potential energy; c) Schematic grapH shows the kinetic energy and vibration of an edge atom compared to potential energy at low temperature; d) Schematic grapH shows the kinetic energy and vibration of an edge atom compared to potential energy at high temperature.

6.1.2.2 Experimental Annealing of Silver Nanowire

The thermal stability of silver nanowires was examined experimentally though SEM and EDX of the annealed samples under argon atmosphere at 200˚C and 300˚C. Before annealing, Figure 6-4-a shows silver nanowires featuring sharp edges and well-defined morphology. Similarly, silver nanowires annealed for 10 hours at 200˚C are found largely stable, having maintained their gross morphology, as shown in Figure 6-4-b. However, after annealing for 10 hours at 300 ˚C (Figure 6-4-c) the nanowires were clearly unstable, having degraded by eroding in some areas while growing new surface features in others; this degradation is easily visible at high-magnification (Figure 6-4-d). The degradation is not electrochemical in nature; inset is EDX spectra of the indicated area, confirming that no contaminants were present, including sulfur. This contradicts the current literature findings that the sulfidation of

silver nanowires is the cause of their thermal instability, and instead reveals that silver nanowires are inherently unstable at high temperature.

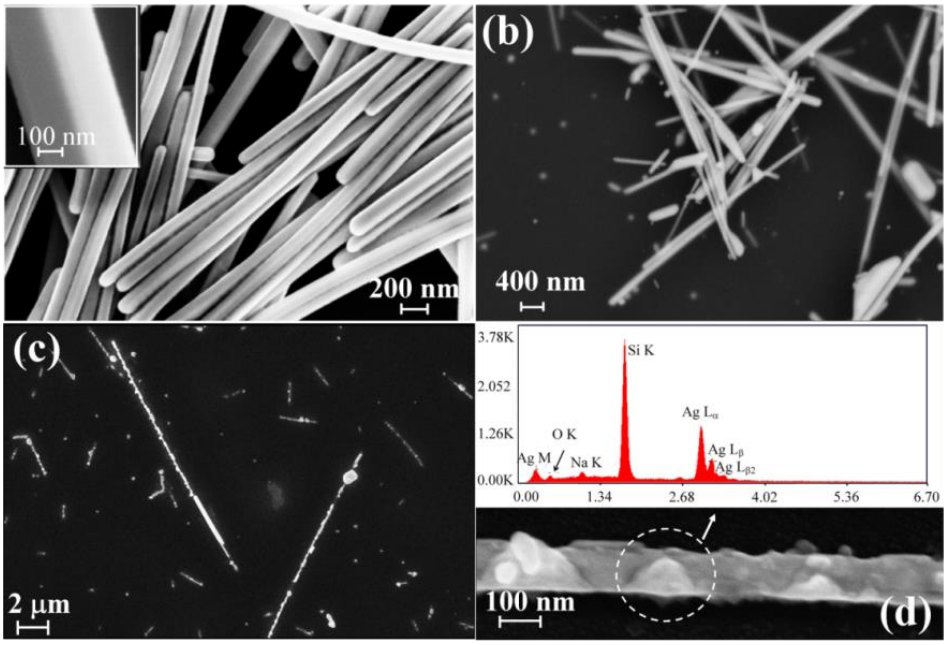

Figure 6-4: a) Synthesized silver nanowires; b) Silver nanowires after annealing at 200˚C for 100 hours; c) silver nanowires after annealing at 300˚C for 10 hours; d) High magnification image of a silver nanowire after 10 hours annealing at 300˚C, inset: the EDX analysis of the highlighted area.

For silver nanowire, the MD simulations and experimental observations indicate inherent thermal instability above 200°C, which makes them unsuitable for high temperature applications. The results imply that the greatest factor in this is the high potential energy of the nanowire surfaces, due to the majority of them being (100) crystallography. In comparison, the (111) planes of the surfaces at the tips of the nanowires appeared stable in the MD simulations, owing to their low-energy close-packed state. If this analysis of silver nanowires is correct, it follows that the primary feature of a silver nanoparticle with higher thermal stability would be a majority of surfaces composed of more stable (111) planes

6.1.2.3 MD Simulation of Silver Nanobelt

Recently, we have synthesized silver nanobelts, a new high-aspect ratio silver nanoparticle featuring (111) crystallography on its broadest flat surfaces. These nanobelts are produced easily through the

nanojoining of hexagonal and triangular structural blocks [122]. If the nanobelts found to be more thermally stable than silver nanowires, they would not only support the hypothesis of the cause of nanowire degradation, they would also provide a feasible alternative to silver nanowires for high temperature applications.

Six MD simulations of a short segment of silver nanobelt annealed at a different temperatures (-272˚C, 200˚C, 300˚C, 400˚C, 500˚C, and 600˚C) are presented in Figure 6-5. The final states of these simulations demonstrate that the nanobelt is thermally stable in temperatures up to and including 500˚C (Figure 6-5-a to e). The -272˚C simulation (Figure 6-5-a) reveals the nanobelt to be well ordered, having developed no apparent defects. From 200˚C and above, the nanobelt sub-units undergo a small relative rotation at their junctions (arrow 1) to minimize internal stresses. From 300˚C to 500˚C (Figure 6-5-c, d and e) the nanobelt develops sparse surface vacancies along its edges. Instead of forming random surface clusters like those on the nanowires, the migrated atoms relocate to the seams between the sub-units (arrow 2), filling the joints between the nanobelt sub-units and improving continuity of the (111) surface. As high as 400˚C and 500˚C (Figure 6-5-d, e) the simulations demonstrate that the broad (111) surfaces of the nanobelt are still intact. However, the minor restructuring of the sharp edges has occurred (arrow 3). In the 600˚C simulation (Figure 6-5-f) does the nanobelt display thermal instability, with atoms migrating from the edges to form clusters on the flat (111) surfaces (arrow 4). At this temperature, it is expected that atoms would continue to migrate across the surface until the nanobelt morphology completely degraded.

Numerical analysis of these MD simulation results (Figure 6-6), evaluates the potential energy, kinetic energy, and displacement of atoms in the 200˚C simulation, using the long-axis of the simulated nanobelt segment as the X-axis. Similar to the previous analysis, this data was gathered from the beginning of the simulation using the atomic states at five equally spaced time steps between 10000 and 11000, and the surface and interior atoms were differentiated using the Ackland-Jones parameter. Interestingly, Figure 6-6-a shows the surface atoms are divided into two distinct energy bands across the entire nanobelt length. A color-coded 3D model of the nanobelt (Figure 6-6-b), with each atom colored according to its potential energy, confirms that the broad and flat (111) surfaces of the nanobelt have lower energy than the edges, and that the high-energy atoms are a small fraction of the total nanoparticle. Some of the small faces are high-energy, as seen on the visible side of the triangular sub-unit; close inspection reveals these are composed of the minority (100) surface crystallography. A comparison between the nanobelt and nanowire (Figure 6-6 and 2, respectively) demonstrates that even at the edges of the nanobelt, the potential energy of surface atoms is smaller than nanowire. The only

exceptions to this are few atoms at the sharp vertexes of the nanobelt, which Figure 6-5 showed were not sufficient to produce thermal instability. The kinetic energy of surface and interior atoms have no significant difference (Figure 6-6-c), while surface atoms at the boundary and the corners are high mobility atoms based on the displacement of atoms(Figure 6-6-d).

The initial potential energies of atoms in the 500˚C and 600˚C simulations are plotted in Figure 6-6-e and f. As expected, the 500˚C simulation (Figure 6-6-e) has a pattern of potential energies approximately similar to that of the 200˚C (Figure 6-6-a). The lower surface energy band at 500˚C displays nearly the same as 200˚C. However, the band corresponding to the higher-energy edge atoms shows more high-energy atoms. In contrast, the 600˚C simulation (Figure 6-6-f) reveals that the surface atoms occupy a diffuse distribution, and representing the onset of thermal instability of silver nanobelts in the vicinity of 600˚C.

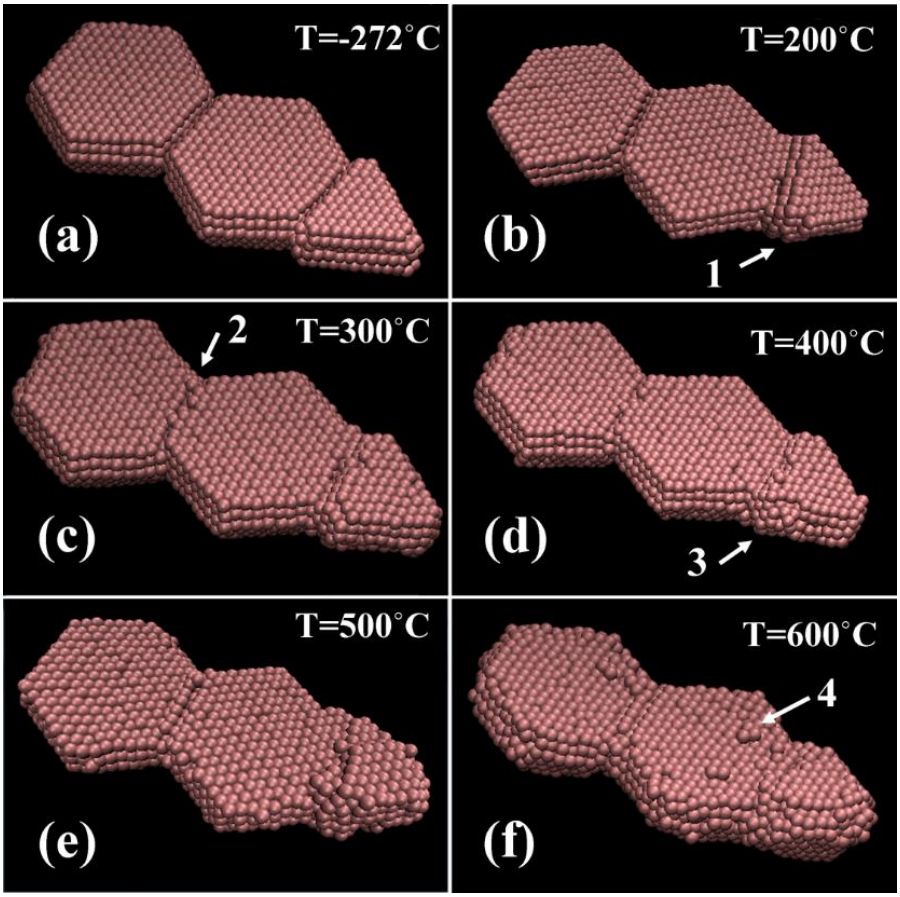

Figure 6-5: a) Structure of silver nanobelt annealed at -272 ˚C; b) Silver nanobelt annealed at 200˚C; c) Silver nanobelt annealed at 300˚C; d) Silver nanobelt annealed at 400˚C; e) Silver nanobelt annealed at 500˚C; f) Silver nanobelt annealed at 600˚C.

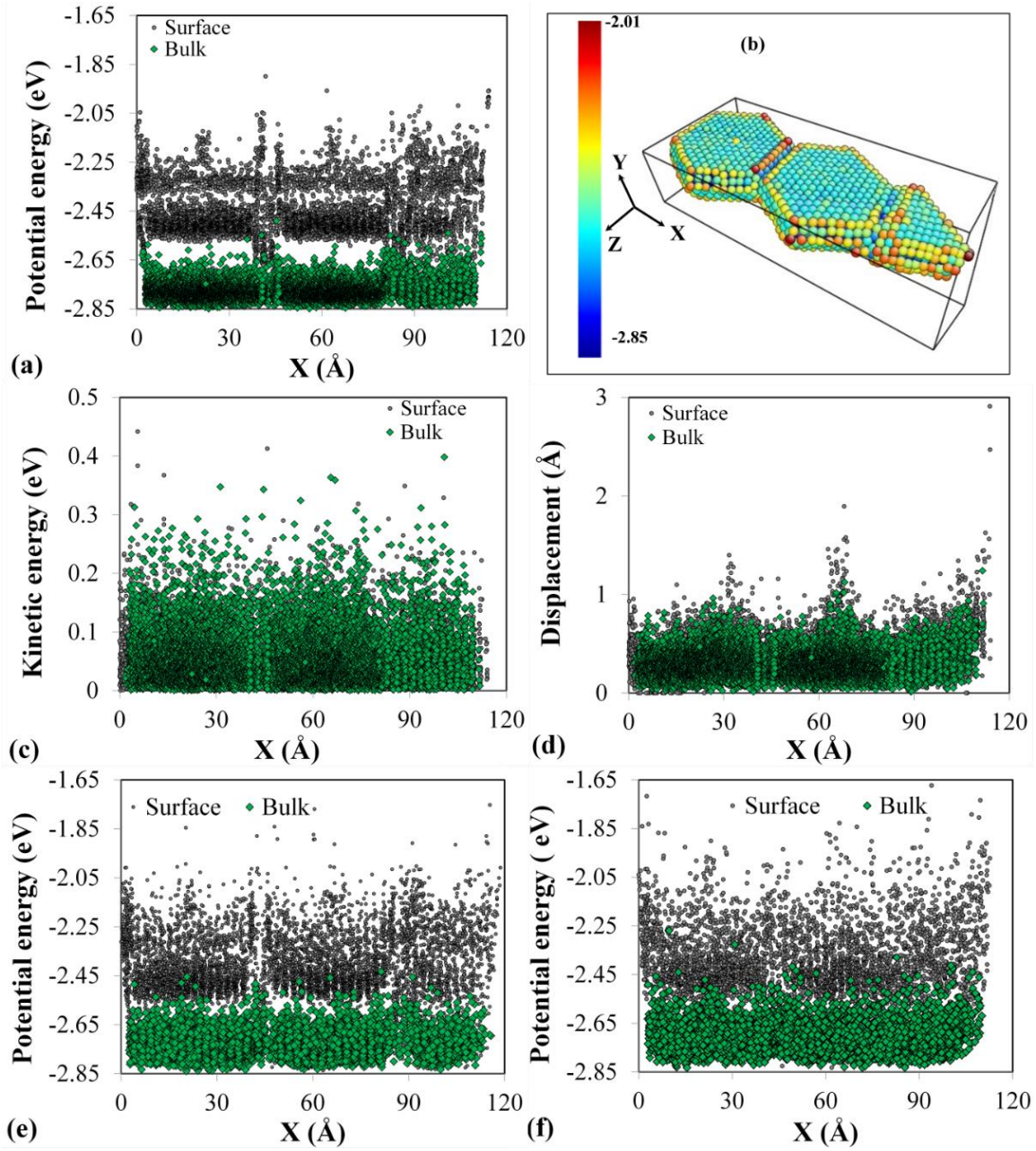

Figure 6-6: a) Potential energy of atoms at 200˚C versus position of atom on the X axis; b) Silver nanobelt, the color of atoms shows their potential energy; c) Kinetic energy of atoms at 200˚C versus position of atom on the X axis; d) Displacement of atoms at 200˚C; e) Potential energy of atoms at 500˚C; f) Potential energy of atoms at 600˚C.

6.1.2.4 Experimental Annealing of Silver Nanowire

Similar to the investigation of nanowires, we compare these MD simulations to SEM observations of silver nanobelts, first in their as-synthesized state, and then after annealing at various temperatures. Since these nanobelts are newly developed, we also include X-ray diffraction (XRD) and TEM observations to better demonstrate their nature. Before annealing, Figure 6-7 demonstrates the as-synthesized condition of the nanobelts. A low-magnification SEM image (Figure 6-7-a) shows many high-aspect ratio nanobelts, inset with a higher magnification example of a serpentine nanobelt. SEM of several stacked nanobelts in Figure 6-7-b reveals the thickness of each to be in the range of 20 nm to 30 nm, and imaging by TEM (Figure 6-7-c) demonstrates that the belt is composed of joined nanoplates. The inset diffraction pattern of the indicated area of Figure 6-7-c confirms that the broad nanobelt surfaces are composed of (111) crystallography. XRD of the as-synthesized nanobelts (Figure 6-7-d) confirms this further, presenting only one peak corresponding to the (111) plane (in accordance with JCPDS card number 00-001-1164). Corresponding XRD on synthesized nanobelt powder reveals this structure to be uniform, and all nanobelts to share this (111) broad surface. This combined characterization confirms that the model nanobelt segment in the MD simulation is a good representative of the as-synthesized material.

Figure 6-8 shows SEM images of five batches of nanobelts, each annealed at a different temperature for 10 hours. After annealing at 200˚C, Figure 6-8-a reveals that the nanobelts remained stable, as predicted by the MD simulation. Inset is a high magnification view, demonstrating that the surface and edges of the nanobelts are intact. It is worthwhile to mention that the PMAA that cover the surface of the nanobelts will degrade around 150˚C [83]; therefore, it cannot affect our the stability observations. Similar to 200˚C, after annealing at 300˚C, the nanobelts remained stable (Figure 6-8-b), and did not sinter to one another (Figure 6-8-c). The nanobelts remain stable enough to maintain their high-aspect ratio form when annealed at temperatures of 400˚C and 500˚C (Figure 6-8-d and e). Insets show that the edges are still intact at 400˚C (Figure 6-8-d), but after exposure to 500˚C the edges have eroded and contacting nanobelts have begun to sinter together (Figure 6-8-e), although the belts have kept their one-dimensionality. After 10 hours of annealing at 600˚C (Figure 6-8-f), the nanobelts are found to be thermally unstable, and have lost their high-aspect ratio morphology due to the continuing diffusion of atoms at high temperature, as predicted by the simulations.

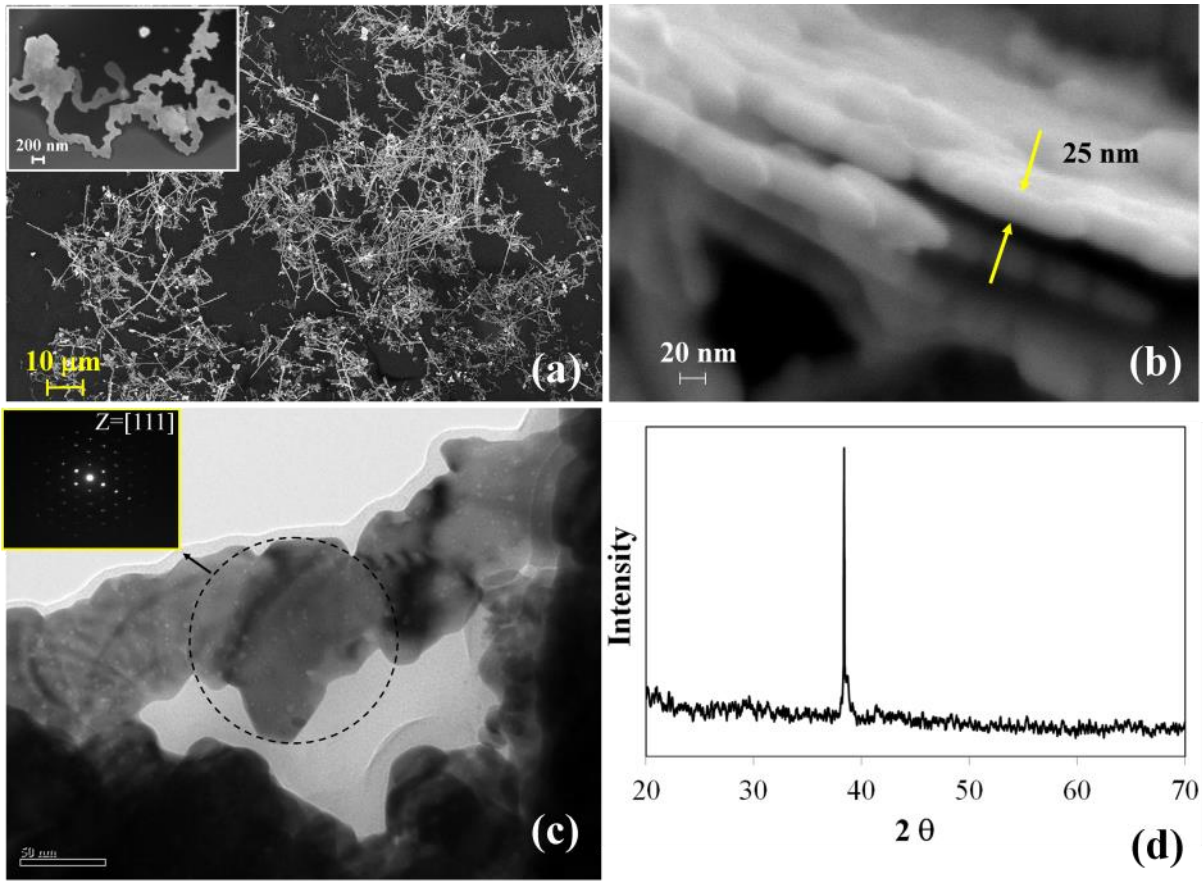

Figure 6-7: a) Synthesized silver nanobelts. The added image shows a single silver nanobelt; b) thickness of silver nanobelts; c) TEM image of a silver nanobelt, the added images shows the selected area diffraction pattern of the marked area; d)X-Ray diffraction pattern of synthesized silver nanobelts.

XRD patterns of the annealed nanobelts at different temperatures are presented in Figure 6-9-a. These XRD patterns reveal that the crystal structure of the nanobelts did not change after annealing at the 200˚C, 300˚C, and 400˚C. At 500˚C, there are two very small peaks belong to (200) and (220) planes of silver crystal (indicated by arrows on the Figure 6-9-a). Figure 6-9-b shows an SEM of a nanobelt after annealing at 500˚C, and Figure 6-9-c presents EDX analysis of the circled area of Figure 6-9-b. Combined, these confirm that this sample was not corroded by sulfur, and that the small structural change observed by XRD is because of sintering and changes in the morphology of the particles. The XRD pattern of the annealed sample at 600˚C has completely different crystal structure, confirming

that degradation occurred at this temperature. This is in agreement with MD simulation and SEM images of the sample after annealing at this temperature (Figure 6-5-f and Figure 6-8-f).

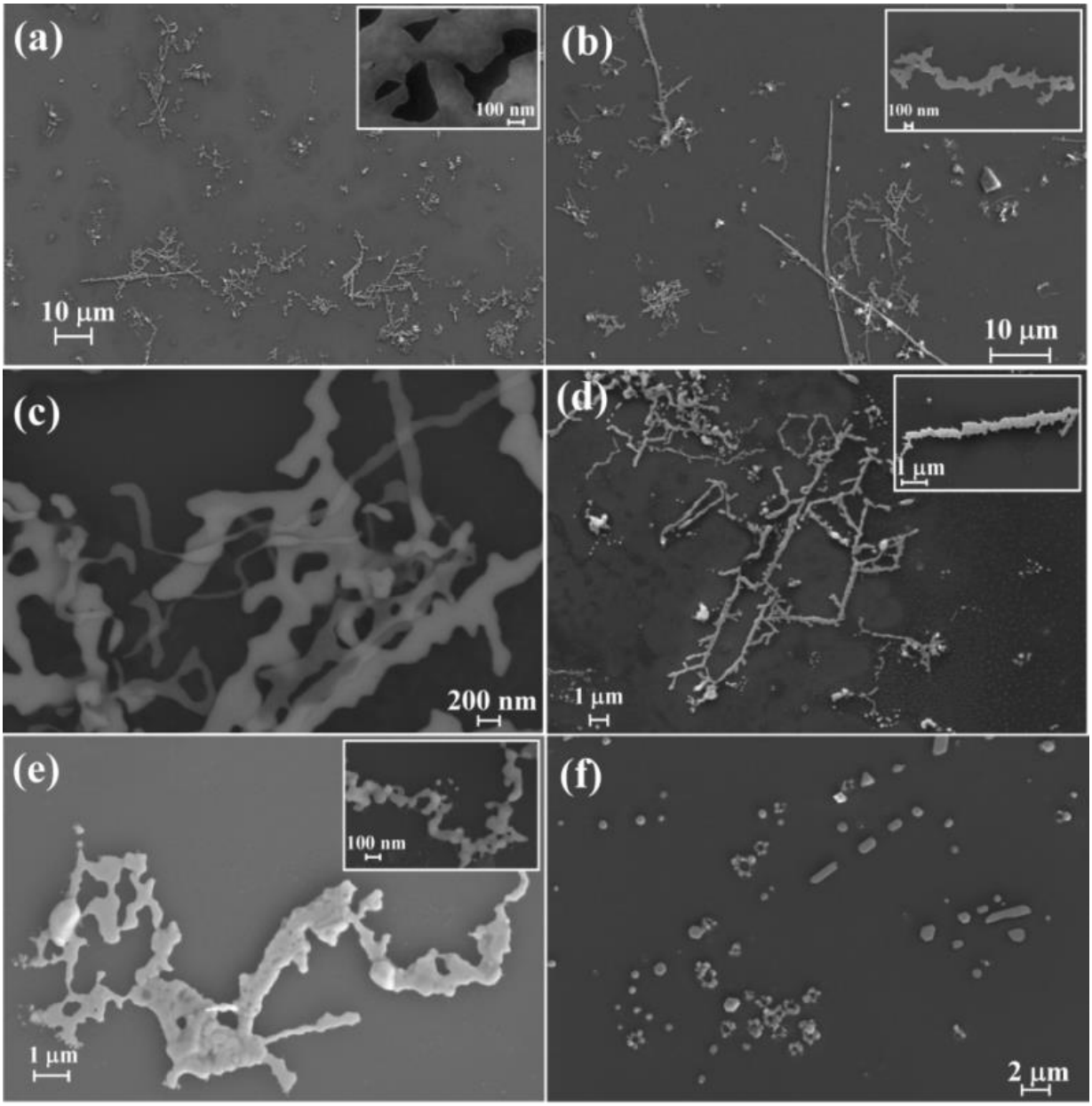

Figure 6-8: a) Silver nanobelts after 10 hours annealing at 200˚C; b) Silver nanobelts after 10 hours annealing at 300˚C; c) Agglomerated silver nanobelts after 10 hours annealing at 300˚C are stable and did not sinter; d) Silver nanobelts after 10 hours annealing at 400˚C; e) Silver nanobelts after 10 hours annealing at 500˚C; f) Silver nanobelts after 10 hours annealing at 600˚C;

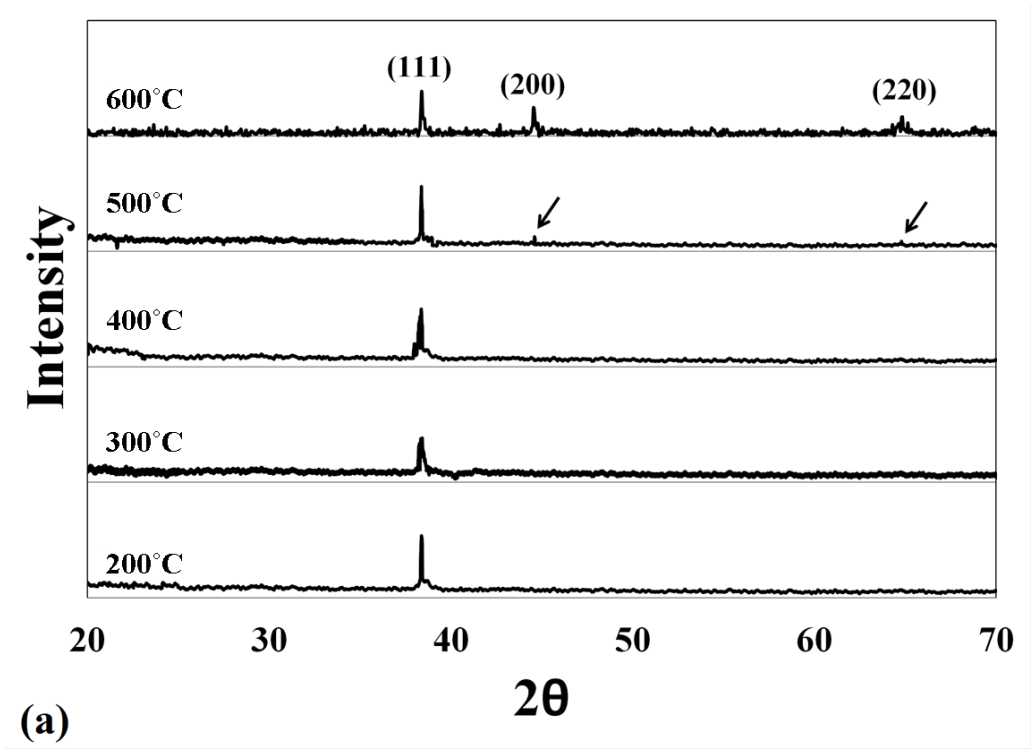

Figure 6-9: a) XRD pattern of the annealed samples at 200˚C, 300˚C, 400˚C, 500˚C and 600˚C; b) SEM of the annealed sample at 500˚C; d) EDX analysis of the marked area of the SEM image (b).

6.1.3 Summary

We have demonstrated the importance of morphology and surface atomic arrangement as an independent influence on the thermal stability of metallic nanoparticles in the 2nm – 100nm size regime. This is a fundamental issue, which should be addressed first when studying a nanoparticle at high temperature, which has not been previously addressed by the literature. To do this research we

performed comparative studies of silver nanowire and silver nanobelts by both MD simulation and experimental observation. These particles are excellent candidates for this study because both of them are one-dimensional and their lengths are in the same range, while their crystal textures are completely different. For pentagonal silver nanowire, the MD simulations and experimental observations indicate inherent thermal instability due to most surfaces being (100) crystallography. This instability results in the erosion and diffusion of atoms across the surface, followed by their recrystallization as new clusters. The greatest erosion of these surfaces appears to occur at the edges between two adjoining (100) surface. This is likely in part due to the geometry of the cross section placing the atoms in proximity to two high-energy surfaces. Through this process, the nanowires appear to favor the formation of new surfaces with (111) crystallography, and the obstruction of (100) planes by the recrystallizing clusters. All of this has been observed without detectable contaminates, demonstrating this degradation is independent of chemical attack. In contrast to silver nanowires, the MD simulations and experimental observations indicate that silver nanobelts are stable up to 600˚C, which makes them suitable for high-temperature functional materials. These results showed that the broad and flat (111) surfaces of the nanobelts were highly resistant to the effects of high temperature, which supports the prior statement that low energy crystal planes with high packing density provide better thermal stability. This case study clarifies that the surface texture of a nanoparticle plays a key role in stability. Based on the presented results, increasing temperature provides enough energy for the surface atoms to displace and degrade the nanoparticle, independent of other contributors. This thermodynamic inherent instability is a fundamental issue and must be considered when selecting nanoparticle for high temperature applications. In the case of silver nanowires, sulfidation has been investigated as the cause of thermal instability before this research. However, this research demonstrates that pentagonal silver nanowires are inherently unstable because of their high energy structure, and will degrade even in a non-corrosive atmosphere. Therefore, although sulfidation is a factor to be investigated, it is accompanied by an inherent thermodynamic instability that limits the performance of silver nanowires in high-temperature applications. In contrast, silver nanobelts are demonstrated to be a high thermal stability one-dimensional silver nanoparticle, which might be a feasible and high performance candidate for different nanotechnology applications. In addition, the intrinsic stability of silver nanobelts promotes them as a model nanoparticle for further research into the mitigation of degradation by chemical attack.

6.2 Surface induced amorphous solid shell: A new explanation for melting of nanoparticles contradicting surface pre-melting

The melting of nano-scale particles is a complex phenomenon because of lower melting temperature of these particles compared to large-scale ones, and "surface premelting". Among those, many fundamental questions related to the possible existence of a liquid layer on the surface of nanoparticles prior to reaching melting temperatures remain unanswered. Based on the literature, there is no doubt that a disordered layer can be created on the surface of crystalline structures because of thermal annealing at a range of temperatures below the melting point. However, the physical state of this disordered surface layer has not been clarified. In this section, the melting of a metallic nanoparticle is investigated with a view to clarifying the nature of this disordered surface layer.

6.2.1 Introduction

The surface melting of nanoscale particles, at temperatures less than the melting point of these materials, began to be investigated in the 1980s when research into nanoscience and nanotechnology became popular. It is a well-established premise that many of the outstanding capabilities of nanotechnology are due to the high specific surface area and surface crystal texture of nanomaterials. However, these characteristics of nanoparticles can be affected by surface melting, which causes shape, size and surface texture change: an important phenomenon from theoretical and practical point of view. [76, 125, 131, 132, 152-155]. Hence, the thermodynamics and kinetics of this phenomenon should be well understood as they form basic knowledge in this field.

Although research into surface melting of nanoparticles began when nanoscience started to grow, the phenomenon has a longer history. To the best of our knowledge, "surface premelting" was reported for the first time in 1942, when Stranksi claimed that melting began at a temperature below the melting point of the material on some surface crystal planes [156]. The concept of a quasiliquid, introduced by Stranksi, has been the subject of many experimental and theoretical research works. These attempts, which now include nanoscale investigations, can be divided into thermodynamic models, experimental observations, and atomistic simulations.

Based on classical thermodynamics, it is known that for a pure material at a constant pressure only one degree of freedom is available and, hence, any phase transformations happen at a singular point in the energy-temperature domain [157]. Based on this basic rule of thermodynamics, a pure material has a specific melting temperature that is determined by the energy balance between its solid and liquid phases. Considering the contribution of the surface energy to the energy of the material, thermodynamic

calculations can provide a clear explanation for the size dependent melting temperature of small particles [158, 159]. However, the coexistence of two phases, solid and liquid, within a temperature range needs one more degree of freedom that is not available for the pure material at constant pressure. Recently, the phase-field simulation method has been utilized to explain "surface premelting" or the coexistence of liquid and solid phases at a range of temperatures [160, 161]. Phase field is a mesoscale simulation method that establishes a system by defining a phase field [162]. To illustrate coexisting solid and liquid phases over a range of temperatures, the above-mentioned research considered a bistable phase, a solid particle with a liquid shell, as an individual phase. By using this approach, the bistable phase is in equilibrium with purely solid and liquid phases at two singular temperatures and the premelting phenomenon can be demonstrated thermodynamically. The key problem with this model is the nature of the bistable phase; it must be different from both the solid and liquid phases to fulfill the thermodynamic requirements. However, in the research, the bistable phase was translated as the "surface premelting" of the solid phase, which is in contradiction to thermodynamic rules. Therefore, further research is required to establish the so-called "surface premelting" phenomenon, using thermodynamic modeling based on classical or nano-scale thermodynamic rules.

Surface melting has been examined experimentally by investigating the surface structure of metallic nanoparticles. Techniques such as low-energy ion scattering [163, 164], low energy electron diffraction [111, 165, 166], atom scattering [167], grazing angle x-ray diffraction [168-170], low energy ion scattering [171],and neutron scattering [172] have been employed to make the observations. All of these methods have successfully illustrated surface disordering produced after annealing at high temperatures (close to the melting point), which leads to surface roughening and/or amorphization. Some researchers have interpreted this amorphous layer as a liquid and reported their findings as evidence for "surface premelting". However, experimental evidence for a structural factor that directly distinguishes a liquid surface layer from an amorphous solid has not yet been reported. Another observation which has been purported as experimental evidence of "surface premelting" is the thermal instability of nanoparticles [173, 174]. The shape and morphology of nanoparticles can be changed dramatically via thermal annealing. This shape evolution of the nanoparticles, called crystal-crystal phase transformation, can be explained by assuming the hydrodynamic flow of a surface liquid layer below the melting point of the nanoparticles [174]. Although the "surface premelting" hypothesis is able to explain the nanoparticles' shape changes at temperatures below the melting point, phenomena such as surface diffusion and high mobility surface defects (*i.e.*, adatoms), can also be used to explain shape and

morphology changes of nanoparticles in solid state and more research is required to compare and experimentally validate these mechanisms.

Finally, the "surface premelting" problem has also been approached through molecular dynamic (MD) simulation. One of the first attempts to explore surface melting through MD was reported in 1973 and investigated the melting of a fifty-five atomic cluster [175]. This research revealed that the cluster melted at a specific melting point and the diffusion coefficient of the surface atoms increased before melting. Researchers claimed that the unexpected diffusion coefficient change was evidence for surface melting of the cluster. Since that time, many MD simulations have been done to verify and characterize "surface premelting", especially at nano-scale [108, 176-187]. Some researchers have reported snapshots of the simulated crystals at different annealing times and temperatures to visualize high mobility surface atoms and the amorphization of the surface layer, which they submit as evidence of "surface premelting" of the nanoparticles. These visualizations were supported by calculating various structural indexes such as the Lindemann index, the mean-square displacement of atoms, the number of disordered atoms, the potential energy of the atoms, the structural ordering parameter, and the radial distribution function of surface and bulk atoms . MD simulations have successfully demonstrated that the surface of a crystal will change from a well-defined surface crystal structure through annealing. However, there are few reports in the literature that investigate the mechanisms of surface crystal. Reports have been limited to illustrating the existence of individual high mobility atoms [178]. However, individual atoms on the surface of a structure are a well-known surface defect, known as adatoms, and cannot be considered as a liquid phase until they join with each other and make liquid clusters [109]. Therefore, research into the presence of a liquid layer on the surface of nanoparticles at temperatures below the melting point, which examines the physical state of the surface clusters, should be conducted.

In this research, the MD simulation method was utilized to investigate whether the disordering of a nanoparticle's surface at high temperatures leads to surface melting or whether this layer remains solid. To carry out this investigation, a truncated cube of silver was used, and the melting of silver clusters, and the surface evolution of particles below the melting point were studied.

6.2.2 Simulation Method

The simulated nanoparticle contained 28741 atoms, with the initial state designed as a truncated cube. To prepare potential energy data, the model was run for 1×10^6 time-steps at temperatures outside the range of 900K to 1200K. Between 900K to 1200K phase transformation occurred. Around the phase

transformation, the model was run for 2×10^6 time-steps for all data points because the phase transformation occurs very slowly and the model needs to run for more time-steps to specify the thermodynamically stable phase. The potential energy of the silver nanoparticle versus temperature was calculated by obtaining the average of the potential energy data of the last 100,000 time-steps of the simulation for each temperature.

The radial distribution function (RDF) was calculated by finding the pairwise distance between the atoms in the cut-off radius by using equation 3 [85]:

$$g(r) = \frac{\langle N(r,\Delta r)\rangle}{\frac{1}{2}N\rho V(r,\Delta r)} \qquad (3)$$

Where $\langle \quad \rangle$ represents time averaging, N is the total number of atoms, $p = \frac{N}{V}$ is the number density, $N(r,\Delta r)$ is number of atoms found in a spherical shell of radius r and thickness Δr, and $V(r,\Delta r)$ is the volume of the spherical shell [85]. The potential energy of the nanoparticle is calculated by summing the potential energy of all of the atoms, and for each atom, the potential energy is calculated by summing the bonding energy of that atom and its neighbors.

Stress tensor of each atom was calculated through computing the applied force on the atom the by all atoms in cut-off radius of the desired atom in each time step [188, 189]. To measure the internal pressure, the stress tensor of each atom during 1000 successive time steps of the MD simulation was calculated and the average of the radial stress was found. Then, the nanoparticle was divided to concentric spherical shells with thickness of 1Å and mean radial stress of the atoms of each shell was reported as internal stress.

6.2.3 Results

Figure 6-10 demonstrates the potential energy change of the silver nanoparticle versus temperature in the range of 300K to 1400K. To prepare this graph, at each temperature, initial arrangement of atoms was formed the perfect and defect-free truncated cube silver nanoparticle. This grapH uncovers a sharp jump in the potential energy curve between 1087K and 1087.5K (inset curve). It is well known that the jump in potential energy represents a first order phase transformation. Moreover, it is apparent in Figure 6-10 that a change in the slope of the potential energy curve occurred between 1000K and 1050K, which indicates a second order phase transformation. These results help us to divide the behavior of the nanoparticle into four distinct regions: T≤1000K, 1000≤T≤1087, 1087≤T≤1087.5 and T>1087.5. The effect of thermal annealing on the nanoparticle's crystal structure, surface, and physical state in these temperature ranges will be discussed below.

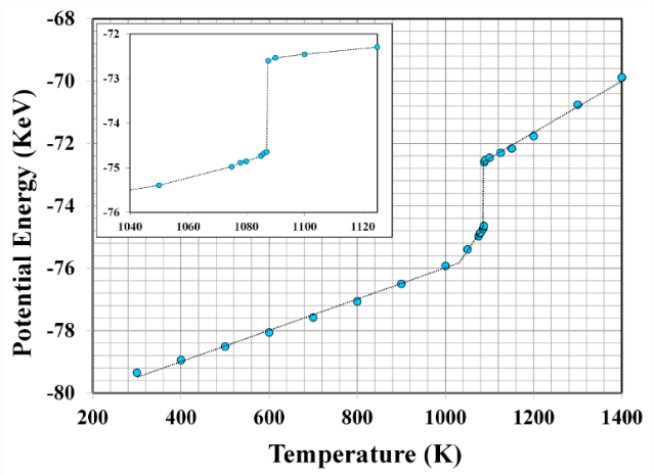

Figure 6-10: Potential energy of the silver nanoparticle versus temperature. Inset shows an enlarged section of the grapH in the range of 1040K to 1125K.

Figure 6-11 demonstrates the nanoparticle after annealing at 300K, 900K, and 1000K. As can be seen in Figure 6-11-a, the nanoparticle's surface remained intact after annealing at 300K. Increasing the temperature to 900K led to several surface defects: adatoms, vacancies, and surface clusters. Further increasing the temperature to 1000K resulted in more defects on the surface. The observed surface defects were created by thermal phonons. At lower temperatures, the thermal phonons do not have enough mechanical energy to create defects. However, at higher temperature, stronger mechanical waves reach the surface and can detach surface atoms from the crystal network and create defects. Figure 6-12 reveals the creation of an adatom and a vacancy under the impact of a strong thermal phonon at 900K. An atom was marked in the original network (Figure 6-12-a). When the phonon reaches the surface, the atoms move from their position and are compressed together (Figure 6-12-b), after which the atoms release their stored energy and return to their original position. However, the kinetic energy of the marked atom was high enough under this condition that it was able to slide over its neighbors and reach the surface, and subsequently moving around on the surface (Figure 6-12-c and d). The atom's trajectory is illustrated in Figure 6-12-e in which, the position of the marked atom in the four fist snapshots (Figure 6-12a-d) is showed on the curve. Movement of this atom led to the creation of an adatom and a vacancy. Adatoms are high energy and unstable and hence, they will react with other surface defects and fill the vacancies or make surface clusters by joining to other adatoms Since the energy of a thermal phonon is temperature dependent, more defects will be created on the surface at higher temperatures (compare Figure 6-11-b and Figure 6-11-c). Based on these observations, at

temperatures below 1000K the silver nanoparticle is a crystalline particle but, depending on the temperature, surface defects may observable.

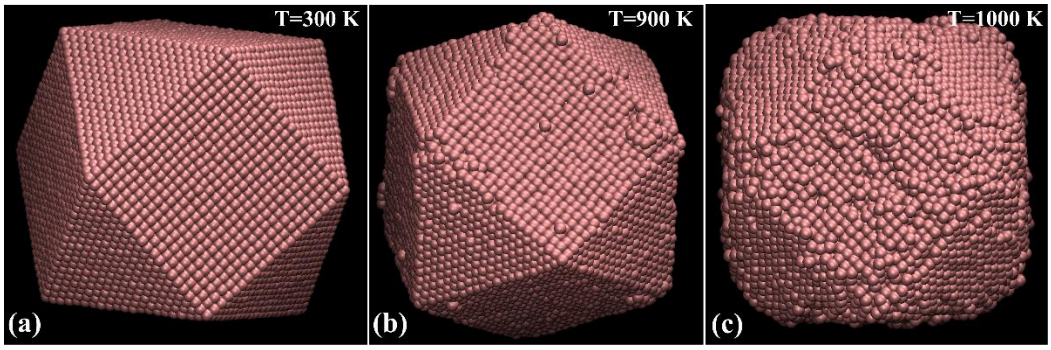

Figure 6-11: Silver nanoparticle after 2×10^6 time-steps annealing at: a) 300K; b) 900K; c) 1000K.

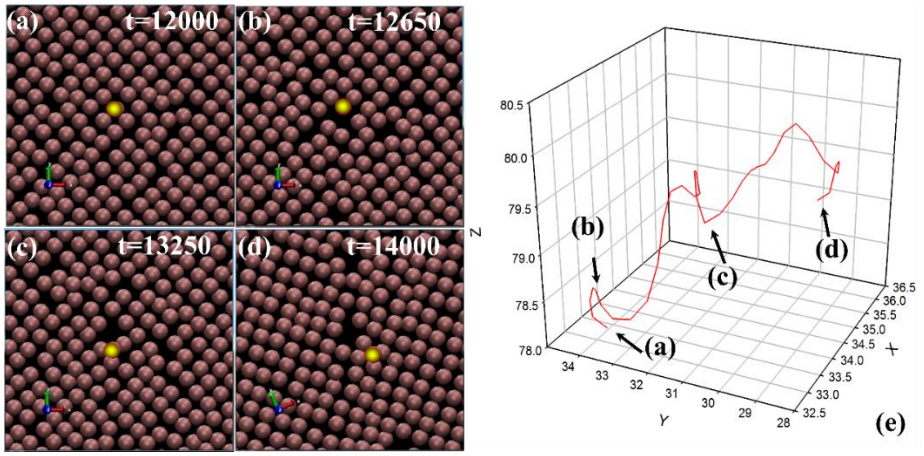

Figure 6-12: Creation of an adatom by thermal phonons. a) initial position of the atom; b) position of the atom when the thermal phonon reaches it; c) atom thrown out from the lattice when its energy is released; d) displacement of the atom on the surface;
e) trajectory of the atom's displacement.

To clarify the nature of the first order phase transformation of nanoparticles between 1087K and 1087.5K, the atomic structure of the cluster before (1087K) and after (1087.5K) the phase transformation are shown in two snapshots (Figure 6-13-a, and Figure 6-13-b). Based on these images, it appears that the cluster has a crystalline structure before the phase transformation, while after the transformation the atoms are randomly arranged. Figure 6-13-c demonstrates the potential energy change of the nanoparticle during annealing at 1087K and 1087.5K. This figure reveals a significant difference between the two potential energy curves. At 1087K, after the initial potential energy increase

during the first 0.2×10^6 time-steps, the potential energy remains constant. However, by increasing the temperature by 0.5K, a different trend in the potential energy of the cluster is observed. From the time-step number 0.75×10^6, the potential energy of the sample began to increase, and this trend continued up to 1.2×10^6. The potential energy remaining stable after this point. The structure of the nanoparticle before and after this potential energy change have been added to the figure and confirm that during this phase transformation the crystal structure of the nanoparticle changes from a crystalline structure to a random one. In addition, the radial distribution function (RDF) of the stable cluster at 300K (when the cluster has a crystalline structure; Figure 6-11-a), 1087K, and 1087.5K are shown in Figure 6-13-d. The RDF curve at 300K depicts the typical RDF curve of a crystalline phase; at 1087.5K it depicts the typical RDF curve of a liquid phase [85]. At 1085K the RDF curve's peaks are broad but detectable, which is predictable for a crystal at high temperature with high thermal vibration. Therefore, the observed first order phase transformation can be interpreted as the melting of a crystalline nanoparticle and hence, the melting point of the silver nanoparticle lays between 1087K and 1087.5K; above this temperature range the particle is liquid.

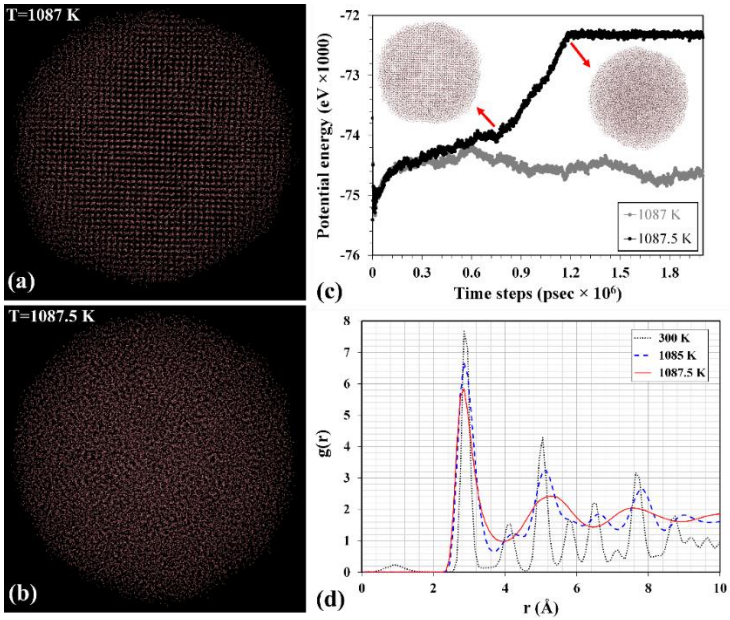

Figure 6-13: a) Snapshot of a silver nanoparticle annealed for 2×10^6 time-steps at 1087K; b) snapshot of a silver nanoparticle annealed for 2×10^6 time-steps at 1087.5K; c) potential energy change of the nanoparticle during annealing at 1087K and 1087.5K; d) radial distribution function of the silver nanoparticle after annealing at 300K, 1085K, and 1087.5K.

Figure 6-14shows the surface texture and arrangement of atoms of a nanoparticle after annealing at 1050K for 2×10^6 time steps. This figure depicts that a disordered atomic layer covers the surface of the nanoparticle and shape of the particle is change from original truncated cube toward a spherical one, while the internal atoms are arrange in a crystalline form. Comparison between the shape and structure of two annealed nanoparticles at 1000K and 1050K, before and after the second order phase transformation (Figure 6-11-c and Figure 6-14) illustrates that the main differences between these two nanoparticles are the disordered surface layer and particle's shape change. Our MD simulation demonstrated that the disordered layer was created by accumulation of surface defects that created by the aforementioned mechanism (Figure 6-12). However, the higher temperature leads to stronger thermal phonons in the nanoparticles and so, increases the defect density ultimately resulting in a continuous disordered surface layer. Therefore, the above-mentioned slop change in potential energy curve of the silver nanoparticle versus temperature between 1000K and 1050K (Figure 6-10) is observed because of the creation of a continuous disorder shell on crystalline core. As discussed before, the crystalline nanoparticle remains solid at any temperature less than the melting point. Hence, the potential energy of the crystalline core would follow the same trend that observed before creation of disorder surface layer. Therefore, the surface disorder layer might be responsible to the slop change. This disorder surface layer of nanoparticle might be what researchers detected on the surface of nanoparticles by using different experimental techniques. Three different physical state can be proposed for this layer: super-cooled liquid, amorphous phase that makes by quenching a liquid phase (amorphous phase A), and amorphous phase that makes by amorphization of a crystalline phase by creation of surface defects through increasing temperature to cause high energy thermal phonons (amorphous phase B). The super-cooled liquid is an unstable thermodynamic state in which, the atoms are able to flow under external stress filed. This phase can be transform to amorphous phase A (or glass phase) by enough fast cooling rate. This change is a reversible second order phase transformation. On the other hand, by definition, an amorphous phase is a non-crystalline solid that creates from crystalline solid by various mechanisms such as sever mechanical deformation (amorphous phase B) [190].

To investigate the physical state of the disorder layer, surface atoms should be analyzed. However, the surface layer is being mechanically impacted by thermal phonons. Because of the disordering of the surface layer, the mechanical waves are not able to propagate into this layer and hence, the phonons deform the layer. Considering the energy and density of thermal phonons at a temperature close to melting point, these impacts lead to continues deformation of the thin disorder surface layer and hence,

existence of very high mobility surface atoms, which overlay a great deal of noise on any observation. Therefore, the structural indexes such as surface diffusion coefficient, root mean square displacement, and Lindemann index cannot be employed to ascertain whether the surface layer is solid or liquid and hence, another approach must be selected for this purpose.

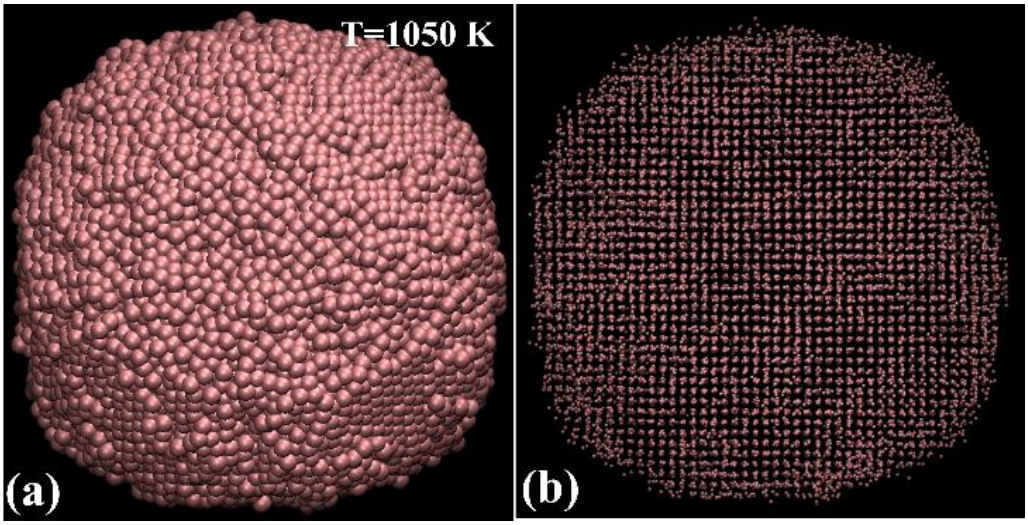

Figure 6-14: a) Silver nanoparticle after 2×10^6 time-step annealing at 1050K, b) cross section of the nanoparticle.

If the disordered surface layer is proposed as super-cooled liquid, heating a nanoparticle with surface disorder layer to melting point creates an equilibrium liquid layer, which promote melting process. In the case of amorphous phase A, increasing temperature of the nanoparticle to melting point may induce some residual stress in the solid core that will released by transformation of this amorphous phase to liquid. However, if we assume the disordered surface layer as amorphous phase B, heating nanoparticle to melting point may introduce some residual stress or internal pressure due to the different thermal expansion coefficients of the crystalline and non-crystalline solids and this pressure shifts the melting point. Therefore, to distinguish if the disordered surface layer is liquid or solid, melting point of the nanoparticle must be ascertained. Hence, we annealed a nanoparticle at 1085K for 2×10^6 time-steps to form the surface disordered layer and then annealed at different temperatures for 10×10^6 time-steps to find the melting point of this nanoparticle. The result of this simulation illustrates that the melting point of the nanoparticle is shifted about +3˚C (Figure 6-15). This simulation was repeated for a nanoparticle that annealed at 1000K for 2×10^6 time-steps that only creates individual surface defects (Figure 6-15), which demonstrated that the melting point of this nanoparticle is exactly same as the perfect crystal.

Hence, higher melting point of the nanoparticle with disorder layer confirms the existence of a lower internal pressure compare to original nanoparticle.

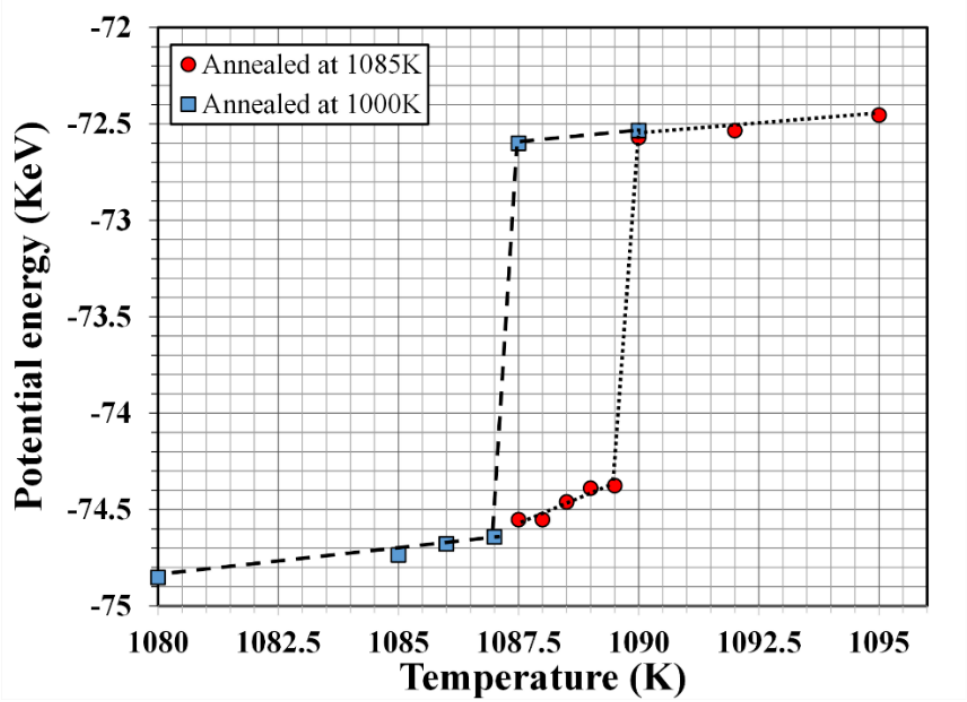

Figure 6-15: Potential energy versus temperature for two annealed nanoparticles at 1000K, and 1085K.

To evaluate the above-mentioned explanation, the internal pressure of the nanoparticle was calculated for three different cases. Figure 6-16-a demonstrates the internal pressure and number of atoms in each shell, when the nanoparticle was annealed at 1000K. In this case, the internal pressure of the shells are mostly positive which demonstrates the effect of the surface energy of the nanoparticle. When the nanoparticle partially melted, pressure of the liquid surface layer on solid core is around zero and the internal crystalline solid is under compressive pressure (Figure 6-16-b). However, when a nanoparticle annealed at 1085K to create the disorder surface layer and then annealed for 1×10^{10} time steps at 1089.5K, a positive pressure was induced on the surface layer (marked Figure 6-16-c), and rest of the shells are almost under compressive pressure. This internal pressure distribution of the particle confirms that the surface layer of the nanoparticle was amorphous solid and before melting point, the particle is completely solid. The time of this simulation is 10 times longer than the time scale that is required for melting the particle (Figure 6-13-c). Therefore, duration of this simulation seems enough to claim that the layer is not liquid due to stability of the induced pressure over entire simulation at 1089.5K.

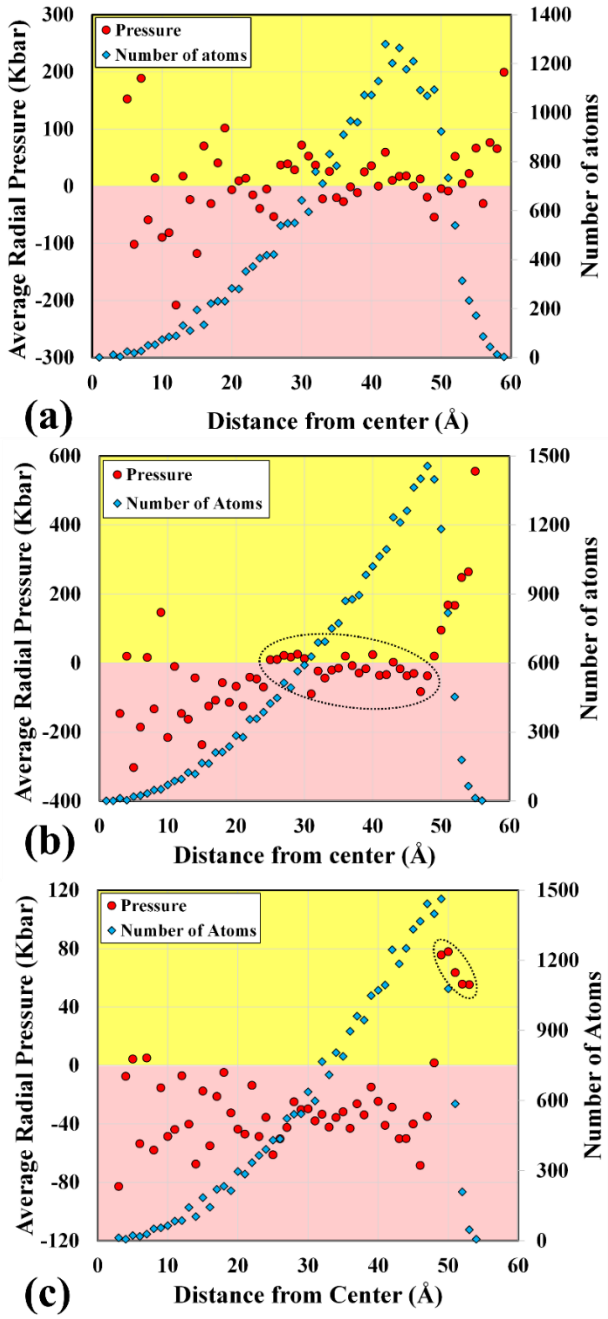

Figure 6-16: Average radial pressure of concentric spheres of atoms with thickness of 1Å and number of atoms in each shell versus distance from center (radius) of: a) a nanoparticle after 2×10^6 time steps annealing at 1000K; b) a partially melted nanoparticle at the melting point (Temperature: 1087.5K,

Time step:1.1 $\times 10^6$); c) a annealed nanoparticle with a disorder surface layer at 1089.5K for 1×10^{10} time steps.

6.2.4 Summary

This research demonstrates that the melting of the nanoparticle occurred at a specific temperature and that surface melting does not happen before the melting temperature, which is compatible with classical thermodynamic. The mechanical waves generated by the thermal phonons are strong enough to overcome the cohesive energy of the surface atoms and create surface defects such as adatoms, vacancies, and surface clusters. The density of these defects increases as the temperature increases and the accumulation of defects leads to an amorphous layer covering the surface of the nanoparticle in a range of temperature below melting point. By investigating internal pressure of the nanoparticle, we demonstrate that the surface layer is a non-crystalline solid, which remain solid up to the melting temperature. The existence of this layer was confirmed before this research by experimental observations, and this new definition is compatible with previous observations in the litrature.

Chapter 7
Applications

In this research, one- and two- dimensional silver nanoscale supercrystals were synthesized. Beyond special features of the products such as unique surface crystal texture and high stability of the silver nanoparticles, simplicity is another interesting aspect of the developed method. Every usual synthesis takes only two minutes to complete. After vacuum filtration and drying, the product is around 0.9 gr silver cake. This cake can be stored for a long time without reaction with environment, thanks to PMAA which has covered surface of the nanoparticles. On the other hand, when a piece of the cake is put in a liquid media such as water or one of the alcohols like ethanol and ultrasonicated for few minutes, the silver nanoparticles will be easily dispersed. This simple, fast and high-yield production, along with easy storage and good dispersion capability make this material an ideal one for industrial applications. Therefore, there is a huge potential for future researches into employing this material for different applications. Here in this chapter, two applications, one of them for silver nanobelts and the other for silver nanosheets will be introduced as two examples of applications.

7.1 Application of silver nanobelts

As first application, one-dimensional silver nanobelts were employed as one-dimensional conductive nanomaterial to enhance electrical conductivity of Electrical conductive adhesive (ECA) [191]. The idea behind this hybrid composite is bridging between silver flakes by one-dimensional silver nanobelts. For this purpose, the silver nanobelts along with silver flakes (Aldrich, 10 mm) at different weight fractions were added to epoxy (diglycidyl ether of bisphenol A, DERTM 322, DOW chemical company, USA). Figure 7-1 shows the conductivity of prepared hybrid ECA in comparison to conventional ECA. This figure shows that adding 1 wt% of silver nanobelts to conventional ECA is able to enhance conductivity of the composite by 1300%. The presented results is preliminary results of application of the fabricated structures in different applications and more research is required to clarify, properties and potential applications of this new grade of silver materials.

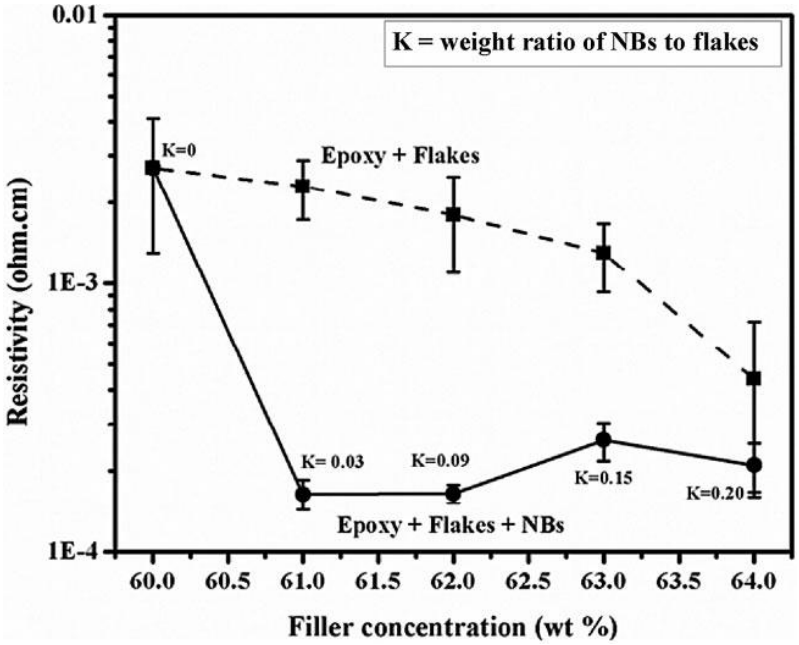

Figure 7-1: The bulk resistivity of the hybrid ECAs (solid line) and the conventional ECAs (dashed line) at various silver concentrations [191].

7.2 Application of Silver nanosheets

Fabrication of nanoscale and microscale machines and devices is one the goals of nanotechnology. For this purpose, different materials, methods, and devices should be developed. Among them, various types of miniaturized sensors are required to build the nanoscale and microscale systems. In this research, we introduce a new nanoscale sensing material, silver nanosheets, for applications such as nanoscale and microscale gas flow sensors. The silver nanosheets were synthesized through the reduction of silver ions by ascorbic acid in the presence of poly (methacrylic acid) as a capping agent, followed by the growth of silver in the shape of hexagonal and triangular nanoplates, and self-assembly, and nanojoining of these structural blocks. At the end of this process, the synthesized nanosheets were floated on the solution. Then, their electrical and thermal stability was demonstrated at 120˚C, and their atmospheric corrosion resistance was clarified at the same temperature range by thermogravimetric analysis (TGA). the silver nanosheets was employed for fabricating airflow sensors, first by scooping out the nanosheets by means of a sensor substrate; after that, drying them at room temperature and then annealing them at 300˚C for one hour. The fabricated sensors were tested for their ability to measure

airflow in the range of 1 to 5 ml/min, which resulted a linear response to the flow of air in this range with a response and recovery time around 2 seconds. Moreover, continuous dynamic testing demonstrated that the response of the sensors were stable and hence, the sensors can be used for a long time without detectable drift in their response. Detail of the fabrication ad characterization is discussed in the rest of this chapter.

7.3 Introduction

The fast development of nanotechnology promises the existence of microscale- and nanoscale-machines in the not too far future. Generally, the construction of a nanoscale or microscale system requires synthesis or fabrication of appropriately scaled structural blocks, a facile energy source, a sound and economically feasible fabrication and assembly process, and adequate control and monitoring to help achieve these goals. Scientists can employ the numerous breakthroughs already made by the scientific and technological communities [192]. However, from where we are now to the desired destination, a lot of work remain to be done. Nanosensors are crucial to these efforts. Employing nanomaterials for sensing has its own benefits because of the constructive effects of scaling down the sensing material to nanoscale. The nanoparticles are being employed to build a new generation of sensors with a bigger sensitivity range than was not achievable with large-scale sensing materials [163, 193, 194]. However, for nanoscale or microscale systems, not only are these new sensors required, but also the miniaturization of conventional sensors such as force, strain, weight and flow sensors. Among them, gas flow sensors are urgently needed for a wide range of applications - from nano- and micro-mechanical systems to medical apparatus and nano-bioassays [195]. Different types of large-scale sensors have been fabricated to measure gas flow meanwhile, the fast development of micro and nanoscale technologies is increasing the demand for new miniaturized sensors [196]. The hot wire anemometer, currently available in macro scale, is one of the most common flow sensors. In a hot wire anemometer, the temperature and as a consequence electrical resistance of a metallic wire is changed by gas flow. The convection heat transfer equation, the heat capacity of the sensing material, and the relation between the temperature and electrical resistivity of the sensing material are the governing equations that determine the sensor's sensitivity [196, 197]. Generally, increasing the surface area and decreasing the mass of the sensing material enhance the sensitivity of a sensor to the external stimulus. The thermal and electrical stability and mechanical strength of the sensing material are other affecting parameters that must be considered in designing a reliable flow sensor. Hot wire anemometers have a

wide range of applications, although they are not suitable for some conditions such as a high vibration environment. In addition, fabricating micron- or nano-scale hot wire flow meters usually requires a very expensive apparatus [197-207]. Therefore, new feasible methods for the design and fabrication of accurate gas flow sensors for current and future applications is an important research topic.

One- and two-dimensional metallic nanoparticles can be considered as potential candidates for the sensing material of a hot wire flow meter. It is reported that the electrical conductivity of the nanoparticles is decreased and the temperature dependency of their electrical conductivity increased by reducing the size of the nanoparticles [208]. Hence, metallic nanoparticles are a good candidate for sensing gas flow from the electrical property point of view. High specific surface area and acceptable mechanical strength are two other advantages of metallic nanoparticles for this application. On the other hand, thermal stability [18], electrical stability or electromigration resistance [16, 17] and high temperature corrosion [146] are important issues that must be considered when we want to employ metallic nanoparticles as sensing material of the flow sensor. Among different metals, silver is a noble metal with excellent electrical and thermal conductivity, high mechanical strength and good corrosion resistance. In addition, silver nanoparticles have unique properties which have led to much research into this material. As a result of these studies, various silver nanoparticles with different sizes and morphologies have been synthesized [38, 41]. All of these facts and the relatively lower price of silver in comparison to its competitors such as gold and platinum, make it a promising choice for hot wire sensor fabrication.

Recently, we synthesized a new type of silver nanoparticle by the simultaneous self-assembly and nanojoining of hexagonal and triangular silver nanoplates as structural blocks in the form of nanobelts, nanoflakes and porous nanosheets [122, 209]. Our synthesis is a fast, high yield and feasible method. The thickness of these nanoparticles, including the nanosheets, is around 25 nm and, the nanosheets can be designed to be in the range of few microns to few millimeters in diameter. We have found that the boundaries between the structural blocks are perfect crystals; that is, there are defect free, which is important conferring good electrical conductivity [122]. Another important feature of this new type of silver nanoparticle is its unique surface texture[122]. The majority of the surface area of this type of silver nanoparticles is composed of a closed packed (111) crystal plane, which is the result of the realignment of the hexagonal and triangular nanoplates during the lateral nanojoining process. We have demonstrated by molecular dynamic simulation and experimental observation that the silver nanobelts are stable at high temperature and remain intact over long time annealing at high temperature because of their unique low energy surface texture [153]. We have used this new type of silver nanoparticles as

filler material to enhance the electrical conductive adhesive performance [73]. In this current research, we have employed silver nanosheets to fabricate a mass airflow sensor. The synthesis process, sensor fabrication method and response of the sensor will be discussed in this paper. Additionally, the results of hot corrosion resistance investigation under atmospheric conditions and the electrical and thermal stability observations of the sensing material are reported to address the essential requirements for a long-lasting sensor application.

7.4 Experimental Procedure

7.4.1 Synthesis and characterization of the porous silver nanosheets

To synthesize silver nanosheets, 2.1 g of $AgNO_3$ (Sigma-Aldrich) was added to 60 ml H_2O and shaken for one minute to form a silver nitrate solution. A reducing solution was prepared separately by adding 0.68 g ascorbic acid (Alfa Aesar) and 0.16 ml poly (methacrylic acid, sodium salt) 40% in water (PMAA solution, Aldrich Chemistry, Typical molecular weight: 4,000-6,000) as a structure-directing reagent to 200 ml H_2O. The mixture was then vigorously shaken for one minute to dissolve the ascorbic acid. Synthesis was performed by adding the silver nitrate solution to the reducing solution. After a few seconds, the silver nanosheets self-assembled and floated on the solution.

Scanning and transmission electron microscopes (SEM and TEM) and optical profilometery were utilized to investigate the morphology and crystal structure of the synthesized nanosheets. To prepare SEM and optical profilometery samples, a silver nanosheet was put on a clean silicon wafer, then dried at 70°C by using a hot plate and annealed at 300˚C for one hour. For TEM observation, the nanosheet was put on a TEM grid, dried under room conditions and then annealed at 300˚C for one hour.

An x-ray diffractometery technique (XRD) was utilized to characterize the crystal structure of the synthesized silver nanosheets. To prepare XRD samples, the floating nanosheets were collected using a filter paper (Whatman® # 1001042). The sample was dried at 70°C, then the nanosheets were detached by peeling away the filter paper and putting the sample on a piece of glass. XRD was performed using an x-ray tube with a wavelength output of Cu-Kα_1 (λ = 0.154056 nm).

Thermal stability of the silver nanosheets was investigated by annealing of the nanosheets at 150°C for 100 hours. The morphology and crystal structure of the silver nanosheets after annealing were investigated by SEM and XRD. Hot corrosion resistance of the nanosheets was investigated using a thermogravimetery (TG) machine under flow of air. The electrical stability of the sensing material

was evaluated by passing 982 mA through it for 500 hours while the sensor was kept at 120°C, which is the working temperature of the sensor.

7.4.2 Sensor Fabrication and test

An alumina substrate with interdigitated electrodes (spaced about 100 μm apart) was used for sensor fabrication. This alumina substrate was equipped with a micro heater on the back side of the electrodes. A nanosheet was loaded onto the electrodes simply by scooping it from the solution surface. To do that, the alumina substrate was dipped into the liquid and used to pick up a nanosheet in such a way that this sheet sat on the electrodes. After that, the sensor was dried at room temperature and then annealed at 300˚C for one hour to remove the PMAA from the surface of the sheet. This sensor was installed in a chamber with a channel with a 1 mm^2 square cross section. To examine the sensor, it was exposed to air flowing at different rates, and its electrical resistance was measured by a 16 bit data logger at a rate of 10 data\sec. A moving average noise rejection filtering with a window of 5 data was used to smooth the data.

7.5 Results and discussion

7.5.1 Synthesis and characterization of sensing material

Figure 7-2-a shows a SEM image of a nanosheet, revealing that the silver nanosheet is a continuous mesh of silver with irregular shaped holes. The left inset of Figure 7-2-a is a high magnification side view of a nanosheet clarifying that the thickness of the nanosheets is 25 nm. The TEM image of a sheet is presented in Figure 7-2-b and demonstrates this sheet is composed of joined nanoplates. The selected area diffraction (SAD) pattern of the marked area of the TEM image is presented in Figure 7-2 -c. This SAD pattern confirms that the surface plane of the nanosheet is (111), although the structural blocks are not completely parallel. This tilt might have occurred during nanojoining, as predicted by molecular dynamic simulation [122]. The x-ray diffraction pattern of the nanosheets shows only one peak, belonging to the (111) crystal plane of silver (Figure 7-2-d), which confirms the supposed structure of the nanosheets. These combined characterizations demonstrate that the synthesized silver nanosheet is a very thin sheet of silver, with a (111) surface crystal texture. Therefore, because of their low mass and high surface area, silver nanosheets are an excellent candidate for use as a sensing material in hot wire anemometers. Moreover, the unique crystal structure and surface texture of the nanosheets could provide special properties for this type of nanoparticle, such as high stability, which may be beneficial for this sensing application.

The synthesis mechanism for this type of nanoparticle was elucidated in [122, 209]. After the nucleation of initial silver clusters through reduction of silver ions by ascorbic acid, the PMAA covers (111) crystal planes of silver and controls the growth process to synthesize the hexagonal and triangular nanoplates. These nanoplates move randomly in the solution, and if they get close enough to each other they will join. In the case of silver nanosheets, we added silver nitrate solution to ascorbic acid. The reduction reaction happens immediately at the top layer of the reducing solution where silver ions exist, and the product floats on the reactor. The right inset of Figure 7-2-a is a high magnification SEM image of a hexagonal structural block of the nanosheet, which is joined to the other structural blocks from one side. This SEM image verifies the proposed mechanism for the synthesis.

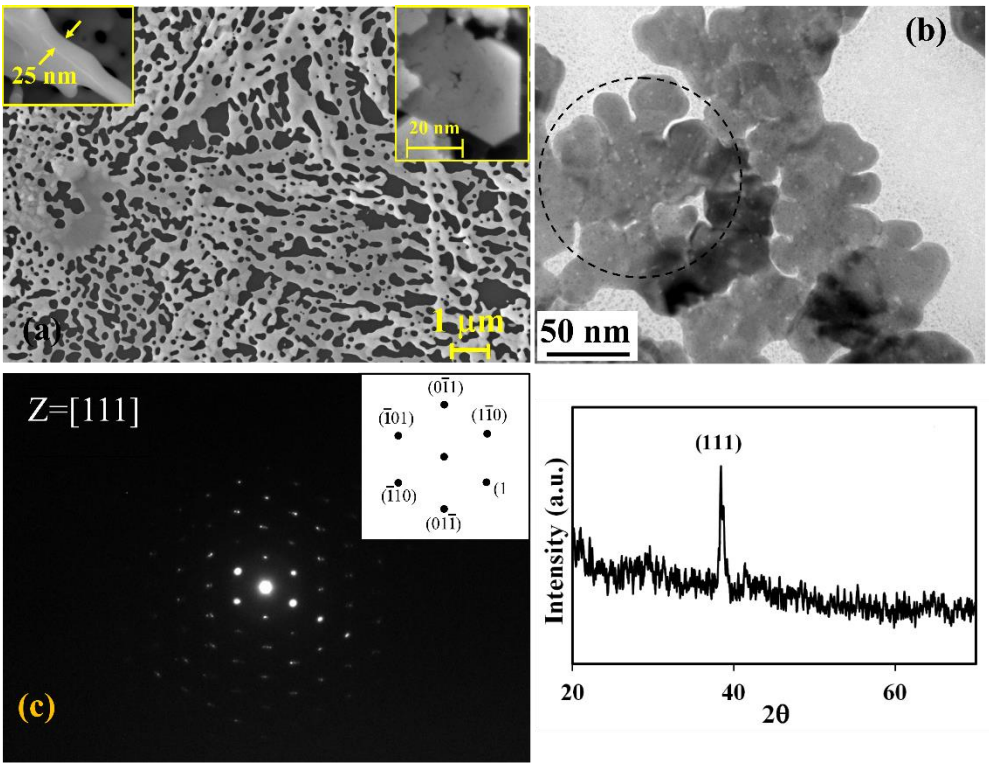

Figure 7-2: a) SEM image of the synthesized silver nanosheet. Inset at left demonstrates the thickness of the nanosheet and right inset image demonstrate a hexagonal structural block of the nanosheet.; b) TEM image of a nanosheet; c) Selected area diffraction pattern of the marked area of 2-b; d) X-ray diffraction pattern of the synthesized silver nanosheets.

7.5.2 Stability of the silver nanosheets

The atmospheric corrosion resistance of the synthesized silver nanosheets was investigated using an annealing heat treatment with thermogravimetric analysis (TGA) at 120°C under flow of air

(Figure 7-3-a). For this experiment, first the sample was heated at 300°C for one hour to remove the adsorbed PMAA molecules from the surface of the silver nanosheets. This happened successfully, which was evident by around 2% weight loss within the first 30 minutes of the TGA test. The Inset curve of Figure 7-3-a demonstrate the TGA test results of the PMAA, which shows the PMAA decomposed in temperature range of 350°C to 450°C. It is well stablished that the PMMA molecules tends to have all-trans conformation for maximum number of the bonds between carboxylate groups and silver nanoparticles [210]. Because of this special all-trans conformation, the PMAA molecule will be under stress, which caused a reduction of the decomposing temperature of chelated PMAA in comparison to free PMAA molecules. Therefore, it can conclude that the observed weight loss in the TGA test of the silver nanosheets was happened because of the decomposition of the PMAA. After one hour annealing at 300°C, the temperature was set at 120°C and kept constant for 900 minutes. During this period, around 0.1% weight increase was observed, which was followed by the same amount of decrease in weight. Therefore, it can be concluded that no traceable oxidation occurred in the sample. Hence, silver nanosheets are not subject to oxidation when exposed to airflow at this temperature.

Electrical stability testing was performed on a silver nanosheet with current density equal to 1×10^7 A/cm^2, while its temperature was controlled at 120˚C. The current characteristic curve versus timing is demonstrated in Figure 7-3-b. It is well known that electromigration causes a decreasing current regime versus time because of induced microstructural defects. However, in this case the current was stable over time, which suggests high electromigration resistance in the silver nanosheet. This result is compatible with the literature, where it has been reported that a thin film of silver with a high degree of (111)-orientation texture exhibits more electromigration resistance than one with a lower degree of (111)-orientation texture [15]. Moreover, it has been reported that pentagonal silver nanowires with (100) surface crystal are susceptible to electromigration at room temperature when a current density of 3.5×10^7 A/cm^2 is passed through a nanowire, and electromigration damage happens within a few hours [17]. Therefore, the (111) surface texture and defect-free boundary between the hexagonal and triangular structural blocks might result in high electromigration resistance, as observed in Figure 7-3 -b.

The structure and morphology of the silver nanosheets were observed after 30 days annealing at 120˚C, to scrutinize their response to temperature at the working temperature of the flow sensor, as thermal stability is one of the requirements for a durable and repeatable hot anemometer flow sensor. Figure 7-3-c shows an SEM image of a silver nanosheet after annealing, confirming that the shape and morphology of the nanosheet kept its morphology intact during 30 days heat treatment. XRD analysis

of heat treated silver nanosheets confirmed not only that the morphology, but also the crystal structure of the silver nanosheets was stable after heat treatment (Figure 7-3-d). This stability can be highlighted by comparison with that of silver pentagonal nanowires [18]. The silver nanowires degraded by annealing at 100˚C for 17 days while silver nanosheets are stable at this temperature [18]. The effect of the surface crystal texture of silver nanoparticles on their thermal stability was investigated, and it was clarified that the existence of low energy (111) crystal planes on the surface of nanocrystals leads to higher thermal stability [153]. In the case of silver nanosheets, the surface of the nanoparticles is almost all (111) plane and this special crystal structure results in superior thermal stability.

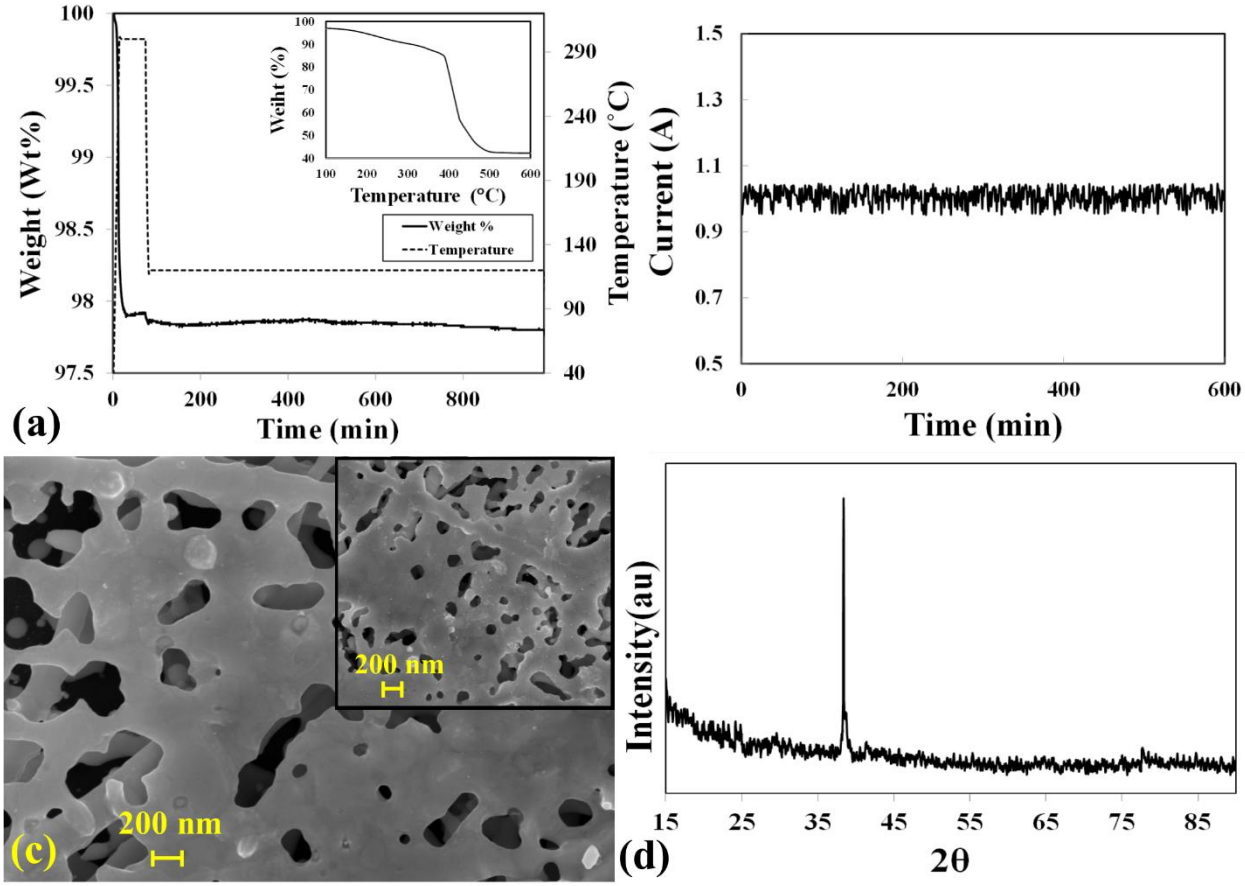

Figure 7-3: a) TGA analysis of the silver nanosheet. Inset is the TGA curve of the PMAA; c) Electrical current was passed through a silver nanosheet for 600 hours confirming the electrical stability of the sensing material; c) SEM image of a silver nanosheet after 30 days annealing at 150˚C. Inset demonstrate the nanosheet before annealing; d) XRD pattern of the silver after 30 days annealing at 150˚C.

7.5.3 Sensor Fabrication

A prototype sensor was fabricated by using an alumina sensor substrate to scoop out a floating silver nanosheet (Figure 7-4-a). Figure 3-b illustrates the sensor fabricated on the alumina substrate and the interdigitated electrodes of the sensor are shown in the inset. The existence of the PMAA layer on the surface of silver nanosheets prevents direct contact between the nanosheets and reduces electrical connection between the electrodes and silver nanosheets. In addition, a PMAA layer may cause a small gap between different silver islands and prevent complete nanojoining. TGA analysis of Figure 7-3-a revealed that the surface of the nanosheets can be cleaned by annealing at 300˚C. Therefore, the fabricated sensor was annealed at 300˚C for one hour to remove the PMAA. After cleaning, adjacent silver nanosheets are able to do more spontaneous nanojoining and increase conductivity of the layer. In addition, this heat treatment is able to increase the electrical contact between the electrodes and silver nanosheet by removing the PMAA surface layer.

Figure 7-4-b shows that the deposited silver nanosheet is not flat. To clarify the morphology of the sensing layer, deposition was done on the flat surface of a silicon wafer by scooping. The silicon wafer was selected for this observation to avoid complexity because of the roughness of the substrate. SEM observation demonstrated that the deposited layer was creased during scooping (Figure 7-5-a). Optical profilometry (3D universal profilometer - Rtec Instrument) was employed to examine the roughness of the deposited layer. Figure 7-5-b demonstrates an image prepare by the optical profilometry. The colors represent the thickness of the nanosheet and the color bar demonstrate the relation between the color and thickness. Based on this measurement, the average roughness of the layer is 0.097 μm. The deposited layer creased because the solution trapped below the nanosheet layer during scooping (inset in Figure 7-4-a) evaporated, leading to shrinkage and crimping of the nanosheet.

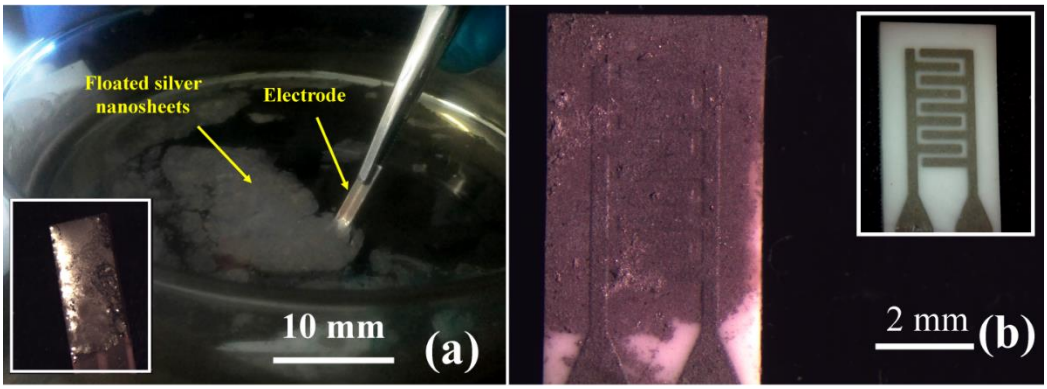

Figure 7-4: a) Sensor fabrication by scooping. Inset shows deposited silver nanosheet immediately after scooping; b) a silver nanosheet on the interdigitated electrodes. Inset is the interdigitated electrodes of the sensor substrate.

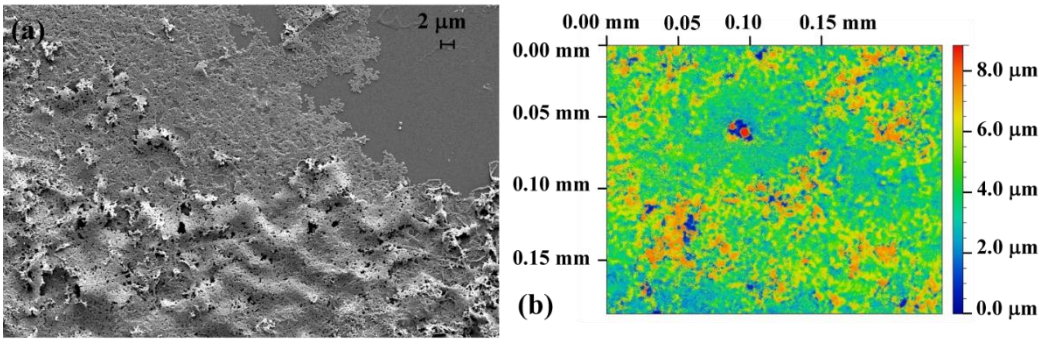

Figure 7-5: a) SEM images of the scooped silver nanosheet on a silicon wafer; b) Roughness of the scooped silver nanosheet.

7.5.4 Electrical properties of the fabricated sensor

Figure 7-6-a demonstrates the I-V curve of the fabricated sensor. The linear relation between the applied voltage and the electric current passing through the silver nanosheets confirmed the metallic nature of the silver nanosheet. The electrical resistance of the sensing material at different temperatures was measured under a static atmosphere (Figure 7-6-b). This experiment revealed that the response of the sensor to temperature change is linear at a rate of 0.0157 Ω/˚C between 50˚C to 210˚C. This linear relation between the temperature change and resistance of the sensor is important in reducing complexity of the sensor response to airflow.

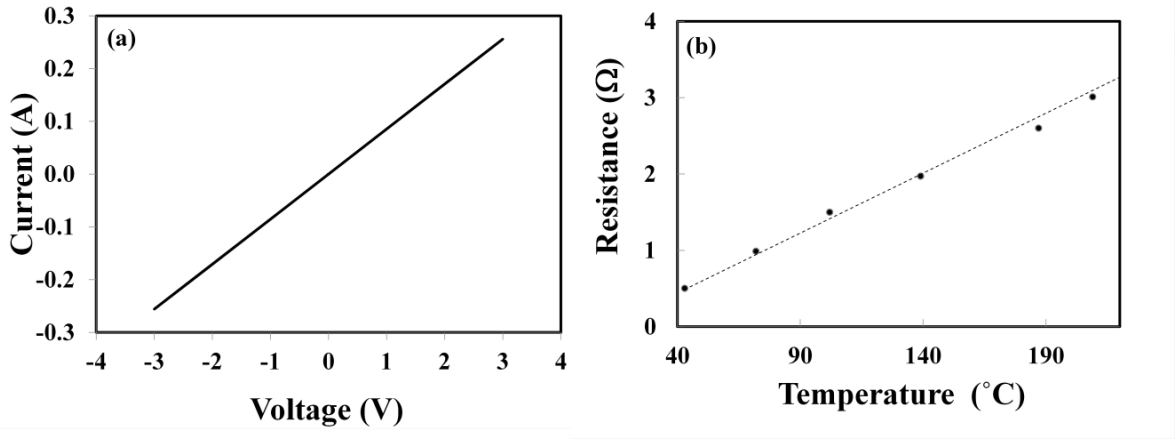

Figure 7-6: a) I-V curve of a silver nanosheet; b) The change of electrical resistance of a silver nanosheet versus temperature.

7.5.5 Sensor characterization

To investigate the response of the sensor to airflow, the sensor's temperature was kept at 120˚C by using the micro heater. Doing so enhanced the response of the sensor to air flow by decreasing the initial conductivity of the sensing material. The resistance of the sensor in its flow chamber was measured at various flow rates in the range of 0.1 to 10 ml/min (Figure 7-7-a). This measurement clarified a linear relation between airflow and resistance of the sheet, in the range of 0.1 to 5 ml/min. Therefore, a working range of 0.1 to 5 ml/min can be considered for this sensor and chamber geometry. A dynamic test was performed to find the response time of the sensor, which was around 2 second to 1 ml/min change in the flow (Figure 7-7-b). Finally, repeatability of the response of the sensor was examined by a dynamic test for 560 min with an on-off cycle of 20 min. (Figure 7-7-c), which revealed that the sensor is stable over a long dynamic experiment.

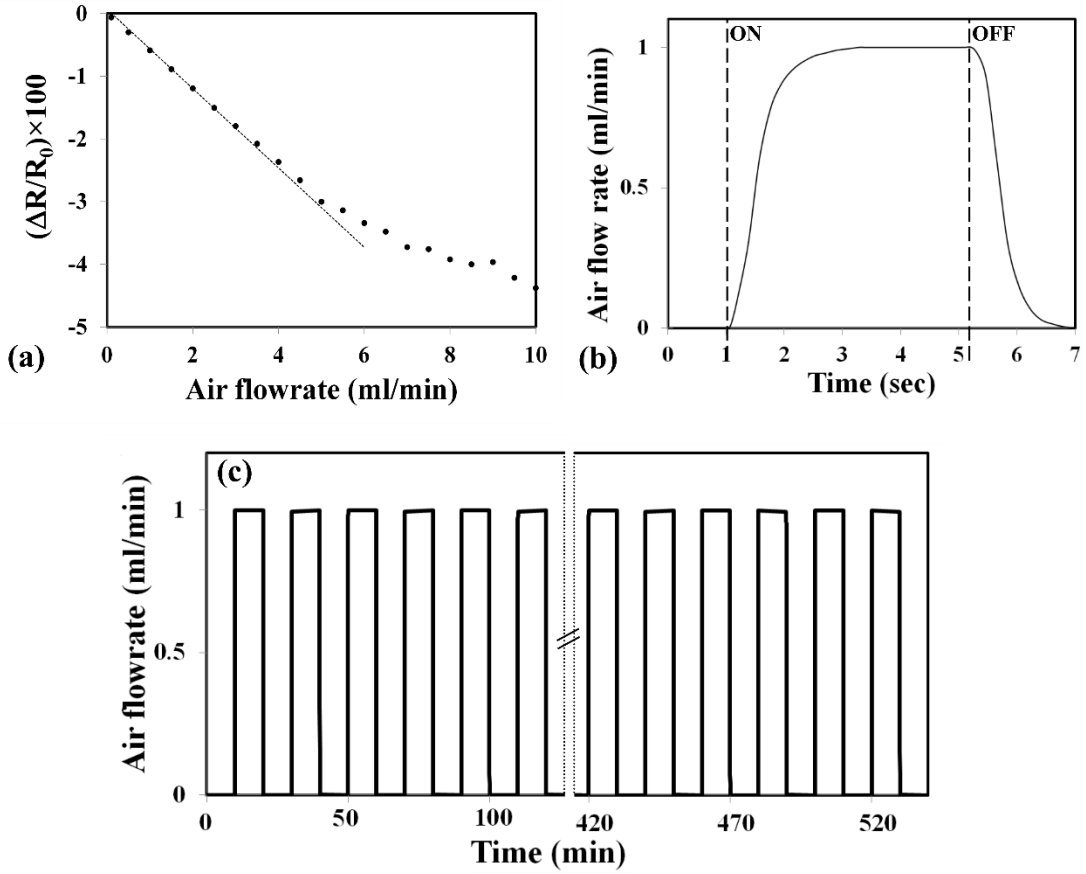

Figure 7-7: a) The resistance change of the sensor versus rate of the airflow; b) Airflow versus time, the on and off time of the air solenoid valve were marked on the graph; c) Dynamic test of the sensor: the duration of each on\off cycle was 20 min.

7.6 Conclusion

A high aspect ratio porous silver nanosheet was formed by simultaneous self-assembly and nanojoining of synthesized hexagonal and triangular silver nanoplates. The nanoplates resulted from the reduction of silver ions by ascorbic acid in the presence of PMAA molecules. The 25 nm thick nanosheets will float on top of reacting solutions after a few minutes. Atmospheric corrosion resistance, electrical or electromigration resistance, morphology and crystal stability of the synthesized silver nanosheet was investigated. Observations revealed that the silver nanosheet has excellent stability at 120˚C from an oxidation, thermal and electrical point of view, which is essential for a durable flow sensor.

An alumina substrate with interdigitated electrodes was selected as a sensor baseplate. The sensor was fabricated by scooping out a piece of the floating silver nanosheets onto the electrodes. The nanosheet was fixed on the senor substrate by with a one hour heat treatment at 300˚C. This sensor was used to measure the flow rate of air. Based on our experiments, the sensor showed a linear response to air flow in the range of 0.1 to 5 ml/min. The response time of the sensor was around 2 seconds when a 1 cc/min change happened in air flow. The dynamic test demonstrated that the response of the senor was stable after 9 hours of continued dynamic on-off experiments. Therefore, it was concluded that the synthesized silver nanosheet is an excellent candidate for a hot wire flow sensor, having high stability, proper gain, a remarkable response time and repeatability.

Chapter 8
Conclusions and future work

8.1 Conclusion

The main goal of this project was to develop a simple, high-yield, environmentally friendly method for synthesizing high aspect ratio silver nanoparticles. The classical synthesis methods for one-dimensional silver nanoparticles such as pentagonal silver nanowires are usually low-yield and costly, which have restricted application of the silver nanoparticles to special high-value applications such as nano- and bio-sensors. Regarding these weaknesses, in this research, a different approach was proposed for synthesis of the particles. The idea was to join silver nanoparticles to construct nanostructures. Looking at the literature illustrates that only few studies have been done in this field. Therefore, theoretical study was necessary along with experiments from which observations were made to provide basic knowledge from the process. In this regard, molecular dynamic simulation was employed to support the experimental observations.

The proposed particle formation method consists of synthesis of the structural blocks, then self-assembly and joining of them in a controllable way to achieve a repeatable product. The final nanostructure inherits the properties of the structural blocks. Hence, the structural blocks should be selected, carefully. For this study, among all silver nanoparticles, the triangular and hexagonal silver nanoplates were selected as structural blocks. By this selection, the final high aspect ratio structures should have a maximum fraction of (111) planes on the surface, which provides maximum stability for the synthesized nanostructures. Furthermore, one-dimensional silver nanowires with (100) surface texture had been synthesized before this research. However, nobody has previously reported large scale synthesis of high aspect ratio nanoparticles with high packing (111) crystal surface planes. Therefore, from this point of view, the new synthesis proposed here seems to be important and beneficial.

Based on the experimental observations and molecular dynamics simulations, conclusions can be drawn as follows:

1) The hexagonal and triangular nanoplates can join if they form in contact. This type of joining has been called oriented attachment in the literature. The mechanism of joining was studied by molecular dynamics simulation. MD simulation has shown that low temperature joining occurred by short movement of atoms to reach lower energy levels. These atoms have forced

their adjacent atoms to follow them and impose elastic strains on the crystal structure, which are released through subsequent rotation and elastic deformation of the particles. If crystal defects such as dislocations are created in the interface during joining, they will move out thus causing plastic deformation in the particles and after these events, the two nanoplates will be perfectly aligned and the system reaches minimum energy level. This decrease in the energy of the surface atoms is the driving force for nanoparticle joining. This mechanism works at all temperatures from 1K to melting of the nanoparticles, however the degree of alignment is temperature dependent. Based on the simulation results, two nanoplates are able to make a joint just through attachment without deformation. However, high temperature can provide enough energy to allow nanoparticles to expand the joining area through elastic and plastic deformation. Based on this observation, this process is more than a simple oriented attachment.

2) The original shape of the structural blocks will remain intact during joining, especially at room temperature.
3) The results of molecular dynamics simulation were confirmed by high-resolution TEM microscopy of the joined nanoplates, which demonstrated that joining of the nanoplates makes perfect crystals at the boundary.
4) Silver nanostructures have been synthesized by reduction of silver nitrate by ascorbic acid in presence of PMAA. In this reaction, ascorbic acid was mainly used to reduce silver ions. The PMAA is the major capping agent which controls the thickness of the product to around 25 nm by capping (111) planes. By using these chemicals and choosing suitable solution parameters, one-dimensional silver nanobelts, two-dimensional silver nanoflakes and multilayer and single-layer porous silver nanosheets were synthesized. Crystal structure of the synthesized nanoparticles was studied which confirmed that the nanobelts, nanoflakes and nanosheets have (111) surface crystal texture. This is not surprising since they are made by joining of hexagonal and triangular nanoplates. This special crystal structure of the products was confirmed by TEM and XRD observations.
5) The proposed synthesis method is a repeatable and fast synthesis. It is demonstrated that primary nanoplate structural blocks will assemble into secondary 1-dimensional belt-shaped segments, followed by secondary assembly and joining into various larger scale structures. The selectivity of preferred joint locations during this secondary assembly directed the development of the final morphology. We demonstrated that these are not kinetically controlled processes, and that the selectivity of joining location during secondary assembly correlated with pH and

the concentration of nitrate ions in solution. There were some indications that the concentration of silver ions correlated with the developed length of the secondary belt segments, however this was correlated with the factors that also selected for more linear secondary assembly modes, complicating analysis.

6) This work has demonstrated the importance of morphology and surface atomic arrangement as independent influences on the thermal stability of metallic nanoparticles. This is a fundamental issue, which should be addressed first when studying a nanoparticle at high temperature.
7) Thermal stability of silver nanowire and silver nanobelts were compared by both MD simulation and experimental observation. For pentagonal silver nanowire, the MD simulations and experimental observations indicate inherent thermal instability due to most surfaces being of (100) crystallography. This instability results in the erosion and diffusion of atoms across the surface, followed by their recrystallization as new clusters. The greatest erosion of these surfaces appears to occur at the edges between two adjoining (100) surfaces. This is likely in part due to the geometry of the cross section placing the atoms in proximity to two high-energy surfaces. Through this process, the nanowires appear to favor the formation of new surfaces with (111) crystallography, and the obstruction of (100) planes by the recrystallizing clusters. All of this has been observed without detectable contaminants, demonstrating that this degradation is independent of chemical attack. In contrast to silver nanowires, the MD simulations and experimental observations indicate that silver nanobelts are stable up to 500˚C, which makes them suitable for high-temperature functional materials. These results showed that the broad and flat (111) surfaces of the nanobelts were highly resistant to the effects of high temperature, which supports the prior statement that low energy crystal planes with high packing density provide better thermal stability.
8) The effects of temperature on the crystal structure of silver nanoparticles were investigated by molecular dynamics simulation. This research demonstrates that the melting of the nanoparticle occurred at a specific temperature and that surface melting does not happen before the melting temperature, which is compatible with thermodynamic rules. At relatively high temperature, the mechanical waves generated by the thermal phonons are strong enough to overcome the cohesive energy of the surface atoms and create surface defects such as adatoms, vacancies, and surface clusters. The density of these defects increases as the temperature increases and the accumulation of defects leads to an amorphous layer covering the surface of the nanoparticle in a range of temperature below the melting point. By investigating the internal pressure of the

nanoparticle, we demonstrate that the surface amorphous layer is a non-crystalline solid, which remains solid up to the melting temperature. The existence of this layer was confirmed prior to this research by experimental observations, and our new definition is compatible with previous observations.

9) The simulations revealed that the melting process around the melting point required a long incubation time before the nucleation of liquid and that melting occurred very slowly. Therefore, the simulation time must be selected with caution as insufficient simulation time-steps may generate erroneous results and lead to inaccurate conclusions such as surface premelting or melting of nanoparticles over a temperature range.
10) As one application, the silver nanobelts were introduced to silver nanoflakes-epoxy resin composite. This experiment has revealed that addition of 1 wt% of silver nanobelts to conventional ECA is able to enhance conductivity of the composite by 1300%.
11) Electrical stability and chemical stability of silver nanosheets were investigated at 150˚C. This observation has demonstrated that the synthesized nanosheets are stable under the experimental conditions used.
12) High aspect ratio porous silver nanosheet was employed for fabrication of an airflow sensor. The sensor was fabricated by scooping out a piece of the floating silver nanosheets onto the interdigitated electrodes, which were printed on an alumina substrate. The nanosheet was fixed on the sensor substrate by one-hour heat treatment at 300˚C. This sensor was used to measure the flow rate of air. Based on our experiments, the sensor showed a linear response to air flow in the range of 0.1 to 5 ml/min. The response time of the sensor was around 2 seconds when a 1 ml/min change happened in air flow. The dynamic test demonstrated that the response of the senor was stable after 9 hours of continued dynamic on-off experiments. Therefore, it was concluded that the synthesized silver nanosheet is an excellent candidate for a hot wire flow sensor, having high stability, proper gain, a remarkable response time and repeatability.

8.2 Recommendations for future work.

This research has introduced a new recipe for synthesizing high aspect ratio silver nanoparticles. Regarding all interesting aspects of the synthesis process and products, this would be an important and fruitful area for further work. The following topics can be suggested as some important research areas for future work:

1) Temperature of the reactor seems to be an important influence on the synthesis of nanoparticles by this method. In this research, all experiments were done at a temperature between 18˚C to 22˚C of the reactants in the synthesis. More research is required to determine the effect of temperature of the system on the morphology of the products.

2) Further experimental investigations are needed to clarify the role of ascorbic acid as structure modifier. This very important research topic will help in understanding the synthesis process.

3) Further investigation and experimentation into the nucleation of silver crystals in the reactor is strongly recommended. In this research it is observed that aging of silver nitrate solution, ultrasonication of the silver nitrate solution, and increasing the concentration of the silver nitrate solution have vital roles in the size and shape of the structural blocks. Therefore, understanding the nucleation mechanism might be very helpful in controlling the process.

4) In this research, a multistage joining process was proposed for the synthesis. However, it is not clear exactly by which mechanism the joining process may be shut down. If this mechanism can be understood, it will be possible to control the joining mechanism to have more progress, build complex nanostructures, and extend the process to three-dimensions.

5) There are not any grain boundaries in the structure of the assembled supercrystals. This was demonstrated by molecular dynamic simulation and by experiments. A reason for this phenomenon is instability of line defects in the nano-size crystals. This instability seems to be size dependent. However, there has not been any systematic investigation into this topic. Therefore, it can be a very important research topic for further investigation.

6) Another possible area of future research would be to investigate the mechanical properties of the synthesized particles. This might be an interesting topic because of the absence of stable dislocations in the crystal structure of the nanobelts. On the other hand, it is very easy to fabricate these nanoparticles in gram-scale. Therefore, this material can be a good candidate as nanofiller for composites. Hence, characterization of the mechanical behaviour of the nanobelts might be beneficial for future applications.

7) Further investigation into crystal structure and surface texture of the synthesized silver nanobelts and silver nanosheets could be interesting research topic. More detailed TEM analysis and employing the mathematical model to investigate the surface texture of the synthesized materials, as well as complementary experimental methods such as EBSD could

clarify the uniformity of the synthesized material and the effect of synthesis condition of the crystal texture of the product.

8) The synthesized silver nanoparticles are unique because of their special surface crystal texture. Therefore, investigation into the impact of this surface crystal texture on different applications such as catalytic and antibacterial performance of silver nanoparticles might be investigated.

Bibliography

1. Feynman, R.P., *There's Plenty of Room at the Bottom.* Caltech Eng. and Sci., 1960. **39**(5): p. 22-36.
2. Mansoori, G.A., *Principles of Nanoyechnology*. 2005: World Scientific.
3. Grzelczak, M., et al., *Directed self-assembly of nanoparticles.* ACSNANO, 2010 **4**(7): p. 3591–3605.
4. Galland, R., et al., *Fabrication of three-dimensional electrical connections by means of directed actin self-organization.* Nature Mater., 2013: p. 416-421.
5. Jana, N.R., *Shape effect in nanoparticle self-assembly.* Angew. Chem. Int. Ed., 2004. **43**: p. 1536 –1540.
6. Panigrahi, S., et al., *Self-Assembly of Silver Nanoparticles: Synthesis, Stabilization, Optical Properties, and Application in Surface-Enhanced Raman Scattering.* J. Phys. Chem. B, 2006. **110**: p. 13436-13444.
7. Murphy, C.J., et al., *Anisotropic metal nanoparticles: synthesis, assembly, and optical applications.* J. Phys. Chem. B, 2005. **109**: p. 13857-13870.
8. Riahifar, R., et al., *Sorting ZnO particles of different shapes with low frequency AC electric fields.* Materials Letters, 2011. **65**(4): p. 632-635.
9. Riahifar, R., et al., *Simulation of TiO2 particle trajectory in AC electric field.* Computational Materials Science, 2015. **108**: p. 183-191.
10. Chimentão, R.J., et al., *Different morphologies of silver nanoparticles as catalysts for the selective oxidation of styrene in the gas phase.* Chem. Commun., 2004: p. 846-847.
11. Rashid, M.H. and T.K. Mandal, *Synthesis and Catalytic Application of Nanostructured Silver Dendrites.* J. Phys. Chem. C, 2007. **111**(16750-16760).
12. Wen, X., et al., *Dendritic Nanostructures of Silver: Facile Synthesis, Structural Characterizations, and Sensing Applications.* Langmuir, 2006. **22**: p. 4836-4842.
13. Murray, B.J., E.C. Walter, and R.M. Penner, *Amine Vapor Sensing with Silver Mesowires.* Nano letters, 2004. **2**(2): p. 665-670.
14. Fang, Y., et al., *Branched silver nanowires as controllable plasmon routers.* Nano Lett, 2010. **10**(5): p. 1950-4.
15. Bittner, A., H. Seidel, and U. Schmid, *Electromigration resistance and long term stability of textured silver thin films on LTCC.* Microelectronic Engineering, 2011. **88**: p. 127-130.

16. Song, T.-B., et al., *Nanoscale Joule Heating and Electromigration Enhanced Ripening of Silver Nanowire Contacts.* ACSnano, 2014. **8**(3): p. 2804-2811.
17. Stahlmecke, B., et al., *Electromigration in self-organized single-crystalline silver nanowires.* Applied Physics Letters, 2006. **88**: p. 053122.
18. Khaligh, H.H. and I.A. Goldthorpe, *Failure of silver nanowire transparent electrodes under current flow.* Nanoscale Res. Lett., 2013. **8**: p. 235-241.
19. Elechiguerra, J.L., J. Reyes-Gasga, and M.J. Yacaman, *The role of twinning in shape evolution of anisotropic noble metal nanostructures.* J. Mater. Chem., 2006. **16**: p. 3906–3919.
20. Tsuji, M., et al., *Shape evolution of octahedral andtTriangular platelike silver nanocrystals from cubic and right bipyramidal seeds in DMF*. Cryst. Growth Des., 2009. **9**(11): p. 4700-4705.
21. Aherne, D., et al., *Optical properties and growth aspects of silver nanoprisms produced by a highly reproducible and rapid synthesis at room temperature.* Adv. Funct. Mater., 2008. **18**: p. 2005-2016.
22. Qi, W., B. Huang, and M. Wang, *Bond-Length and -Energy Variation of Small Gold Nanoparticles.* Journal of Computational and Theoretical Nanoscience, 2009. **6**: p. 635–639.
23. Qi, W.H., *Modeling the relaxed cohesive energy of metallic nanoclusters.* Materials Letters, 2006. **60**: p. 1678-1681.
24. QI, W.H. and M.P. WANG, *Size effect on the cohesive energy of nanoparticle.* Journal of Materials Science Letters, 2002. **21**: p. 1743-1745.
25. Chamaani, A., et al., *Thermodynamics and molecular dynamics investigation of a possible new critical size for surface and inner cohesive energy of Al nanoparticles.* Journal of Nanoparticle Research, 2011. **13**(11): p. 6059-6067.
26. Alarifi, H., et al., *Silver nanoparticles paste for low-temperature bonding of copper.* J. Elec. Mater., 2011. **40**(6): p. 1394-1402.
27. Alarifi, H.A., et al., *Determination of Complete Melting and Surface Premelting Points of Silver Nanoparticles by Molecular Dynamics Simulation.* J. phys. chem. C, 2013. **117**: p. 12289-12298.
28. Alarifi, H.A., et al., *Molecular Dynamics Simulation of Sintering and Surface Premelting of Silver Nanoparticles.* Mater. Trans. , 2013. **54**: p. 884-889.
29. Gosele, U., et al., *SELF-PROPAGATING ROOM-TEMPERATURE SILICON-WAFER BONDING IN ULTRAHIGH-VACUUM.* Applied physics letters, 1995. **67**(24): p. 3614-3616.

30. Zhang, F., et al., *Application of silver nanoparticles to cotton fabric as an antibacterial textile finish.* Fibers and Polymers, 2009. **10**(4): p. 496-501.
31. Speshock, J.L., et al., *Interaction of silver nanoparticles with Tacaribe virus.* J. Nanobiotechnol., 2010. **8:19**.
32. Shim, I.-K., et al., *An organometallic route to highly monodispersed silver nanoparticles and their application to ink-jet printing.* Mater. Chem. and Phys., 2008. **110**: p. 316-321.
33. Murugadoss, A. and A. Chattopadhyay, *A 'green' chitosan–silver nanoparticle composite as a heterogeneous as well as micro-heterogeneous catalyst.* Nanotechnology, 2008. **19**: p. 015603 (1-9).
34. Kumar, A., et al., *Silver-nanoparticle-embedded antimicrobial paints based on vegetable oil.* Nat. Mater., 2008. **7**: p. 236-241.
35. Chen, X. and H.J. Schluesener, *Nanosilver: A nanoproduct in medical application.* Toxicol. Lett., 2007. **176**: p. 1-12.
36. Bigall, N.C., et al., *Fungal templates for noble-metal nanoparticles and their application in catalysis.* Angew. Chem. Int. Ed., 2008. **47**: p. 7876-7879.
37. Lu, X., et al., *Chemical synthesis of novel Plasmonic nanoparticles.* annu. Rev. Phys. Chem., 2009. **60**: p. 167-192.
38. Sun, Y. and Y. Xia, *Shape-controlled synthesis of gold and silver nanoparticles.* science, 2002. **298**: p. 2176-2179.
39. Sun, Y., B. Mayers, and Y. Xia, *Transformation of silver nanospheres into nanobelts and triangular nanoplates through a thermal process.* Nano Letters, 2003. **3**(5): p. 675-679.
40. Sun, Y., et al., *Polyol synthesis of uniform silver nanowires: A plausible growth mechanism and the supporting evidence.* Nano Lett., 2003. **3**(7): p. 955-960.
41. Tao, A.R., S. Habas, and P. Yang, *Shape control of colloidal metal nanocrystals.* small, 2008. **4**(3): p. 310-325.
42. Burda, C., et al., *Chemistry and properties of nanocrystals of different shapes.* Chem. Rev., 2005. **105**: p. 1025-1102.
43. Grzelczak, M., et al., *Shape control in gold nanoparticle synthesis.* Chem. Soc. Rev., 2008. **37**: p. 1783-1791.
44. Xiao, J. and L. Qi, *Surfactant-assisted, shape-controlled synthesis of gold nanocrystals.* Nanoscale, 2011. **3**: p. 1383–1396.

45. Wiley, B., et al., *Shape-controlled synthesis of metal nanostructures: The case of silver.* Chem. Eur. J., 2005. **11**: p. 454-463.
46. WILEY, B., Y. SUN, and Y. XIA, *Synthesis of Silver Nanostructures with Controlled Shapes and Properties.* Acc. Chem. Res., 2007. **40**: p. 1067-1076.
47. Li, M., H. Schnablegger, and S. Mann, *Coupled synthesis and self-assembly of nanoparticles to give structures with controlled organization.* Nature, 1999. **402**: p. 393-395.
48. Gao, Y., et al., *Synthesis, characterization and self-assembly of silver nanowires.* Chemical Physics Letters, 2003. **380**: p. 146-149.
49. Tang, Z., N.A. Kotov, and M. Giersig, *Spontaneous organization of single CdTe nanoparticles into luminescent nanowires.* science, 2002. **297**: p. 237-240.
50. Gates, B., et al., *Single-Crystalline Nanowires of Ag2Se Can Be Synthesized by Templating against Nanowires of Trigonal Se.* J Am. Chem. Soc., 2001. **123**: p. 11500-11501.
51. Korgel, B.A. and D. Fitzmaurice, *Self-Assembly of Silver Nanocrystals into Two-Dimensional Nanowire Arrays.* Advanced Materials, 1998. **10**(9): p. 661-665.
52. Kalsin, A.M., et al., *Electrostatic Self-Assembly of Binary Nanoparticle Crystals with a Diamond-Like Lattice.* science, 2006. **312**: p. 420-424.
53. Zhang, X.-Y., et al., *Self-Assembly of Large-Scale and Ultrathin Silver Nanoplate Films with Tunable Plasmon Resonance Properties.* ACSNANO, 2011. **5**(11): p. 9082-9092.
54. Zhou, Y. and A. Hu, *From Microjoining to Nanojoining* The Open Surface Science Journal, 2011. **3**: p. 32-41.
55. Zhou, Y., et al., *Recent progress in micro and nano-joining.* Journal of Physics: Conference Series, 2009. **165**: p. 012012 (1-6).
56. Hu, A., et al., *Femtosecond laser welded nanostructures and plasmonic devices.* J. Laser App., 2012. **24**: p. 042001 (1-7).
57. Chacko, S., K. Joshi, and D.G. Kanhere, *Why Do Gallium Clusters Have a Higher Melting Point than the Bulk?* Physical Review Letters, 2004. **13**(92): p. 135506 (1-4).
58. Lehtinen, K.E.J. and M.R. Zachariah, *Effect of coalescence energy release on the temporal shape evolution of nanoparticles.* Physical Review B: Condensed Matter, 2001. **63**: p. 205402(1-7).
59. Ding, F., A. Rosén, and K. Bolton, *Size dependence of the coalescence and melting of iron clusters: A molecular-dynamics study.* Physical Review B: Condensed Matter, 2004. **70**: p. 075416 (1-6).

60. Ding, F., K. Bolton, and A. Rosen, *Molecular dynamics study of the surface melting of iron clusters.* Eur. Phys. J. D, 2005. **34**: p. 275-277.
61. Arcidiacono, S., et al., *On the coalescence of gold nanoparticles.* International Journal of Multiphase Flow, 2004. **30**(979-994).
62. Hu, A., et al., *Low temperature sintering of Ag nanoparticles for flexible electronics packaging.* Applied Physics Letters 2010. **97**: p. 153117 (1-3)
63. Guo, J.Y., et al., *Sintering dynamics and thermal stability of novel configurations of Ag clusters.* Journal of Physics and Chemistry of Solids, 2012. **73**: p. 1350-1357.
64. Frankel, D. and B. Smit, *Understanding Molecular Simulation: From Algorithms to Applications*. 1996, San Diego: Academic Press.
65. Kang, S., *Sintering: Densification, Grain Growth, and Microstructure*. 2004: Elsevier Ltd.
66. Hirata, Y., A. Hara, and I.A. Aksay, *Thermodynamics of densification of powder compact.* Cer. Inter., 2009. **35**: p. 2667-2674.
67. Lange, F.F., *Densification of powder compacts: An unfinished story.* j. Europ. Cer. Soc., 2008. **28**: p. 1509-1516.
68. Slamovich, E.B. and F.F. Lange, *Densification of large pores: I, experiments* J. Am. Ceram. Soc., 1992. **75**: p. 2498-2508.
69. Slamovich, E.B. and F.F. Lange, *Densificatio of large pores: II, Driving potentials and kinetiks.* J. Am. Ceram. Soc., 1993. **76**: p. 1584-1590.
70. Walker, R.F., *Mechanism of Material Transport During Sintering.* J. Am. Ceram. Soc., 1955. **36**: p. 187-197.
71. Magdassi, S., et al., *Triggering the Sintering of Silver Nanoparticles at Room Temperature.* ACSNANO, 2010. **4**(4): p. 1943-1948.
72. Hu, A., et al., *Low temperature sintering of Ag nanoparticles for flexible electronics packaging.* Applied Physics Letters, 2010. **97**: p. 153117 (1-3).
73. Amoli, B.M., et al., *Electrical conductive adhesives enhanced with high aspect-ratio silver nanobelts.* J. Macromol. Mater. Eng., 2014. **229**: p. 739-747.
74. Ide, E., et al., *Metal–metal bonding process using Ag metallo-organic nanoparticles.* Acta Materialia, 2005. **53**: p. 2385–2393.
75. Iwama, S. and T. Safashi, *Sintering of ultrafine metal powders . I. Coalescence growth stage of Au and Ag.* Japanese journal of Applied physics 1980. **19**(6): p. 1039-1044.

76. Jose-Yacaman, M., et al., *Surface Diffusion and Coalescence of Mobile Metal Nanoparticles.* J. Phys. Chem. B, 2005. **109**: p. 9703-9711.
77. Niederberger, M. and H. Colfen, *Oriented attachment and mesocrystals: non-classical crystallization mechanisms based on nanoparticle assembly.* Physical chemistry chemical physics : PCCP, 2006. **8**(28): p. 3271-87.
78. Zhang, H., et al., *Nanocrystal growth via oriented attachment.* CrystEngComm, 2014. **16**(8): p. 1407.
79. Gehrke, N., et al., *Superstructures of Calcium Carbonate Crystals by Oriented Attachment.* Crystal Growth and design, 2005. **5**(4): p. 1317-1319.
80. Daw, M.S. and M.I. Baskes, *Semiempirical, Quantum Mechanical Calculation of Hydrogen Embrittlement in Metals.* Physical Review Letters, 1983. **50**(17): p. 1285-1288.
81. Daw, M.S. and M.I. Baskes, *Embedded-atom method: Derivation and application to impurities, surfaces, and other defects in metals.* Physical Review B: Condensed Matter, 1984. **29**(12): p. 6443-6453.
82. Foiles, S.M., M.I. Baskes, and M.S. Daw, *Embedded-atom-method functions for fcc metals Cu, Ag, Au, Ni, Pd, Pt, and their alloys* Physical Review B: Condensed Matter, 1986. **33**(12): p. 7983-7991.
83. Humphrey, W., A. Dalke, and K. Schulten, *VMD- Visual Molecular Dynamic.* J. Molec. Graphics, 1996. **14**(1): p. 33-38.
84. Hoover, W.G., *Canonical dynamics: Equilibrium phase-space distributions.* Physical Review A: Atomic, Molecular, and Optical Physics, 1985. **31**(3): p. 1695-1697.
85. Hail, J.M., *Molecular dynamics simulation: Elementary Methods* 1992: JOHN WILEY & SONS.
86. Israelachvili, J.N., *Intermolecular and Surface Forces*. 3rd ed. 2011, San Diego: Academic Press.
87. Kittel, C., *Introduction to Solid state physics*, ed. S. ed. 1996, New York: John & Sons Inc.
88. Fang, z.z. and H. Wang, *Densification and grain growth during sintering of nanosized particles.* International Materials Reviews, 2008. **53**(6): p. 326-352.
89. Seiz, F. and D. Turnbull, *Solid State Physics*. Vol. 16. 1964, New York: Academic Press.
90. Shvartsburg, A.A. and M.F. Jarrold, *Solid Clusters above the Bulk Melting Point.* Physical Review Letters, 2000. **12**(85): p. 2530-2532.

91. Qi, W.H. and S.T. Lee, *Core–shell structures of silicon nanoparticles and nanowires with free and hydrogenated surface.* Chemical Physics Letters, 2009. **483**: p. 247-249.
92. Song, H.W., S.R. Guo, and Z.Q. Hu, *A coherent polycrystal model for the inverse Hall-Petch relation in nanocrystaaline materials.* Nanostructured Materials, 1999. **11**(2): p. 203-210.
93. Liu, H.B., et al., *Molecular dynamics simulation on edge dislocation in the bulk and nanoparticles of iron.* Computation Materials Science, 2003. **27**: p. 333-341.
94. Schall, P., et al., *Visualizing dislocation nucleation by indenting colloidal crystals.* Nature, 2006. **440**: p. 319-323.
95. Jose-Yacaman, M., E. Perez-Tijerinab, and S. Mejia-Rosales, *Defect structure in nanoalloys.* Journal of Materials Chemistry, 2007. **17**: p. 1035-1038.
96. Carlton, C.E., L. Rabenberg, and P.J. Ferreira, *On the nucleation of partial dislocations in nanoparticles.* Philosophical Magazine Letters, 2008. **88**: p. 715-724.
97. Qi, W.H., et al., *Generalized bond-energy model for cohesive energy of small metallic particles.* Physics Letters A, 2007. **370**: p. 494-498.
98. Peng, P., et al., *Self-Oriented Nanojoining of Silver Nanowires via Surface Selective Activation.* Part. Part. Syst. Charact., 2013. **30**(5): p. 420-426.
99. Maillard, M., S. Giorgio, and M.-P. Pileni, *Silver nanodisks.* Adv. Mater., 2002. **14**(15): p. 1084-1086.
100. Yang, Y., et al., *Solvothermal Synthesis of Multiple Shapes of Silver Nanoparticles and Their SERS Properties.* J. Phys. Chem. C, 2007. **111**(26): p. 9095-9104.
101. Songping, W. and M. Shuyuan, *Preparation of ultrafine silver powder using ascorbic acid as reducing agent and its application in MLCI.* Mater. Chem. and Phys., 2005. **89**: p. 423-427.
102. Zhang, D., et al., *Formation of silver nanowires in aqueous solutions of a double-hydrophilic block copolymer.* Chem. Mater., 2001. **13**: p. 2753-2755.
103. Ishizu, K., et al., *Encapsulation of silver nanoparticles within double-cylinder-type copolymer brushes as templates.* Polym. Adv. Technol., 2005. **16**: p. 834-839.
104. You, S.A., O.S. Kwon, and J. Jang, *A facile synthesis of uniform Ag nanoparticle decorated CVD-grown graphene via surface engineering.* J. Mater. Chem., 2012. **22**(34): p. 17805-17812.
105. Wang, X.M., et al., *Comparing the growth of PVD silver nanoparticles on ultra thin fluorocarbon plasma polymer films and self-assembled fluoroalkyl silane monolayers.* Nanotechnology, 2007. **18**(26).

106. Lofton, C. and W. Sigmund, *Mechanisms controlling crystal habits of Gold and Silver colloids.* Adv. Funct. Mater., 2005. **15**: p. 1197-1208.

107. Iwama, S. and K. Hayakawa, *Sintering of Ultrafine Metal Powders. II. Neck growth stage of Au, Ag, Al, and Cu.* Japanese journal of Applied physics, 1981. **20**(2): p. 335-340.

108. Yang, X., W. Hu, and Z. Zhang, *Atomistic simulations for the non-equilibrium surface premelting and melting of Nb(1 1 0) plane.* Current App. Phy., 2012. **10**: p. 436-443.

109. Kolasinski, K.W., *Surface Sci.* 3rd ed. 2012: John Wiley & Sons, Ltd.

110. Lu, L., et al., *Oriented Attachment-Based Assembly of Dendritic Silver Nanostructures at Room Temperature.* J. Phys. Chem. B, 2006. **110**: p. 23234-23241.

111. Prince, K.C., U. Breuer, and H.P. Bonzel, *Anisotropy of the order-disorder phase transition on the Pb(110) surface.* Phys. Rev. Lett., 1988. **60**(12): p. 1146-1149.

112. Katchalsky, A. and P. Spitnik, *Potentiometric Titrations of Polymethacrylic Acid.* Journal of Polymer Science, 1947. **2**(3): p. 432–446.

113. Ball, E.G., *Studies on Oxidation-Reduction: XXIII Ascorbic Acid.* J Biol Chem, 1937. **118:**: p. 219-239.

114. Kudaibergenov, S.E., *Recent Advances in the Study of Synthetic Polyampholytes in Solutions in: Polymer Latexes - Epoxide Resins – Polyampholytes.* Advances in Polymer Science, 1999. **144**: p. 115-197

115. Kimura, M., M. Yamamoto, and S. Yamabe, *Kinetics and Mechanism of the Oxidation of L-Ascorbic Acid by Tris-(oxalato)cobaltate(111) and Tris(1 ,I 0-phenanthroline)iron(111) Complexes in Aqueous Solution.* J. Chem. Soc., Dalton Trans., 1982. **2**: p. 423-427.

116. Moya, H.D. and N. Coichev, *Kinetic Studies of the Oxidation of L-Ascorbic Acid by Tris(Oxalate)Cobaltate in the Presence of CDTA Metal Ion Complexes.* , J. Braz. Chem. Soc, 2006. **17**(2): p. 364-368.

117. Vert, M., et al., *Terminology for biorelated polymers and applications (IUPAC Recommendations 2012).* Pure Appl. Chem., 2012. **84**(2): p. 377-410.

118. Azarnia, N., H.M. Berman, and R.D. Rosenstein, *The crystal structure of D-iso-Ascorbic acid.* Acta Cryst., 1971. **B72**: p. 2157-2161.

119. Grinstead, R.R., *The Oxidation of Ascorbic Acid by Hydrogen Peroxide. Catalysis by Ethylenediaminetetraacetato-Iron (111).* J. Am. Chem. Sco. , 1960. **82**(13): p. 3464–3471.

120. Esumi, K., et al., *Role of Poly(amidoamine) Dendrimers for Preparing Nanoparticles of Gold, Platinum, and Silver.* Langmuir, 2000. **16**: p. 2604-2608.

121. Chen, S. and D.L. Carroll, *Synthesis and characterization of truncated triangular silver nanoplates.* Nano Letters, 2002. **2**(9): p. 1003-1007.
122. Marzbanrad, E., et al., *Room temperature nanojoining of triangular and hexagonal silver nanodisks.* J. Phys. Chem. C, 2013. **117**: p. 16665-16676.
123. Xiong, Y., et al., *Trimeric clusters of silver in aqueous AgNO3 solutions and their role as nuclei in forming triangular nanoplates of silver.* Angew. Chem. Int. Ed., 2007. **46**: p. 4917-4921.
124. Kim, M.H., D.K. Yoon, and S.H. Im, *Growth pathways of silver nanoplates in kinetically controlled synthesis: bimodal versus unimodal growth.* RSC Adv., 2015. **5**(19): p. 14266-14272.
125. Yacaman, M.J., et al., *Structure shape and stability of nanometric sized particles.* J. Vac. Sci. and Tech. B, 2001. **19**: p. 1091-1103.
126. Desireddy, A., et al., *Ultrastable silver nanoparticles.* Nature, 2013. **501**: p. 399-402.
127. Liang, L.H., et al., *Increase in thermal stability induced by organic coatings on nanoparticles.* Phys. Rev. B, 2004. **70**: p. 205419 (1-5).
128. Zhao, M. and Q. Jiang, *Size effect on thermal properties in low-dimensional materials.* key Engineering Materials, 2010. **444**: p. 189-217.
129. Liu, X., et al., *Synthesis of Thermally Stable and Highly Active Bimetallic Au-Ag Nanoparticles on Inert Supports.* Chem. Mater., 2009. **21**: p. 410-418.
130. Sun, J., et al., *Toward Monodispersed Silver Nanoparticles with Unusual Thermal Stability.* J. Am. Ceram. Soc., 2006. **128**: p. 15756-15764.
131. Shim, J.-H., B.-J. Lee, and Y.W. Cho, *Thermal stability of unsupported gold nanoparticle: a molecular dynamics study.* surface Science, 2002. **512**: p. 262-268.
132. Guisbiers, G., et al., *Effects of Shape on the Phase Stability of Nanoparticles.* J. Comput. Theor. Nanosc., 2007. **4**(2): p. 309-315.
133. Liu, C., et al., *Preparation of Silver Nanoparticle and Its Application to the Determination of ct-DNA.* Sensors 2007. **7**: p. 708-718.
134. Zhao, L., K.L. Kelly, and G.C. Schatz, *The Extinction Spectra of Silver Nanoparticle Arrays: Influence of Array Structure on Plasmon Resonance Wavelength and Width.* J. Phys. Chem. B, 2003. **107**: p. 7343-7350.
135. Elechiguerra, J.L., et al., *Interaction of silver nanoparticles with HIV-1.* J. Nanobiotechnol., 2005. **3:6**.

136. Pradhan, N., A. Pal, and T. Pal, *Silver nanoparticle catalyzed reduction of aromatic nitro compounds.* Colloid Surface A, 2002. **196**: p. 247-257.
137. Cai, H., et al., *An electrochemical DNA hybridization detection assay based on a silver nanoparticle label.* Analyst, 2002. **127**: p. 803-808.
138. Leach, A.M., M. McDowell, and K. Gall, *Deformation of Top-Down and Bottom-Up Silver Nanowires.* Avd. funct. Mater., 2007. **17**: p. 43-53.
139. Lee, J.Y., et al., *Solution-Processed Metal Nanowire Mesh Transparent Electrodes.* Nano Lett., 2008. **8**(2): p. 689-692.
140. Gunawidjaja, R., et al., *Flexible and Robust 2D Arrays of Silver Nanowires Encapsulated within Freestanding Layer-by-Layer Films.* Adv. Funct. Mater., 2006. **16**: p. 2024-2032.
141. Peng, P., et al., *Functionalization of silver nanowire surfaces with copper oxide for surface-enhanced Raman spectroscopic bio-sensing.* : J. Mater. Chem., 2012. **22**: p. 15495-15499.
142. Kim, T.Y., et al., *Uniformly Interconnected Silver-Nanowire Networks for Transparent Film Heaters.* adv. Funct. Mater., 2013. **23**: p. 1250-1255.
143. Feng, J., et al., *Ag/epoxy nanocomposite film with aligned Ag nanowires and their polarization property.* Jornal of Materials research, 2011. **26**(21): p. 2691-2700.
144. Zhang, X., et al., *Large-size graphene microsheets as a protective layer for transparent conductive silver nanowire film heaters.* Carbon, 2014. **69**: p. 437-443.
145. Farney, J.P., G.W. Kammlott, and T.E. Graedel, *The corrosion of silver by atmospheric sulfurous gases.* Corr. sci., 1985. **25**(2): p. 133-143.
146. Elechiguerra, J.L., et al., *Corrosion at the Nanoscale: The Case of Silver Nanowires and Nanoparticles.* Chem. Mater., 2005. **14**: p. 6042-6052.
147. Jin, R., et al., *Photoinduced Conversion of Silver Nanospheres to Nanoprisms.* Science, 2001. **294**: p. 1901-1903.
148. Pastoriza-Santos, I. and L.M. Liz-Marza´n, *Synthesis of Silver Nanoprisms in DMF.* Nano Lett., 2002. **2**(8): p. 903-905.
149. Sun, Y., et al., *Crystalline Silver Nanowires by Soft Solution Processing.* Nano Lett., 2002. **2**(2): p. 165-168.
150. Sun, Y. and Y. Xia, *Large-Scale Synthesis of Uniform Silver Nanowires Through a Soft, Self-Seeding, Polyol Process* Adv. Mater., 2002. **14**(11): p. 833-837.

151. Peng, P., et al., *Room-temperature pressureless bonding with silver nanowire paste: towards organic electronic and heat-sensitive functional devices packaging.* J. Mater. Chem., 2012. **22**: p. 12997-13001.
152. Landry, B.K., et al., *The kinetics of thermal instability in nanocrystalline silver and the effect of heat treatment on the antibacterial activity of nanocrystalline silver dressings.* Boimater., 2009. **30**(36): p. 6929-6939.
153. Marzbanrad, E., et al., *How morphology and surface crystal texture affect thermal stability of a metallic nanoparticle: the case of silver nanobelts and pentagonal silver nanowires.* Phys. Chem. Chem. Phys., 2015. **17**: p. 315-324.
154. Orellana, W. and G. Gutiérrez, *First-principles calculations of the thermal stability of Ti3SiC2(0001) surfaces.* Surface Science, 2011. **605**(23-24): p. 2087-2091.
155. Sun, C.Q., *Size dependence of nanostructures: Impact of bond order deficiency.* Prog. Solid State Chem., 2007. **35**: p. 1-159.
156. Stranski, I.N., *Uber das Verhalten nichtpolarer Kristalle dicht unterhalb des Schmelzpunktes und beim Schmelzpunkt selbst.* Z. Phys., 1942. **119**: p. 22-43.
157. Gaskell, D.R., *Introduction to Metallurgical Thermodynamics*. 2nd ed. 1981, New York: Hemisphere Publishing Corporation.
158. Begtrup, G.E., et al., *Probing Nanoscale Solids at Thermal Extremes.* Phys. Rev. Lett., 2007. **99**: p. 155901 (1-4).
159. Luo, W. and W. Hu, *Gibbs freeenergy,surfacestressandmeltingpointofnanoparticle.* Physica B, 2013. **425**: p. 90-94.
160. Levitas, V.I. and K. Samani, *Size and mechanics effects in surface-induced melting of nanoparticles.* Nature Com., 2011. **2**: p. 284 (1-6).
161. Levitas, V.I. and K. Samani, *Melting and solidification of nanoparticles: Scale effects, thermally activated surface nucleation, and bistable states.* Phys. Rev. B, 2014. **89**: p. 075427 (1-10).
162. Boettinger, W.J., et al., *Phase-field simulation of solidification 1.* Annu. Rev. Mater. Res., 2002. **32**: p. 163-194.
163. GON, A.W.D.v.d., et al., *Melting of Al surfaces.* Surface Sci., 1990. **227**: p. 143-149.
164. Frenken, J.W.M. and J.F.v.d. Veen, *Observation of Surface Melting.* Phys. Rev. Lett., 1985. **54**: p. 134-137.

165. Pavlovska, A., M. Tikhov, and Y.G.E. Bauer, *Thermal disordering of the Al(110) surface* Surface Sci., 1992. **278**: p. 303-316.
166. Blanckenhagen, P.v., W. Schommers, and V. Voegele, *Temperature dependence of the structure of the AI(110) surface.* J. Vac. Sci. Technol. A, 1986. **5**: p. 649.
167. Frenken, J.W.M., J.P. Toennies, and C. Woll, *Self-Diffusion at a Melting Surface Observed by He Scattering.* Phys. Rev. Lett., 1988. **60**: p. 1727-1730.
168. Dosch, H., et al., *Synchrotron x-ray scattering from the Al(110) surface at the onset of surface melting.* Europhys. lett. , 1991. **15**(5): p. 527-533.
169. Pinxteren, H.M.v., et al., *Thermal diffuse scattering from surface-melted Pb(110).* Phys. Rev. B, 1995. **51**(20): p. 14573-14575.
170. Rühm, A., et al., *Bulk and surface premelting phenomena inα-gallium.* Phy. Rev. B, 2003. **68**(22).
171. Pedemonte, L., et al., *Low-energy ion scattering study of Al(1 1 0) thermal disordering*. Nuclear Inst. Meth. in Phy. Res. B, 2002. **193**: p. 563-567.
172. Kristensen, J.K. and R.M.J. Cotterill, *On the existence of pre-melting and after-melting effects A neutron scattering investigation.* Phil. Mag. , 1977. **36**(2): p. 437-452.
173. Lereahy, Y., et al., *Time-resolved electron microscopy studies of the structure of nanoparticles and their melting.* Phil. Mag. B, 2001. **91**(11): p. 1801-1819.
174. Levitas, V.I., et al., *Crystal-crystal phase transformation via surface-induced virtual premelting.* Phys. Rev. B, 2012. **85**: p. 220104-(1-5).
175. Krumb, N., *Melting of small cluster of atoms.* Nature 1973. **243**: p. 100-102.
176. Landa, A., et al., *Molecular dynamics study of disordering, roughening, and premelting of the Pb(110) surface.* J. Non-Crys. Solids, 1996. **205-206**: p. 767-771.
177. Rahman, T.S., Z. Tian, and J.E. Black, *Surface disordering, roughening and premelting of Ag(110).* Surface Sci., 1997. **374**: p. 9-16.
178. Nikasi, Y.J. and C. Ebner, *Molecular dynamics study of surface premelting in adsorbed argon films on graphite.* J. Phys.: Condens. Matter, 1989. **1**: p. 2709-2713.
179. Xi-yuan, Y. and W. Dan, *Atomic simulations for surface-initiated melting of Nb(111).* Trans. Nonferrois Met. Soc. China, 2009. **19**: p. 210-214.
180. Shen, T., et al., *Size dependence and phase transition during melting of fcc-Fe nanoparticles: A molecular dynamics simulation.* App. Surface Sci., 2013. **277**: p. 7-14.
181. Tang, F.L., et al., *Premelting ofAlnonperfect(111)surface.* Physica B, 2010. **405**: p. 1248-1252.

182. Wee, T.H., et al., *Premelting disordering of the Si(113) surface studied by tight-binding molecular dynamics.* J. Phys.: Condens. Matter, 1996. **8**: p. 6511-6523.

183. Wen, Y.H., et al., *A molecular dynamics study of shape transformation and melting of tetrahexahedral platinum nanoparticle.* Chem. Phys. Lett., 2009. **471**: p. 295-299.

184. Song, H., et al., *A molecular dynamics simulation of (1 1 0) surface premelting in Ni.* Scripta Mat., 2010. **63**: p. 128-131.

185. Yong-Jun, L., *Enhanced Surface Premelting of Ni90Si10 Nanoparticles.* Chin. Phys. Lett., 2012. **29**(4): p. 046401 (1-4).

186. Alarifi, H.A., et al., J. Phys. Chem. C, 2013. **117**(Determination of complete melting and surface premelting points of silver nanoparticles by molecular dynamics simulation): p. 12289-12298.

187. Rosato, V., G. Ciccotti, and V. Pontikis, *Molecular-dynamics study of surface premelting effects.* Phys. Rev. B, 1986. **33**(3): p. 1860-1870.

188. Heyes, D.M., *Pressure tensor of partial-charge and point-dipole lattices with bulk and surface geometries.* Physical Review B, 1994. **49**(2): p. 755-764.

189. Thompson, A.P., S.J. Plimpton, and W. Mattson, *General formulation of pressure and stress tensor for arbitrary many-body interaction potentials under periodic boundary conditions.* The Journal of chemical physics, 2009. **131**(15): p. 154107.

190. Suryanarayana, C. and A. Inoue, *Bulk metallic glasses*. 2011, Boca Raton: Taylor & Francis Group.

191. Amoli, B.M., et al., *Electrical Conductive Adhesives Enhanced with High-Aspect-Ratio Silver Nanobelts.* Macromolecular Materials and Engineering, 2013: p. n/a-n/a.

192. Tang, H., et al., *A label-free electrochemical immunoassay for carcinoembryonic antigen (CEA) based on gold nanoparticles (AuNPs) and nonconductive polymer film.* Biosen. Bioelect., 2007. **22**(6): p. 1061-1067.

193. Maruyama, M., *Surface premelting phenomena of rare gas crystals.* J. Crystal Growth, 1989. **94**: p. 757-761.

194. Nenow, D., *Surface premelting.* Prog. Crystal Growth and Charact, 1984. **9**: p. 185-225.

195. Nenow, D. and A. Trayanov, *Surface premelting phenomena.* Surface Sci., 1989. **213**: p. 488-501.

196. Liptak, B.G., *Process Measurement and Analysis*. 2003, London: CRC Press.

197. Kuo, J.T.W., L. Yu, and E. Meng, *Micromachined Thermal Flow Sensors—A Review.* Micromachines, 2012. **3**: p. 550-573.
198. Adamec, R.J. and D.V. Thiel, *Self Heated Thermo-Resistive Element Hot Wire Anemometer.* IEEE Sensors J., 2010. **10**(4): p. 847-848.
199. Bensidhoum, M.T., et al., *Fabrication flaws and reliability in MEMS thin film polycrystalline flow sensor.* Microsyst Technol, 2014. **20**: p. 1-7.
200. Buder, U., et al., *AeroMEMS Wall Hot-Wire Anemometer on Polyimide Substrate Featuring Top Side or Bottom Side Bondpads.* IEEE Sensors J., 2007. **7**(8): p. 1095-1101.
201. Dong, X., et al., *Compact Anemometer Using Silver-Coated Fiber Bragg Grating.* IEEE Photonics J., 2012. **4**(5): p. 1381-1386.
202. Liu, H.-B., et al., *High Sensitivity, Miniature, Full 2-D Anemometer Based on MEMS Hot-Film Sensors.* IEEE Sensors J., 2013. **13**(5): p. 1914-1920.
203. Nagaiah, N.R., et al., *A Novel Design and Analysis of a MEMS Ceramic Hot-Wire Anemometer for High temperature Applications.* J. Phy. Conference Series, 2006. **34**: p. 277-282.
204. Piotto, M., G. Pennelli, and P. Bruschi, *Fabrication and characterization of a directional anemometer based on a single chip MEMS flow sensor.* Microelectronic Eng., 2011. **88**: p. 2214-2217.
205. Sazhin, O., *Novel mass air flow meter for automobile industry based on thermal flow microsensor. I. Analytical model and microsensor.* Flow Measur. Instrument., 2013. **30**: p. 60-65.
206. Sazhin, O., *Novel mass air flow meter for automobile industry based on thermal flow microsensor. II. Flow meter, test procedures and results.* Flow Measur. Instrument., 2014. **35**: p. 48-54.
207. Viard, R., et al., *A robust thermal microstructure for mass flow rate measurement in steady and unsteady flows.* J. Micromech. Microeng., 2013. **23**: p. 065016 (1-8).
208. Tanner, D.B. and D.C. Larson, *Electrical resistivity of silver films.* Phy. rev., 1968. **166**(3): p. 652-655.
209. Marzbanrad, E., et al., *Effect of Solution Conditions on the Fabrication of Silver Nanobelts,Nanoflakes and Porous Nanosheets with (111) Surface Crystal Orientation.* J. of Nanoscience and Nanotechnology. **Submitted**.
210. Li, Y. and C.P. Wong, *Monolayer protection for electrochemical migration control in silver nanocomposite.* App. Phys. lett., 2006. **89**: p. 112112 (1-3).